

DISSERTATION ZUR ERLANGUNG DES DOKTORGRADES DER  
FAKULTÄT FÜR CHEMIE UND PHARMAZIE DER  
LUDWIG-MAXIMILIANS-UNIVERSITÄT MÜNCHEN

NEW METHODS VISUALIZING  
MESOSTRUCTURED MATERIALS

ANDREAS ZÜRNER

AUS

MÜHLDORF AM INN

2011



### **Erklärung**

Diese Dissertation wurde im Sinne von § 13 Abs. 3 bzw. 4 der Promotionsordnung vom 29. Januar 1998 (in der Fassung der sechsten Änderungssatzung vom 16. August 2010) von Herrn Prof. Dr. Thomas Bein betreut.

### **Ehrenwörtliche Versicherung**

Diese Dissertation wurde selbständig, ohne unerlaubte Hilfe erarbeitet.

München, am 07. Juli 2011



---

Dissertation eingereicht am	07. Juli 2011
1. Gutachter	Prof. Dr. Thomas Bein
2. Gutachter	Prof. Dr. Christina Scheu
Mündliche Prüfung am	03. November 2011





## **Danksagung**

Diese Arbeit wäre ohne die Hilfe einer Vielzahl sehr netter Menschen nicht möglich gewesen. Keinen zu vergessen ist ein äußerst schwieriges Unterfangen, dem ich dennoch im Folgenden versuche gerecht zu werden.

Zunächst einmal gilt mein Dank Professor Thomas Bein, der mich freundlicherweise in seinen Arbeitskreis aufnahm und somit diese Arbeit überhaupt erst möglich machte. Die subgroup-meetings und sonstigen Diskussionen waren stets eine Bereicherung und nicht selten die entscheidenden Ideengeber. Sehr zu schätzen weiß ich auch die mir gewährte wissenschaftliche Freiheit, sowie die zahlreichen Konferenzen und Tagungen an denen ich teilnehmen durfte. Dafür nochmals meinen herzlichsten Dank.

Ebenso danken möchte ich Professor Christina Scheu für die Übernahme des Zweitgutachtens und das Fortführen des Tomographie-Themas in Ihrer Gruppe.

Mein Dank gilt auch Johanna Kirstein und Professor Christoph Bräuchle, sowie seinem gesamten Arbeitskreis für die über Jahre hinweg hervorragende Zusammenarbeit und die exzellenten Ergebnisse, die dadurch zustande kamen.

Ebenfalls dankbar für die gute Zusammenarbeit bin ich Ruoshan Wei und Ulrich Rant vom Walter Schottky Institut, München.

Besonders bedanken möchte ich mich bei meinen ehemaligen Kollegen im Arbeitskreis von Professor Bein. Ihr wart stets hilfsbereite und kompetente Gesprächspartner, sowie wichtige Ideengeber. Dennoch werden mir vor allem die nicht fachlichen Konversationen, die Mittagessen und Kuchenpausen, sowie die Feiern und Grillabende besonders in Erinnerung bleiben. Vielen Dank dafür.

Markus, danke für die unzähligen Stunden am TEM und die vielen Diskussionen, die Elektronenmikroskopie betreffend.

Valentina möchte ich danken für Ihre Hartnäckigkeit bei der Synthese der mesoporösen Partikel für die Tomographie, für die Gespräche im Büro und beim Mittagessen und dafür, dass Sie es mit mir solange im gleichen Büro ausgehalten hat.

Axel, danke für Deine Hilfe beim "clicken" der Enzyme in den mesoporösen Filmen.

Danke an Camilla, Jörg, Keili und Ralf für die beste Konferenz überhaupt (Paris) und natürlich für die Fahrten ans Elettra. Ich habe es sehr genossen.

Den Alt-Alt-Doktoranden Alex, Barbara, Enrica, Hendrik, Johannes, Stefan und Wastl möchte ich für das beste F-Praktikum meiner Studienzeit und für Ihre Unterstützung zu Beginn der Arbeit danken.

Die Studenten, die bei mir F-Praktikum gemacht haben, möchte ich natürlich nicht unerwähnt lassen. Danke an Dennis, Maria, Michael, Philipp, Uan-Siing und Veronika für ihre tolle Arbeit.

Ebenso gilt mein Dank all den ehemaligen Kollegen im AK Bein, die bis jetzt unerwähnt blieben: Alexandra, Basti, Benni, Dina, Gabriela, Huihong, Johann, Johann, Karin, Lea, Melanie, Mirjam, Momtchil, Monika, Norma, Olivier, Shaofeng, Sonni, Stefan, Svetlana, Yan, Yujing. Danke, dass Ihr alle dazu beigetragen habt, dass ich trotz manch langer "Durststrecken" sehr gerne an meine Doktorandenzeit zurückdenken werde.

Danke auch an die guten Seelen des Arbeitskreises, Regina und Tina. Ohne Euch hätte ich wahrscheinlich keinen einzigen Reiseantrag richtig ausgefüllt und wäre wohl jedesmal verzweifelt, wenn ich auf der Suche nach passenden Teilen für Versuchsaufbauten war.

Steffen, danke für die unzähligen SEM-Sitzungen und die langwierigen TEM-Aufnahmen für die Überlagerung mit den Fluoreszenzbildern.

Danke an die Mitarbeiter der Feinmechanik und der Elektronikwerkstatt für die exzellente Arbeit beim Bau des Dip-Coaters.

Bekanntlich kommt das Beste ja zum Schluß und auch ich will am Ende den wichtigsten Menschen in meinem Leben überhaupt danken: Meinen Eltern, meiner Schwester, Ernst und Jakob und natürlich Sylviane, Florian und Maximilian. Danke, dass Ihr da seid und so seid wie Ihr seid.

*für Christian und Maximilian*



## Summary

Today nanotechnology has a direct or at least an indirect influence on many industrial sectors. It is one of the key technologies of the 21st century and the development of new markets still continues. Two principal strategies for the creation of nanostructures and nanomaterials do exist. On the one hand devices are processed physically, chemically and mechanically until the desired structure, e.g. computer chips, are produced. On the other hand small building blocks, for example single molecules, are used to form bigger units by self-assembly — a technique nature has made use of since millions of years. In the future, a combination of both methods will certainly allow us to produce smaller and more complex structures in shorter periods of time. Mesoporous silica could hereby serve as a possible starting point. This material has pores with diameters ranging from about 2 to 50 nm. The pore walls are built up from silicon dioxide. It can be considered as a porous glass with a specific surface area several times larger than that of many silica gel materials. Mesoporous silica, in particular mesoporous thin layers, are introduced in the first three sections of this work, focusing on various structure types, synthesis and of course characterization.

The synthesis of nano sized systems and the understanding of their physical and chemical properties is much easier if the real structure is visualized. This is the reason why microscopy, in the case of nanotechnology primarily electron microscopy, has evolved into one of the most important characterization techniques. For example, transmission electron microscopy can image the structure of thin mesoporous layers, built-up by channels parallel to the surface. Optical microscopy, by contrast, is able to visualize the diffusion of fluorescent molecules incorporated into these pores, but it cannot resolve the mesoporous structure. However, section 4 demonstrates how to get both information from the same sample and what insights are gained by the combination of optical and electron microscopy. In cooperation with Johanna Kirstein from the group of Prof. Bräuchle, it is shown how a single luminescent molecule travels along the channels of a mesoporous structure or how it bounces back at domain boundaries and tries to find a new way. Furthermore, lateral motion between 'leaky' channels is observed, allowing the molecule to explore different parallel channels within an otherwise well-ordered periodic structure.

The diffusion of molecules within the pores of porous materials is crucial for potential applications. The diffusion depends on so-called host-guest in-

teractions, caused by the physical and chemical properties of the framework and incorporated species. Hence, a detailed analysis and controlled modification of these interactions is essential, e.g. for the synthesis of mesoporous silica-nanospheres dedicated to act as intelligent drug delivery systems. For example enzymes encapsulated by nanospheres, which are programmed for targeting cancer cells, could initiate apoptosis, the programmed cell death. As the diffusion of guest molecules in such particles with diameters of less than 100 nm is difficult to observe, a model system for diffusion measurements was developed. In section 5 the aim was to bind enzymes covalently to the pore walls of mesoporous silica thin films, in order to directly observe the chemical conversion of fluorescent substrates. Trypsin molecules were successfully attached to the silica walls via “click-chemistry” techniques and their activity was verified by fluorescence spectroscopy. In addition, it was necessary to develop a synthesis for mesoporous thin films with big domains and pores in order to track larger molecules, i. e. cancer drugs, by single molecule microscopy and characterize their diffusion analyzing their movement. In section 6 a synthesis for mesoporous thin films with 10 nm pores is described. During the analysis with single molecule fluorescence microscopy, the movement of individual dye molecules could be tracked over several microns and an oriented motion was observed.

One pre-condition for using nanospheres as drug delivery systems is a different functionalization of the inner and outer surface. An indirect localization of these functionalizations is achieved by the use of standard characterization methods, but direct visualization is able to provide more concrete results. Therefore, chapter 7 deals with a relatively new characterization method in the field of materials science, namely electron tomography, which is based on theories developed in the beginning of the last century. Since the 1970's tomography is widely used in the medical sector (CT, MRI) and with the beginning of the 1980's it has been more and more established in biology. So for example, the detailed knowledge on the structure of individual cell components was only acquired due to electron microscopy. Today the method is also applied for characterization of non-living matter and was thus chosen for direct imaging of the functionalizations of the nanoparticles mentioned above. At first, a recently developed algorithm was embedded in a conventional reconstruction software. Then discrete tomography was applied for calculating and visualizing the three-dimensional distribution of the functionalizations from only a few two-dimensional electron microscopy images.

On the one hand this work intends to present new possibilities on how the combination of characterization methods can be used to gain information not available from the individual techniques. On the other hand discrete tomography - a relatively new method in materials science - is used to image real three-dimensional nano structures with a resolution of only a few nanometers. Visualization not only facilitates the interpretation of scientific results, but also aims at contributing to a better general understanding of nano technology.

## **Résumé**

La nanotechnologie est considérée dans le monde comme une des technologies clés du 21<sup>e</sup> siècle. Déjà aujourd'hui il y a beaucoup de secteurs économiques, qui sont influencés directement ou indirectement par la nanotechnologie et le nombre de ces branches continue de s'agrandir. En général, il y a deux stratégies pour créer des nanostructures et des matériaux nanostructurés. D'une part, on peut travailler une pièce de manière technique, physique, chimique ou manuelle jusqu'à obtenir la structure voulue, par exemple un microprocesseur. D'autre part, on prend des petits éléments constitutifs, telles que des molécules individuelles, qui se regroupent elles-mêmes pour former une plus grande unité. C'est exactement ainsi que la nature procède depuis des millions d'années. A l'avenir, une combinaison de ces deux techniques offrira certainement la possibilité de produire efficacement des structures plus complexes et plus petites. Un point de départ serait la silice mésoporeuse. Ce sont des matériaux avec des pores d'environ 2 à 50 nm de diamètre, dont les parois sont en silicium dioxyde amorphe. On peut les considérer comme des verres poreux dont la surface spécifique dépasse souvent plusieurs fois celui du gel de silice. Les trois premiers chapitres se penchent donc sur les différentes structures, la synthèse et la caractérisation des silices mésoporeuses, et plus particulièrement des couches mésoporeuses.

La synthèse des systèmes de taille nano et la compréhension de leurs propriétés physiques et chimiques sont plus faciles si on visualise leur structure réelle. C'est aussi la raison pour laquelle la microscopie, et en cas de nanotechnologie plus précisément la microscopie électronique, est devenue une des méthodes de caractérisation les plus importantes. Par exemple, la structure d'une fine couche mésoporeuse avec des canaux parallèles à la surface peut être retransmise par un microscope électronique. Si des molécules fluores-

centes sont incluses dans ces canaux, on peut suivre leur diffusion avec un microscope optique, mais à cause de la limite de résolution il n'est pas possible de voir la structure. Cependant une solution pour obtenir ces deux informations sur un même échantillon et les connaissances que l'on gagne en combinant la microscopie optique et électronique, vont être présentés en chapitre 4. Il s'agissait d'une coopération avec Johanna Kirstein du groupe de Professeurs Bräuchle. Il sera décrit, comment les molécules individuelles suivent la structure réelle des pores ; comment elles sont bloquées aux limites des domaines et doivent chercher de nouveaux chemins, ainsi que l'existence de mouvements entre des canaux différents.

La diffusion des molécules dans les pores est souvent d'une importance décisive pour certaines applications. Elle dépend de l'interaction entre hôte et invité, qui repose sur les propriétés physiques et chimiques respectives des partenaires participants. L'investigation exacte et la modification ciblée de ces interactions sont essentielles pour la plupart des applications, par exemple, pour utiliser des nanosphères mésoporeuses à base de silice comme transporteur intelligent de médicaments. Ces systèmes avec enzymes incorporées pourraient être programmés pour cibler les cellules malades et y déclencher l'apoptose : suicide de la cellule, à cause d'une réaction enzymatique. Parce que la diffusion dans ces particules, dont le diamètre inférieur à 100 nm est difficile à analyser, un système modèle a été développé pour faciliter ces études. Le but du chapitre 5 était d'attacher de manière covalente des enzymes aux parois des pores pour observer directement la conversion enzymatique des substrats fluorescents. En utilisant ce que l'on appelle la chimie "click" il était possible d'attacher des molécules de trypsine aux parois des pores et de prouver leur activité par spectroscopie fluorescente. En outre, il fallait y développer une méthode de synthèse pour des couches mésoporeuses avec de grands domaines et pores pour y analyser des molécules plus larges, comme par exemple les agents cancéreux, par le biais de la microscopie de molécules individuelles et pour caractériser leur diffusion par leur mouvement. C'est pourquoi en chapitre 6 une synthèse est décrite, elle présente des couches mésoporeuses avec des pores d'environ 10 nm de diamètre. Lors des enquêtes via la microscopie optique on pouvait suivre les molécules fluorescentes sur plusieurs micromètres et un mouvement orienté a pu être constaté.

Si une nanoparticule mésoporeuse doit être employée comme transporteur des médicaments, il faut que les parois des pores intérieur et extérieur fonctionnent différemment. En utilisant des méthodes standards, il est tout à fait



possible de localiser indirectement ces fonctionnalités mais une visualisation directe permet une vérification encore plus évidente. C'est pour cela que le chapitre 7 se penche sur une méthode de caractérisation relativement nouvelle au domaine des sciences des matériaux – la tomographie électronique. Elle repose sur des théories développées au début du dernier siècle. Depuis les années 1970 la tomographie est une application très répandue dans le secteur de la médecine (scanner médical, IRM) et depuis les années 1980 elle est employée avec beaucoup de succès dans les domaines biologiques. Seulement grâce à la tomographie électronique on arrive à analyser en détail la structure organique d'une cellule. Entre-temps, cette méthode est également utilisée pour étudier la matière "morte" et c'est pour cela qu'on l'a choisit pour reproduire directement les fonctionnalités de la nanoparticule mentionnée ci-dessus. De ce fait, un algorithme développé il y a peu de temps, a été intégré dans un logiciel courant à la reconstruction. Ensuite la tomographie discrète a été appliquée pour calculer et reproduire la répartition tridimensionnelle des fonctionnalités dans la nanoparticule, à partir de quelques images à deux dimensions, obtenues par un microscope électronique en transmission.

D'une part, cette thèse montre comment une combinaison de méthodes de caractérisation permet d'acquérir de nouvelles connaissances, qui ne sont pas accessibles par informations individuelles. D'autre part, la tomographie discrète, méthode relativement nouvelle, est utilisée pour reproduire des structures réelles en trois dimensions avec une résolution de quelques nanomètres. Non seulement la visualisation rend l'interprétation des résultats scientifiques plus simple, mais elle représente aussi une opportunité de populariser la nanotechnologie.

## **Zusammenfassung**

Die Nanotechnologie wird weltweit als eine der Schlüsseltechnologien des 21. Jahrhunderts angesehen. Bereits heute sind viele Branchen direkt oder indirekt von ihr beeinflusst und laufend kommen neue Anwendungsgebiete hinzu. Prinzipiell werden zwei Strategien verfolgt, um Nanostrukturen und nanostrukturierte Materialien zu erzeugen. Zum einen kann man ein Werkstück so lange mit physikalischen, chemischen oder mechanischen Methoden bearbeiten, bis die gewünschte Struktur, beispielsweise eine Computerchip, entstanden ist, oder man benutzt kleine Bausteine, zum Beispiel einzelne Mole-

küle, die sich selbständig zu einer größeren Einheit zusammenlagern — ganz so wie es uns die Natur seit Jahrtausenden vormacht. Die Verknüpfung beider Techniken wird es uns in Zukunft wohl ermöglichen noch kleinere und komplexere Strukturen viel effizienter herzustellen. Ein Ansatzpunkt ist dabei mesoporöses Silikat - ein Material mit Poren zwischen etwa 2 und 50 nm Durchmesser und Wänden aus amorphem Siliziumdioxid. Man kann sie als poröse Gläser auffassen, deren spezifische Oberflächen aber selbst diejenigen von Silicagel oft noch um ein vielfaches übertreffen. Verschiedene Strukturen, die Synthese und die Charakterisierung von mesoporösen Silikaten, und im speziellen von dünnen mesoporösen Schichten, werden in den ersten drei Kapiteln dieser Arbeit behandelt.

Für die Entwicklung solcher Systeme und zum Verständnis deren physikalischer und chemischer Eigenschaften kann die Visualisierung, also die Abbildung der realen Struktur eine ganz entscheidende Hilfe sein, da Zusammenhänge schneller erkannt werden. Dies ist auch der Grund weshalb sich die Mikroskopie - im Bereich der Nanotechnologie v. a. die Elektronenmikroskopie - zu einer der wichtigsten Charakterisierungsmethoden überhaupt entwickelt hat. Beispielsweise kann die Struktur von dünnen mesoporösen Schichten mit Kanälen parallel zur Oberfläche mit Hilfe eines Transmissionselektronenmikroskops abgebildet werden. Bringt man fluoreszierende Moleküle in diese Kanäle, dann kann man im optischen Mikroskop sehr genau deren Wanderungsbewegungen verfolgen, aber es ist aufgrund der Auflösung nicht möglich die Struktur abzubilden. Wie es dennoch gelingt, beide Informationen über ein und dieselbe Probe zu erhalten und welche neuen Erkenntnisse durch die Kombination von optischen und elektronenmikroskopischen Daten gewonnen werden können, beschreibt Kapitel 4. In Zusammenarbeit mit Johanna Kirstein aus der Arbeitsgruppe von Professor Bräuchle konnte gezeigt werden, wie Moleküle der realen Porenstruktur folgen, wie sie an Domänengrenzen zurückgehalten werden und sich neue Wege suchen müssen, oder auch dass Bewegungen zwischen verschiedenen Poren möglich sind.

Für potenzielle Anwendungen ist die Diffusion von Molekülen innerhalb der Poren meist von entscheidender Bedeutung. Sie ist abhängig von der sogenannten Wirt-Gast Wechselwirkung, die auf den jeweiligen chemischen und physikalischen Eigenschaften der beteiligten Partner beruht. Eine genaue Untersuchung und gezielte Veränderung dieser Wechselwirkung ist für die meisten Applikationen essentiell. So z. B. für die Verwendung von mesoporösen Nanosphären auf Silica-Basis als intelligente Medikamententransporter. Da

das Diffusionsverhalten in diesen Partikeln mit weniger als 100 nm Durchmesser extrem schwer zu untersuchen ist, galt es ein Modellsystem für solche Untersuchungen zu entwickeln. In Kapitel 5 war es Ziel Enzyme kovalent an die Porenwände zu binden, um eine direkte Beobachtung der Umsetzung von fluoreszierenden Substraten zu ermöglichen. Nanosphären mit integrierten Enzymen könnten gezielt auf kranke Zellen programmiert werden und dort über enzymatische Reaktionen beispielsweise die Apoptose, also gewissermaßen das Selbstmordprogramm der Zelle, auslösen. Mit Hilfe der sogenannten "Click-Chemie" konnten Trypsinmoleküle erfolgreich an die Porenwände gebunden werden und mittels Fluoreszenzspektroskopie wurde deren Aktivität nachgewiesen. Zusätzlich war es nötig eine Synthesemethode zu entwickeln, die mesoporöse Filme mit großen Domänen und Poren liefert. Damit ist es möglich größere Moleküle, wie zum Beispiel Wirkstoffe gegen Krebs, mittels Einzelmolekülmikroskopie im Inneren der Poren zu verfolgen und über deren Bewegung ihre Diffusion zu charakterisieren. Deshalb wird in Kapitel 6 eine Synthese beschrieben, die durch langsames Herausziehen eines Substrates aus einer sauren Silica-Lösung mesoporöse Filme mit etwa 10 nm großen Poren liefert. Bei ersten Untersuchungen mittels Einzelmolekülfluoreszenzmikroskopie konnten einzelne Farbstoffmoleküle in diesen Filmen über mehrere Mikrometer hinweg verfolgt und orientierte Bewegungen nachgewiesen werden.

Für die Verwendung als Medikamententransporter ist es nötig die Porenwände im inneren der Nanopartikel und die äußere Oberfläche unterschiedlich zu funktionalisieren. Eine indirekte Lokalisierung von Funktionalitäten ist mit Standardmethoden durchaus möglich, aber auch hier ist die direkte Visualisierung der bessere, da eindeutiger Nachweis. Kapitel 7 beschäftigt sich deshalb mit einer relativ neuen Charakterisierungsmethode im Bereich der Materialwissenschaften, der Elektronentomographie. Basierend auf Theorien, die Anfang des letzten Jahrhunderts entwickelt wurden, findet die Tomographie seit den 1970er Jahren breite Anwendung im medizinischen Bereich (CT, MRT) und erfreut sich seit den 1980er Jahren immer größerer Beliebtheit in der Biologie. Wirklich detailliert konnten der Aufbau und die Struktur von einzelnen Zellbausteinen erst mit Hilfe der Elektronentomographie untersucht werden. Inzwischen findet die Methode auch Anwendung in den Materialwissenschaften und soll deshalb auch die Funktionalisierungen des oben angesprochenen Nanopartikels direkt abbilden. Dazu wurde ein erst kürzlich entwickelter Algorithmus in eine gebräuchliche Rekonstruktionssoftware

eingearbeitet, um dann mittels diskreter Tomographie aus wenigen zweidimensionalen elektronenmikroskopischen Aufnahmen die Verteilung der Funktionalisierung innerhalb des Nanopartikels im dreidimensionalen Raum zu berechnen und darzustellen.

Diese Arbeit möchte neue Möglichkeiten aufzeigen, wie zum einen die Kombination von Charakterisierungsmethoden verwendet werden kann, um Erkenntnisse zu gewinnen, die so aus den einzelnen Informationen nicht zugänglich sind. Zum anderen wird mit der diskreten Tomographie eine in der Praxis sehr neue Methode verwendet, um reale dreidimensionale Strukturen mit einer Auflösung von wenigen Nanometern abzubilden. Eine Visualisierung erleichtert nicht nur Wissenschaftlern die Interpretation von Forschungsergebnissen, sondern sie trägt auch dazu bei, die Nanotechnologie der breiten Bevölkerung verständlich näher zu bringen.

# Contents

## INTRODUCTION

<b>1</b>	<b>Setting the scene</b>	<b>2</b>
1.1	'top down' and 'bottom up' . . . . .	2
1.2	Porous materials by 'bottom up' . . . . .	5
1.3	Periodic mesoporous silica . . . . .	6
1.4	Investigating mesostructures . . . . .	8
1.4.1	Common techniques . . . . .	8
1.4.2	Diffusion measurements . . . . .	9
1.4.3	Discrete electron tomography . . . . .	10
1.5	Motivation . . . . .	12
<b>2</b>	<b>Basics and present state of research</b>	<b>16</b>
2.1	Formation mechanism of mesoporous materials . . . . .	16
2.2	Synthesis of mesoporous (thin) silicate films . . . . .	17
2.3	Structures of mesoporous materials . . . . .	20
2.4	Characterization methods . . . . .	21
2.4.1	Electron microscopy . . . . .	21
2.4.2	Electron Tomography . . . . .	24
2.4.3	Single molecule fluorescence microscopy . . . . .	31
2.4.4	1D X-ray diffraction . . . . .	33
2.4.5	X-ray reflection . . . . .	34
2.4.6	2D X-ray diffraction . . . . .	36
2.4.7	Ellipsometry . . . . .	36
2.4.8	Infrared and Raman spectroscopy . . . . .	38

## EXPERIMENTAL METHODS

<b>3</b>	<b>Experimental methods</b>	<b>42</b>
3.1	Starting materials . . . . .	42
3.2	Instruments . . . . .	43
3.3	Synthesis of mesoporous films used in section 4 . . . . .	45
3.3.1	Pre-mixed stock solutions . . . . .	45
3.3.2	General synthesis . . . . .	45

3.4	Synthesis of enzyme functionalized mesoporous thin silica films .	46
3.4.1	sp-Functionalization of trypsin . . . . .	46
3.4.2	Chloropropyl functionalized films by cocondensation . . . .	46
3.4.3	Template removal . . . . .	47
3.4.4	Azide exchange . . . . .	47
3.4.5	Enzyme attachment by click reaction . . . . .	47
3.5	Synthesis of large domain mesoporous thin silica films . . . . .	47

## RESULTS AND DISCUSSION

<b>4</b>	<b>Visualizing single-molecule diffusion in mesoporous materials</b>	<b>50</b>
4.1	Adjusting film thickness . . . . .	51
4.2	Synthesis of thin mesostructured silica films with pure phases . .	53
4.2.1	Films with 2D-hexagonal arrangement of rod-like pores. . .	53
4.2.2	Films with cubic structures. . . . .	53
4.2.3	Films with lamellar structure. . . . .	54
4.3	Final recipe and reproducibility . . . . .	56
4.4	Using silicon nitride membranes as substrates . . . . .	57
4.5	Widefield microscopy and Single Particle Tracking . . . . .	58
4.6	Transmission electron microscopy . . . . .	59
4.7	Overlay . . . . .	61
4.8	Results . . . . .	63
<b>5</b>	<b>Enzymes covalently bound to the surface of mesoporous thin films</b>	<b>70</b>
5.1	Covalent binding . . . . .	71
5.2	Synthesis . . . . .	73
5.3	Activity measurement . . . . .	74
5.4	Results . . . . .	75
<b>6</b>	<b>Mesoporous thin films as sample systems for silica based drug de- livery systems</b>	<b>80</b>
6.1	Structure and pore size . . . . .	80
6.2	Functionalization and template removal . . . . .	81
6.3	Domain size . . . . .	83
6.4	Results . . . . .	86

<b>7 Visualizing nano scale objects by discrete tomography</b>	<b>90</b>
7.1 Masked SIRT algorithm . . . . .	93
7.2 Alignment using the “barycenter” . . . . .	93
7.3 Setting up the mask . . . . .	94
7.3.1 Individual particles . . . . .	94
7.3.2 Continuous membranes and metal layers . . . . .	94
7.4 DART . . . . .	95
7.5 Colloidal Mesoporous Silica Nanoparticle . . . . .	96
7.5.1 Acquisition and projection pre-processing . . . . .	96
7.5.2 Comparing original and DART projections . . . . .	97
7.6 Nanopore in a silicon nitride membrane . . . . .	102
7.6.1 Image acquisition . . . . .	102
7.6.2 Mask set-up and DART reconstruction . . . . .	103
7.6.3 Comparing DART reconstructions derived from different SIRT starting volumes . . . . .	103
7.7 Results . . . . .	104

## CONCLUSION

<b>8 Conclusion</b>	<b>108</b>
---------------------	------------

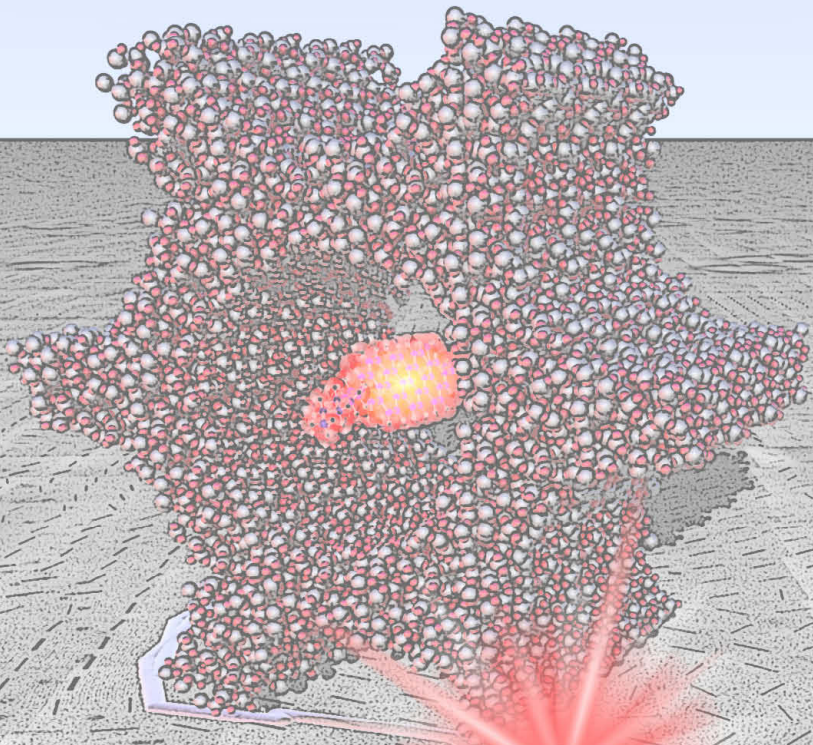
## APPENDIX

<b>9 Appendix</b>	<b>112</b>
9.1 Literature . . . . .	112
9.2 Supplementary figures . . . . .	125
9.2.1 Basics - 1D-XRD . . . . .	125
9.2.2 Filmthickness . . . . .	126
9.2.3 2D-hexagonal phase . . . . .	129
9.2.4 Cubic phase . . . . .	131
9.2.5 Lamellar phase . . . . .	134
9.3 Supplementary tables . . . . .	138
9.4 Program code . . . . .	140
9.4.1 Determining the center of PS-beads in TEM maps . . . . .	140
9.4.2 Calculating the FFT directors of TEM maps . . . . .	141

9.4.3 Calculating scaling, rotation and translation of optical images with respect to the TEM map . . . . .	142
9.5 CD content . . . . .	146
9.6 List of abbreviations . . . . .	148
9.7 Curriculum vitae . . . . .	151
9.8 Publications . . . . .	153
9.9 Presentations . . . . .	153
9.10 Meetings, Awards . . . . .	153



# 1



**INTRODUCTION**

EXPERIMENTAL METHODS

RESULTS AND DISCUSSION

CONCLUSION

APPENDIX



## 1 Setting the scene

Scratch-resistant automobile paint<sup>1</sup>, 800 million transistors on a few square centimeters<sup>2</sup> and invisible sunscreens with high sun protection factor but without allergenic organic UV absorbers<sup>3</sup> — these are only three examples of developments in nanotechnology recently put on the market.

“Nano” actually means ‘dwarf’ (greek *νάνος*) and denotes as prefix (symbol n) in the SI system of units a factor of  $10^{-9}$ . In the chemical and physical context particles and structures in the nanometer range are implied here. By approaching this scale one leaves more and more the “normal” macroscopic world and often reaches a completely different one, dominated by the physical rules of quantum mechanics. For example, the electronic structure of nanoparticles is modified in comparison to the bulk material in such a way that their magnetic properties can change from diamagnetic into paramagnetic and from ferromagnetic into super paramagnetic, or the continuum conduction band can split of into discrete levels<sup>4-6</sup>. An impressive proof is given by the different colors of nanoparticle solutions. For instance CdTe semiconductor nanoparticles change their color from blue (2.3 nm diameter) to red (5.5 nm diameter)<sup>7</sup> and colloidal gold suspensions can be red (15 nm in diameter) as well as blue (30 nm in diameter).<sup>8</sup>

Today about 750 companies in Germany are involved in the development, application, and sales and marketing of nanotechnological products and approximately 63,000 industry jobs can be directly or indirectly attributed to this field.<sup>9</sup> In 2007 nanotechnology was incorporated into \$147 billion in manufactured goods – worldwide. This is approximately the triple of 2005, and in 2015 an estimated amount of up to \$3.1 trillion in global manufactured goods will incorporate nanotechnology, which is about 15% of total output.<sup>10,11</sup> In the same year it is expected that nearly every industrial sector will be influenced by nanotechnology, particularly chemistry, life science and electronics.<sup>12</sup>

Regarding all these aspects it is not surprising that the German federal ministry of education and research (BMBF) considers nanotechnology as one of the most promising technologies of the 21st century.<sup>13</sup>

### 1.1 ‘top down’ and ‘bottom up’

There are two principal approaches designing nanostructures. On the one hand the ‘bottom up’ approach and on the other hand the ‘top down’ approach.

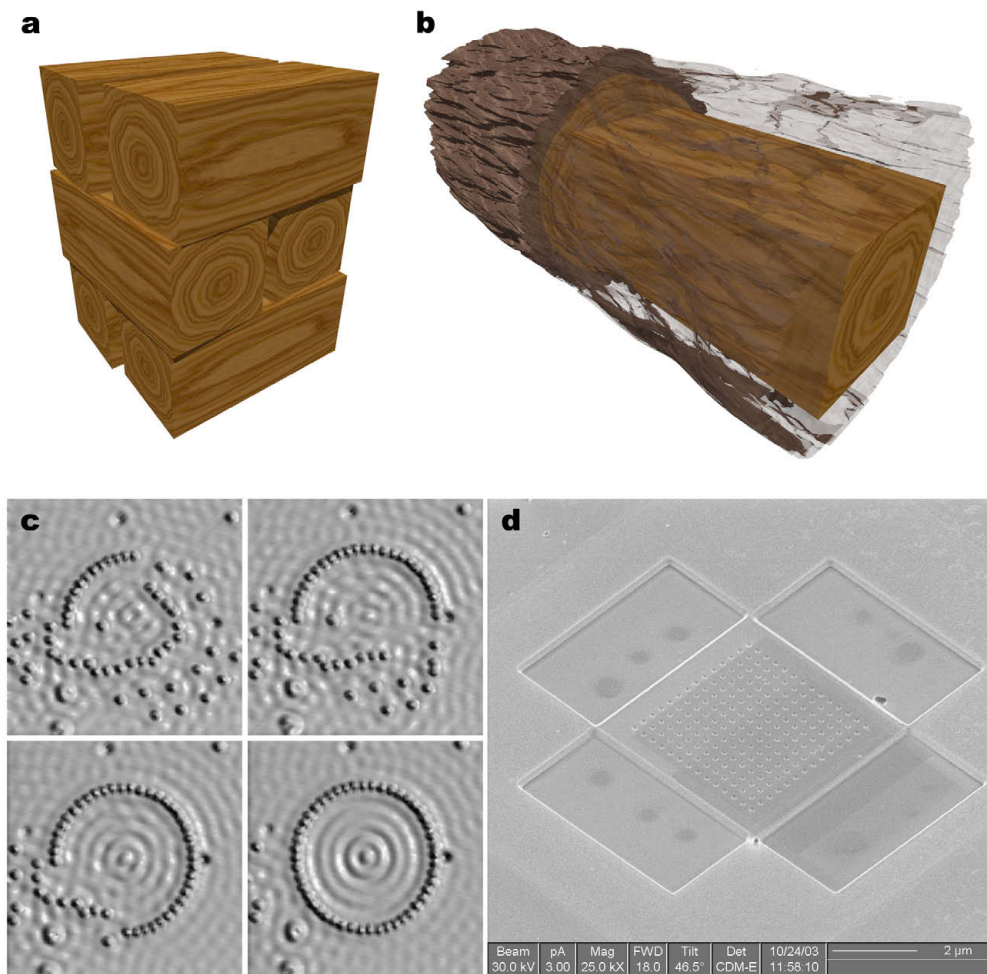


**Figure 1.1:** **a** The 'bottom up' approach is comparable to the stacking of wooden building blocks. This means the creation of structures or objects by the use of smaller units. **b** But these wooden blocks themselves are made by a 'top down' approach, because they have to be cut out of a bigger piece of wood. Therefore, 'top down' means mechanical, chemical or physical downsizing or modification of macroscopic objects or structures. **c** Spatial image of the eigenstates of a quantum corral. Ring constructed on a Cu(111) surface using atomic force microscopy to arrange 48 Fe atoms in a 'bottom up' approach. Average diameter of the ring (atom center to atom center) is 142.6 Å.<sup>14-16</sup> **d** The Figure shows an example of a nano-porous silicon membrane 100 nm thick that was produced in a 'top down' approach using a Focused Ion Beam Microscope to sputter an array of 42 nm diameter holes through the thickness of the membrane.<sup>17</sup>

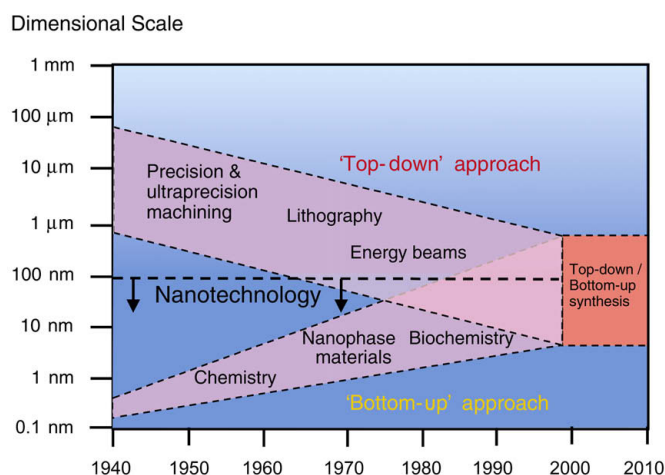


**Figure 1.2:** Evolution of the dimensional ranges of 'top down' and 'bottom up' methods with time.<sup>18</sup> Both have currently reached a region where they can overlap.

In the first case molecules or atoms are selectively connected to bigger structures or particles in the nanometer range. Transferred into the macroscopic world this is comparable with Lego<sup>®</sup> bricks or wooden building blocks small children use to build houses or towers with. The wooden blocks themselves, however, are made by a 'top down' approach, because they have to be cut out of a bigger piece of wood. Or expressed in a more scientific way: 'Top down' is the mechanical, chemical or physical downsizing or modification of macroscopic objects and structures (see figure 1.1). Nearly the whole fabrication process of integrated circuits, computer chips and memory devices is based on this approach. While the great chip manufacturers produce their integrated circuits currently in the 45-nm regime<sup>19</sup> and prototypes of even smaller transistors down to 10 nm<sup>20</sup> were already developed, the conventional methods, like lithography or electron beam treatment, face increasing technological and fundamental challenges. Overcoming these difficulties is certainly possible, but associated with enormous efforts and costs.<sup>21,22</sup> 'Bottom up', however, is a rather cheap method, which even allows the assembly of complex 3D structures in large quantities. Regarding the evolution with time of the dimensional ranges they address, both methods are currently overlapping (see figure 1.2) and there is no doubt that their combination will lead to exciting new hybrid methods of manufacture.<sup>23</sup>

## 1.2 Porous materials by 'bottom up'

One possible starting point for such hybrid methods are porous materials often used as filters, membranes, adsorbents or catalysts. A classical miscellaneous example is activated carbon used in gas masks and extractor hoods, for water treatment and – loaded with palladium – as hydrogenation catalyst in chemical reactions. It is synthesized by carbonization of organic materials at high temperatures (above 600°C). Unfortunately, this procedure does not permit a precise control over pore size or shape and results in a broad pore size distribution. By contrast, the 'bottom up' approach is a suitable way for creating porous materials with defined pores. Precursors of the later framework and templating molecules arrange themselves in such a way that after precursor cross-linking and template removal a solid porous framework with a defined pore system in the nanometer range is left. In zeolite synthesis, for example, hydrolyzed silica and alumina species act as precursors and alkyl ammonium, water, sodium cations, etc. template the structure.<sup>24</sup> Zeolites are also produced on a large scale. These tectosilicates, composed of a three-dimensional framework of aluminum, silicon and oxygen atoms, have defined cavities and channels incorporating water and/or cations. They are used as desiccants for gases and solvents, for ion exchange, especially as builder in laundry detergents, and in cryosorption pumps. Zeolites containing noble metals can catalyze isomerizations (linear into branched alkanes), as well as cracking and other reactions (methanol into hydrocarbons, benzene into ethyl benzene or toluene, etc.). That is why they take on a central role in petrochemistry. But applications are often limited by the pore size, which is still in the microporous range (< 2 nm) for zeolites as well as for the recently developed aluminophosphates<sup>25</sup>. Moreover, structures with bigger pores tend to have decreased stability and therefore only zeolites with pores up to 1 nm are used in industrial applications.<sup>26</sup> Once bigger or bulky molecules should be converted or more complex active centers, like biomolecules or metal complexes are needed, this limitation is quickly exceeded. Very recently several promising approaches try to overcome this problem. For example, metal and covalent organic frameworks (MOFs and COFs with large open pore systems see figure 1.3) were discovered in the mid-nineties<sup>27,28</sup> and 2005<sup>29</sup>, respectively. With pore sizes up to 3 nm, densities down to 0.17 g/cm<sup>3</sup> and surface areas up to 4500 m<sup>2</sup>g<sup>-1</sup>, their porous qualities are several times better than the ones of zeolites.<sup>32</sup> Nevertheless, for many applications, particularly in the area of

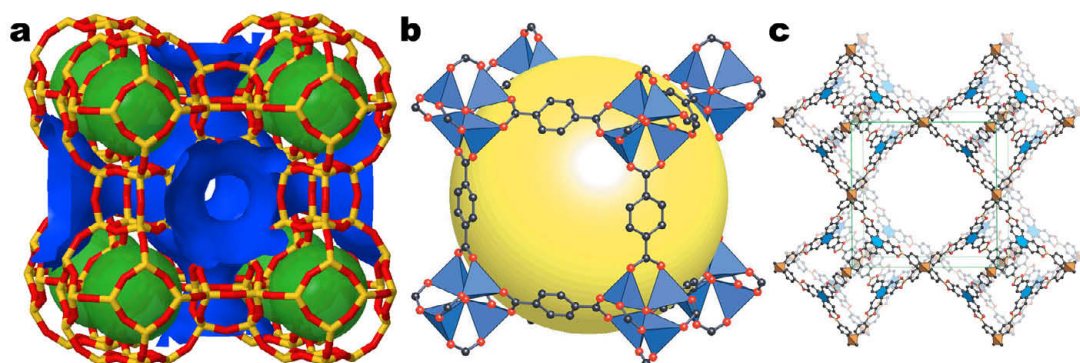


**Figure 1.3:** **a** Crystal structure of zeolite A (LTA). Si-O bonds are red, Al-O bonds are yellow. Na and H atoms are not shown. Pore size approximately 0.4 nm **b** Structure of the metal organic framework MOF-5 shown as  $ZnO_4$  tetrahedra (blue polyhedra) joined by benzene dicarboxylate linkers (O, red and C, black) to give an extended 3D cubic framework with interconnected pores of 0.8 nm aperture width and 1.2 nm pore (yellow sphere) diameter. (Yellow sphere represents the largest sphere that can occupy the pores without coming within the van der Waals size of the framework).<sup>30</sup> **c** Atomic connectivity and structure of the covalent organic framework COF-108. Hydrogen atoms are omitted for clarity. Carbon, boron, and oxygen atoms are represented as gray, orange, and red spheres, respectively. Diameter of biggest cavity 30 nm.<sup>31</sup>

heterogeneous catalysis, their window or pore sizes can still be too small.

### 1.3 Periodic mesoporous silica

Not long ago, bigger pores could only be provided by some amorphous materials, like silica gel, porous glasses or certain polymers. These materials can be synthesized with pores in the mesoporous region, corresponding to a diameter in the range between 2 and 50 nm, based on the IUPAC classification of porous materials. But as in the case of activated charcoal mentioned above, these materials often show broad pore size distributions. Only since the pioneering work of Beck et al.<sup>33</sup> (MCM) and Inagaki et al.<sup>34</sup> (FSM) there are mesoporous materials with periodically ordered structures and narrow pore size distributions. Shortly thereafter many other mesoporous systems resulted from these discoveries<sup>35-38</sup>, one very important in 1998, the so called SBA-family<sup>39-41</sup>. The synthesis of all these materials is based on a self-assembly mechanism. Pre-hydrolyzed silicon species (e.g. tetraethylorthosilicate) and a supramolecular template arrange themselves into an ordered structure. Adjacent silanol groups (Si-OH) can condense and build-up an amorphous, glass-like silicon oxygen framework, surrounding the template. Removal of the tem-

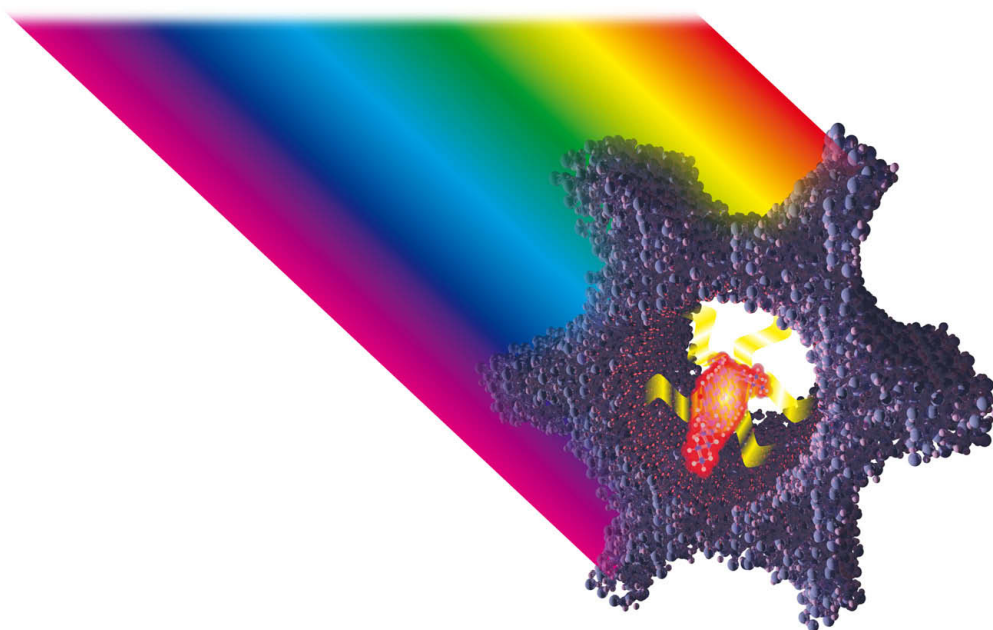


**Figure 1.4:** Illustration of energy transfer from organic chromophores in the framework to a dye in the mesochannels of PMO. The transfer of excitation energy from the framework donors to acceptors in the mesochannels is promoted and the dyes remain separated even at high concentrations. Therefore the luminescence of the dyes doped in the channels is enhanced in comparison to a dye solution with the same concentration.

plate molecules, for example by calcination, UV light, ozonization or in an oxygen plasma, results in a mesoporous material with defined pores, high surface area ( $>1000 \text{ m}^2 \text{ g}^{-1}$ ) and big pore volume (up to  $1 \text{ ml g}^{-1}$  and more). This is quite comparable with zeolites, but the pore diameters can reach 20 or more nanometers, depending on the used template.<sup>41</sup>

Periodic mesoporous materials, such as MCM or SBA, can assume a variety of structures<sup>42,43,39</sup>, and their widely tunable properties make them attractive hosts for numerous applications. They could be used for example as low dielectric constant material in integrated circuits<sup>40,44</sup>, as photo luminescent material for light emitting diodes or displays<sup>45,46</sup>, as building blocks for photonic crystals<sup>47,48</sup> or as light harvesting material<sup>49</sup> (see figure 1.4). In addition, they combine the advantages of activated charcoal (high surface area and big pores) with the ones of zeolites (narrow pore size distribution) and they represent - also because of their high mechanical and thermal stability - an excellent substrate for heterogeneous catalysis. Even though mesoporous materials have a lower acidity and hydrothermal stability and therefore will not replace



zeolites in the near future, they could be very useful as catalysts in the synthesis of fine chemicals.<sup>50</sup> Thereby catalytically active metal atoms, molecules or complexes are either directly integrated into the silica framework during synthesis by cocondensation<sup>51,52</sup> or they are attached to the silica surface in an additional step after synthesis<sup>53-57</sup>, referred to as post-grafting.<sup>58-61</sup> Further applications of mesoporous materials could be in the analytical sector, e.g. as stationary phase in liquid chromatography or as specific adsorbents.

Regarding the applications of mesoporous materials mentioned above (e.g. low  $k$  material or LEDs), there was a great interest in finding a way of synthesizing these structures in the form of thin layers - preferably on silicon wafers with the same techniques already developed for chip manufacturing. In 1994 Ogawa was the first, obtaining thin mesostructured layers by spin coating<sup>62</sup> and since then a broad variety of synthesis techniques was developed. Widely used are spin- and dip-coating processes to produce layers with thicknesses ranging from several ten nanometers to several micrometers. Again, through functionalization - during synthesis or afterwards - their application spectrum can be strongly extended. Hence, these films can be used as sensors, permselective membranes or photovoltaic cells.<sup>63</sup> Moreover, other mesoporous materials such as mesoporous TiO<sub>2</sub> films are promising electrode materials for dye-sensitized solar cells.<sup>64,65</sup> 2D hexagonal ordered mesoporous films can also serve as a model system for drug delivery applications, e.g. mesoporous silica nanospheres. The goal is a mesostructured silica nanoparticle smaller than 100 nm, loaded with drugs inside and decorated with caps and required ligands such as proteins outside.<sup>66,67</sup> The proteins can provide selective endocytosis into diseased cells, e.g. tumor cells, and by the associated pH change the caps can open (see 'presentations/poster2.pdf' on the supplementary CD), so that healthy cells are not affected. Because of the toxicity of the presently used cancer drugs, an intelligent encapsulation would significantly enhance their effectivity.

### **1.4 Investigating mesostructures**

#### **1.4.1 Common techniques**

Although mesostructured materials are often non-crystalline, the main method determining the structure type is X-ray diffraction. Bulk material is often investigated by simple one-dimensional powder diffraction, whereas thin films usually have to be studied by two-dimensional grazing incidence small-angle



X-ray scattering (2D-GISAXS). But both measurements only provide general information on the whole sample. For structural information at distinct points of the sample the instrument of choice is electron microscopy. By scanning electron microscopy (SEM) the particle morphology is determined and in many cases also bigger pores (>5 nm) can be resolved, but it is a surface-sensitive technique, which does not provide much information about the internal structure. Transmission electron microscopy on the other hand images through the specimen, but sample preparation is often more complex and time-consuming. Nevertheless, as the resolution can be in the sub-nanometer range, it is the best method for imaging mesostructures, even of samples with small pores.

Another useful information can be obtained by characterizing the cavities of template free mesostructures. Pore size distribution, pore diameter and volume, for example, are obtained from N<sub>2</sub>- and Kr-sorption measurements or Hg-porosimetry, whereas porosity of thin films can be extracted from ellipsometry data. Functionalizations of the framework are often visible in IR, Raman, or solid state NMR spectra, or in TGA or DSC (both are thermoanalytical methods to measure either weight change or heat flux as a function of temperature). With all these measurements one obtains information about the framework structure, its atomic composition and its functionalization, which are the main characteristics of a mesostructured material and in the end define its potential applications.

#### **1.4.2 Diffusion measurements**

For nearly all applications the interaction between the mesostructured framework itself and molecules incorporated in this structure is critical; this is also known as host-guest interaction. A measurable parameter strongly influenced by this interaction is the diffusion of the guests within the pores of the host, specified by a diffusion constant. Diffusion constants are measured with different techniques. Pulsed-field gradient NMR spectroscopy<sup>68</sup> and quasi-elastic neutron scattering<sup>69</sup> provide the opportunity to probe the diffusional behavior of any diffusing species, like water, methane or xenon. Needless to say that at least neutron scattering is a method only available in a handful of laboratories and also PFG-NMR requires very special apparatus. Alternative methods include fluorescence correlation spectroscopy (FCS)<sup>70</sup> and fluorescence recovery after photobleaching (FRAP)<sup>71</sup> measurements. These are restricted to comparatively large fluorescent dye molecules, but in the case of mesoporous materials

with pore diameters above 2 nm this is not a serious limitation.

All these diffusion measurements are averaging over hundreds and thousands or even more molecules and are therefore not suitable for characterizing single domains within the mesostructured material. A method with a spatial resolution up to two orders of magnitude better than FCS is single particle tracking (SPT). SPT provides individual information on the diffusion of single molecules and permits the identification of sub populations. In some cases it is even possible to see changes in the diffusional behavior within one individual trajectory.

### 1.4.3 Discrete electron tomography

Since its invention in the 1930's electron microscopy (EM) has revolutionized imaging of sub-micrometer structures in the fields of biology and materials science. For the first time it was possible to overcome the resolution limit of light microscopy defined by Abbe and to see the fine details of the interior structures of organic cells (nucleus, mitochondria, etc.), which was just not possible using light microscopes. With the arrival of integrated circuits in the 1970's and their continuous miniaturization, today the electron microscope is also used for quality control and failure analysis in semiconductor device fabrication. Approximately at the same time the first X-ray computed tomography (CT) systems came on the market and revolutionized medical imaging. In CT a series of two-dimensional X-ray images taken around a single axis of rotation is used to generate a three-dimensional image of an object by mathematical algorithms.

Electron tomography (ET) is the combination of both techniques (EM and CT) and allows deep insights into nanostructured objects in three dimensions. As long as no automatic acquisition of image series was possible this method was applied to very few biological specimens.<sup>72-74</sup> But since electron microscopes are computer controlled and image series can be obtained almost in a fully automated manner, it is possible to apply ET also to radiation-sensitive samples,<sup>75</sup> resulting in several highly rated publications in a short time.<sup>76-79</sup> In materials science up to now this method is not used as extensively as in biology, but there are also some interesting results, for example, TEM studies analyzing the 3D structure of mesoporous materials<sup>80-82</sup>. Other groups have studied the size distribution and 3D location of single NiO crystallites<sup>83</sup>, gold and zirconium oxide<sup>84,85</sup> in the pores of SBA-15. Despite the great po-

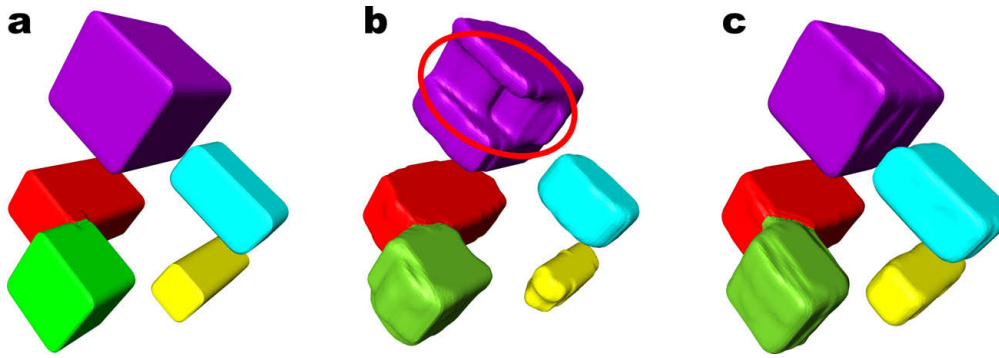


**Figure 1.5: Comparing standard and discrete tomography.** **a** The initial three-dimensional hypothetical shape. From this structure nine projections are calculated at different tilt angles of  $-60^\circ$ ,  $-45^\circ$ ,  $-30^\circ$ ,  $-15^\circ$ ,  $0^\circ$ ,  $15^\circ$ ,  $30^\circ$ ,  $45^\circ$  and  $60^\circ$ . **b** With a commonly used algorithm, called simultaneous iterative reconstruction technique (SIRT), the reconstruction suffers from highly visible artifacts (marked by red circle). This is due to the small number of projections and the missing-wedge problem (see section 2.4.2). **c** Using a recently developed reconstruction algorithm (discrete algebraic reconstruction technique - DART) these artifacts are clearly minimized, only some objects appear slightly bigger in the reconstruction.

tential of this method, its application is rather complex. After the tomographic reconstruction, artifacts from Fresnel diffraction and diffraction contrast are present.<sup>84</sup> Especially at high resolutions, ET of nanostructured materials face the same problems as in biology, namely missing-wedge artifacts and radiation damage (see section 2.4.2). A solution to overcome these problems is discrete tomography, meaning in general the use of additional information beside the projections to calculate the reconstruction. In the case of nanostructured materials, for example, the number of different materials and their electron diffraction capability is included in the reconstruction algorithm. In comparison to ‘normal’ ET, discrete tomography yields the same reconstruction quality with significantly fewer projections and much higher qualities with the same number of projections, respectively.<sup>86,87</sup> In figure 1.5 this is explained on the basis of a hypothetical nanostructure with five different materials. Artifacts that occur due to reconstruction with a commonly used algorithm, called simultaneous iterative reconstruction technique (SIRT), are clearly visible (fig 1.5b). Whereas with discrete tomography, using the discrete algebraic reconstruction technique (DART)<sup>88,89</sup>, the shape of the individual objects is retained.

## **1.5 Motivation**

Often, a better understanding of complex systems is achieved by visualization, e.g., with diagrams, figures or pictures. Normally these are abstract representations of information gained from real data. Crystal structures obtained from diffraction patterns are good examples. The nice three-dimensional illustrations with face-sharing octahedra, edge-sharing tetrahedra or trans-connected octahedral chains, etc., don't represent the real structure but a 'smoothed' average over the whole sample. Local defects or domain boundaries are only accessible by indirect approaches, but not revealed directly. Clearly this is often the best way describing a material in general - to show its normal behavior and properties - but, if there are questions regarding a certain sample location or one distinct structural element out of a thousand, new visualization techniques are necessary.

Section 4 of this work deals with a problem concerning the diffusion of single molecules within the pores of a mesoporous silica material. By following the pathway of an individual molecule, one can observe structured, as well as unstructured movement, bouncing back at distinct sites or complete immobility. Although it is quite obvious that the behavior depends on the local structure, it was not yet possible to correlate the structure with the diffusional trajectory. Therefore, the diffusion pathways of individual molecules should be followed by single molecule tracking, and TEM was chosen for structure characterization in the same area. By superimposing optical and electron microscopy data a direct correlation of diffusion behavior and mesoporous structure should be possible.

At a first glance, the aim of section 5 looks quite different: Enzymes should be incorporated into mesoporous films by covalent bonding. But finally this is the basis for direct observation of enzymatic reactions within the pores of mesoporous thin films. Those films should serve as model systems for intelligent drug delivery techniques, based on colloidal mesoporous silica (CMS).

It is also planned to carry out diffusion studies in these model systems, determining the influence of functionalized pore walls. Hence, section 6 is about increasing the domain size of mesoporous thin films, in order to get longer path-ways and more defined, ordered channel systems for fundamental studies of diffusion in such hosts.

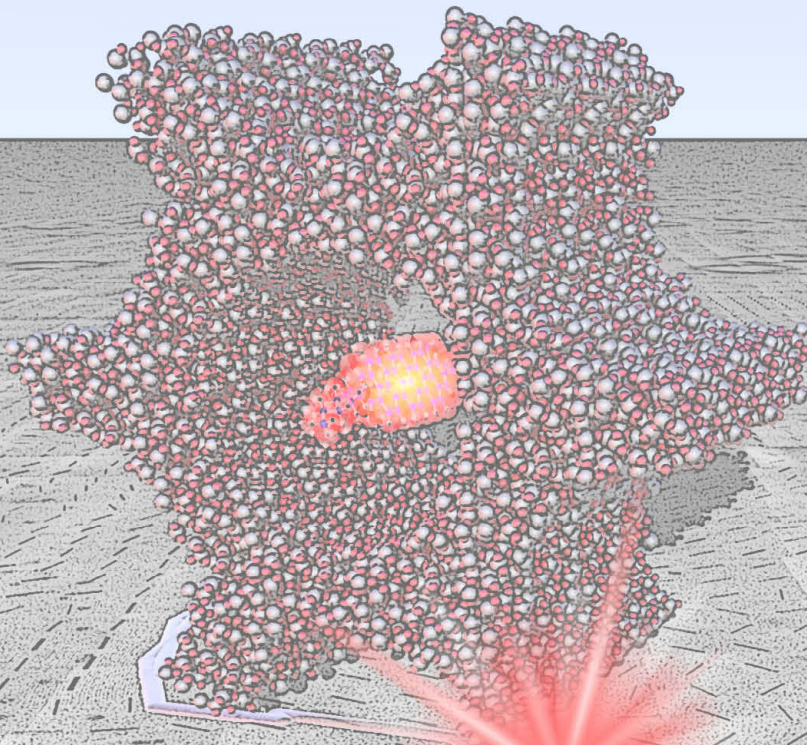
Section 7, finally, addresses the topic of electron tomography - a technique used to reveal the real three-dimensional structure of nanoscale objects, com-

parable to computerized tomography for medical examinations. A recently developed reconstruction algorithm should be applied to visualize the highly electron sensitive CMS particles, mentioned above, in a quality not achievable by conventional methods.





# 2



**INTRODUCTION**

EXPERIMENTAL METHODS

RESULTS AND DISCUSSION

CONCLUSION

APPENDIX



## 2 Basics and present state of research

This chapter focuses on formation mechanisms, structures and general characterization methods of ordered mesoporous materials. Further information is given by several excellent reviews summarizing synthesis, characterization and applications of this class of materials<sup>50,90-103</sup> in general and of mesoporous thin films<sup>104-107</sup> in particular, as well as novel developments in this field of research in the past 15 years.

### 2.1 Formation mechanism of mesoporous materials

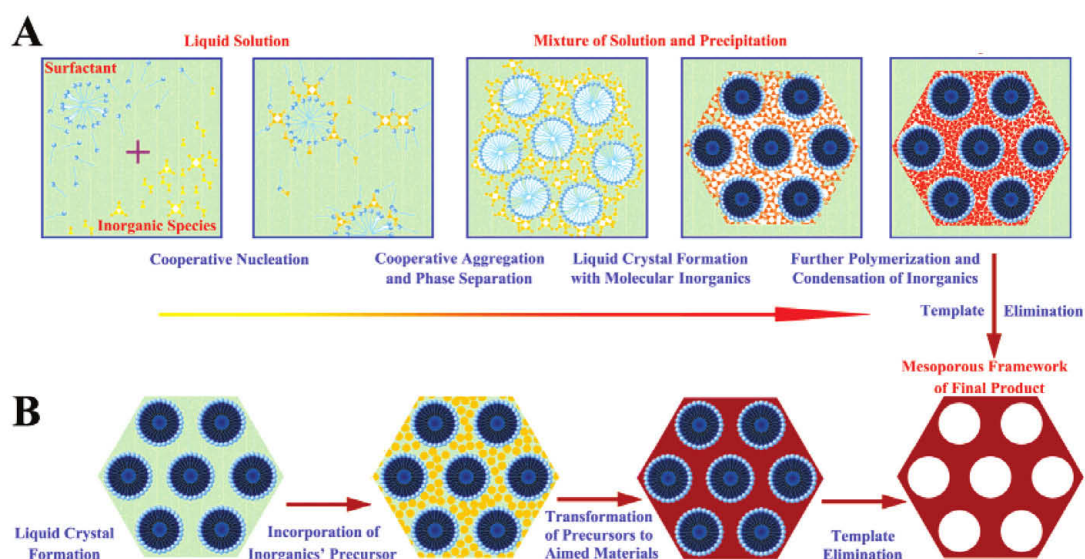
The synthesis strategy for mesoporous materials was more or less adapted from zeolite synthesis<sup>24</sup> using organic or inorganic templates. Building blocks, so called precursors, are organized around supramolecular surfactant structures by non-covalent interactions between themselves and the templating molecules. Based on the first mechanism postulated by Beck and co-workers<sup>33,42</sup> today two main pathways for template directed synthesis of mesoporous materials are generally accepted, cooperative self-assembly (CSA) and “true” liquid-crystal templating (TLCT) processes.<sup>103,108</sup>

TLCT implies the formation of micelles above the critical micelle concentration of the template. These micelles (e.g. spheres or rods) arrange themselves in an ordered way to form the structure (e.g. cubic or hexagonal). Inorganic precursor molecules fill up the free space between the micelles and after condensation the inverse micellar structure is obtained (see figure 2.1 route B).

But as mesoporous materials can also be synthesized far below the critical micelle concentration of the template,<sup>94</sup> the CSA mechanism<sup>96</sup> seems to be more accurate at least for some synthesis strategies. It postulates at first the formation of silicate oligomers, interacting with free template molecules. Further grow leads to silicate polymers, capable to bind even more template. Only at this point the structure is formed and continues growing, whereas the micelles just serve as a sort of reservoir for template molecules (see figure 2.1 route A).

In the end, surfactant removal yields the desired mesoporous materials. Even though there are novel mesoporous frameworks with at least crystal-like pore walls,<sup>65,109-111</sup> a defined crystalline framework for mesoporous materials could not be observed.<sup>112</sup> By using different surfactants (see table 1) and precursors (see table 2), a variety of structures is obtained including mesoporous metals<sup>113-116</sup>, metal oxides<sup>117-123</sup> and periodic mesoporous organosili-



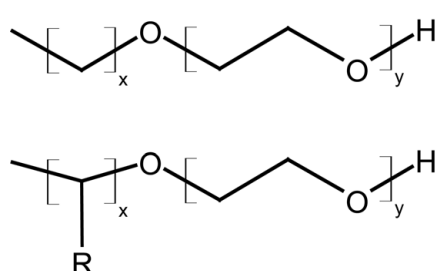
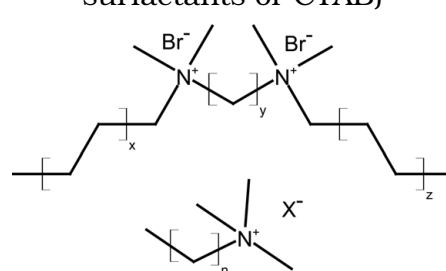
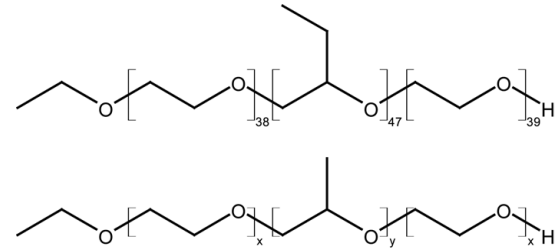


**Figure 2.1:** Two synthetic strategies of mesoporous materials: (A) cooperative self-assembly; (B) “true” liquid-crystal templating process.<sup>103</sup>

cas (PMOs)<sup>124-126,109</sup>. Surfactant-free mesopores, in turn, can template structures by filling them, for example with organic material. After carbonization at about 1000°C and removal of the mesoporous framework, e.g. by dissolution of silica in an aqueous solution containing NaOH and ethanol, highly ordered carbon molecular sieves can be synthesized.<sup>127-130</sup> This so called hard templating procedure is rather time-consuming, as at first a mesoporous structure has to be synthesized which afterwards templates the carbon. Thus recent efforts resulted in the development of a soft templating route via the polymerization of organic oligomers in the presence of surfactant.<sup>131-133</sup>

## 2.2 Synthesis of mesoporous (thin) silicate films

In general mesoporous silicates are obtained by “hydrothermal” synthesis at room temperature or slightly elevated temperatures (rarely above 100°C). In most cases acidic or basic aqueous solutions are used, as in a neutral environment the silica precursor hydrolyzes too slowly. During synthesis the mesoporous material precipitates and can be filtered off. Needless to say that this method is inappropriate for producing thin layers. Therefore several other preparation methods were developed in order to get periodically ordered mesoporous thin silica films (see figure 2.2). Chemical solution deposition methods, like spray, meniscus, spin and dip coating are the most common methods, as

<p>Diblock Copolymers<sup>36,41</sup> (e.g. Tergitol or Brij)</p>  <p><math>12 \leq x \leq 18, 2 \leq y \leq 30, R = H, CH_3</math></p>	<p>Alkyltrimethylammonium salts<sup>33,38</sup> (e.g. gemini surfactants or CTAB)</p>  <p><math>8 \leq x, z \leq 16, 2 \leq y \leq 18, n = 12, 16, X = Br, Cl</math></p>
<p>Triblock Copolymers<sup>37,41</sup> (e.g. Pluronic)</p>  <p><math>5 \leq x \leq 30, 30 \leq y \leq 70</math></p>	<p>Primary amines<sup>35</sup></p> <p>R-NH<sub>2</sub></p> <p><math>C_8 \leq R \leq C_{18}</math></p>

**Table 1:** Common templates for the synthesis of mesoporous materials

Precursor	Resulting mesoporous material
Alkoxysilanes (TEOS, TMOS)	amorphous silicon dioxide
Metal salts, metal-organic complexes or inter-metallic phases	amorphous and even crystalline metal oxides or metals
Bridged alkoxysilanes	Periodic mesoporous organosilicates (PMOs)
organic oligomers	Periodic mesoporous pure carbon frameworks

**Table 2:** Common precursors for the synthesis of mesoporous materials

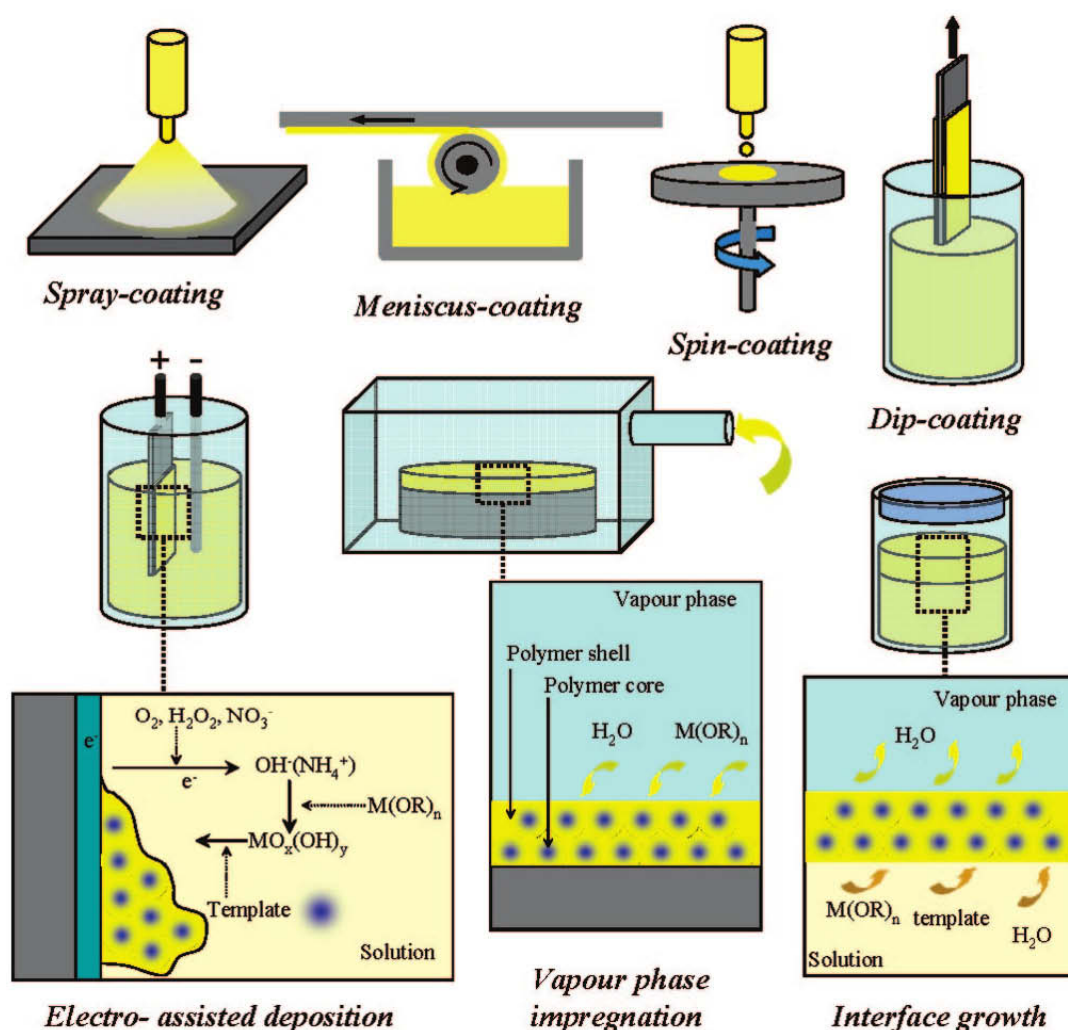
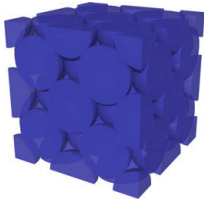
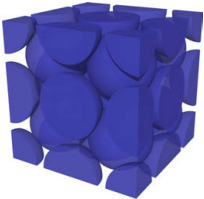
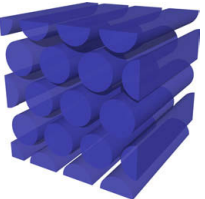
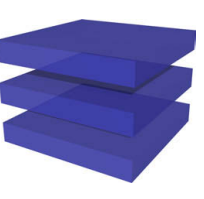
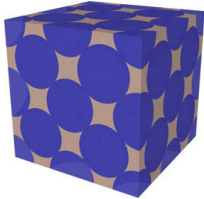
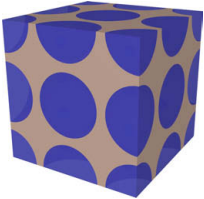
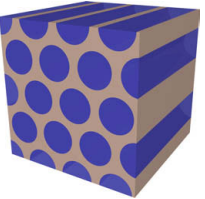
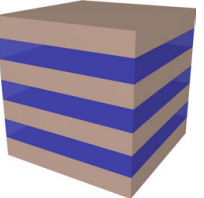
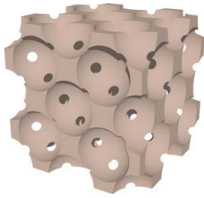
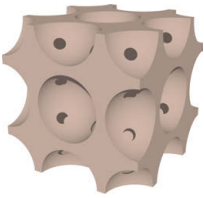
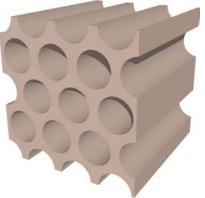


Figure 2.2: Various synthesis techniques for mesoporous thin silica films.<sup>63</sup>

they are cheap and easy to handle, but also because they are compatible with the so-called evaporation-induced self-assembly (EISA) approach, first introduced by Brinker in 1999.<sup>134</sup> Starting point is a homogeneous solution containing silica precursor, surfactant and water in a volatile solvent with a surfactant concentration far below the critical micelle concentration. As the solvent evaporates during synthesis, the surfactant concentration increases and self-assembly of silica-surfactant micelles begins. These micelles then further organize towards liquid crystalline mesophases, resulting in thin mesostructured films after condensation of the precursor. Different mesostructures are formed through variation of the initial alcohol/water/surfactant mole ratio.

	Fm $\bar{3}$ m	Im $\bar{3}$ m	P $_6$ mm	lamellar
liquid crystalline phase				
organic-inorganic mesostructure				
mesoporous structure				

**Table 3:** Examples for common structures of mesoporous materials. The initial liquid crystalline phase of the templating molecules is normally preserved as a negative “imprint” in the solid after template removal. Only lamellar mesophases collapse without template.

Other methods for thin film synthesis, like electro-assisted deposition, vapor phase impregnation or interphase growth, are very interesting for some special applications, but cannot be declared as general synthesis procedures.

### 2.3 Structures of mesoporous materials

Ordered mesoporous materials are made with templating molecules, forming liquid crystalline phases. After template removal the resulting mesostructures represent inverse phases of such liquid crystals. A Fm $\bar{3}$ m mesostructure, for example, derives from a face centered cubic packing of spherical micelles, an Im $\bar{3}$ m mesostructure from a body centered cubic arrangement of such micelles and the two-dimensional (2D) hexagonal mesophase is built up from hexagonally packed micellar rods. Another very common structure is the lamellar mesophase, formed by alternating layers of template and silica. Of course, in this case template removal will destroy the structure (see table 3).

The number of possible structures is even increased if mesoporous layers on flat substrates are formed, depending on the orientation of the unit cell

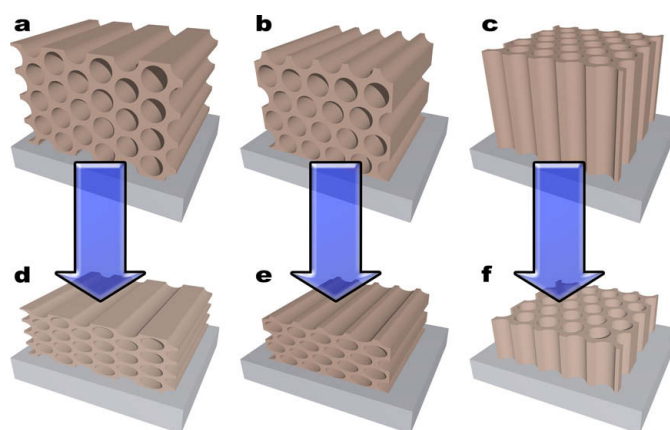


**Figure 2.3: Three possible orientations of a  $P_6mm$  mesostructure coated on a silicon wafer. a** 110 lattice planes parallel to the substrate surface. **b** 100 lattice planes parallel to the substrate surface. **c** Both lattice planes are perpendicular to the substrate surface. **d, e** By shrinkage the  $P_6mm$  structures with pores parallel to the substrate surface transform into  $C_2mm$  structure types. **f** A  $P_6mm$  structure with pores perpendicular to the substrate surface is not much influenced by shrinkage.

relative to the substrate. This is explained in figure 2.3a-c on the basis of the  $P_6mm$  mesophase. Furthermore, film shrinkage after synthesis - only possible in z-direction (otherwise cracks occur) - in most cases includes a decrease in symmetry, which also results in new structure types (see figure 2.3d-f). Phase mixtures are also known, e.g., lamellar with 2D hexagonal<sup>135</sup> and mesoporous materials within the pores of anodic alumina membranes<sup>136,137</sup>.

## 2.4 Characterization methods

### 2.4.1 Electron microscopy

As mentioned above direct imaging of nanostructures is only possible by electron microscopy (EM), scanning tunneling microscopy (STM) or atomic force microscopy (AFM). EM provides in principle two main methods, scanning and transmission electron microscopy (SEM and TEM, respectively). Both methods use focused electron beams for imaging. Detectors within the SEM measure the intensity of back-scattered electrons to create an image, whereas TEM uses the electrons passing through the sample for imaging.

This means that SEM, as well as AFM and STM only provide a detailed image of the sample surface. But TEM is able to reveal the structure inside the sample. For this purpose the sample must be thin enough to let the electrons pass through. Often this is associated with time-consuming sample preparation and

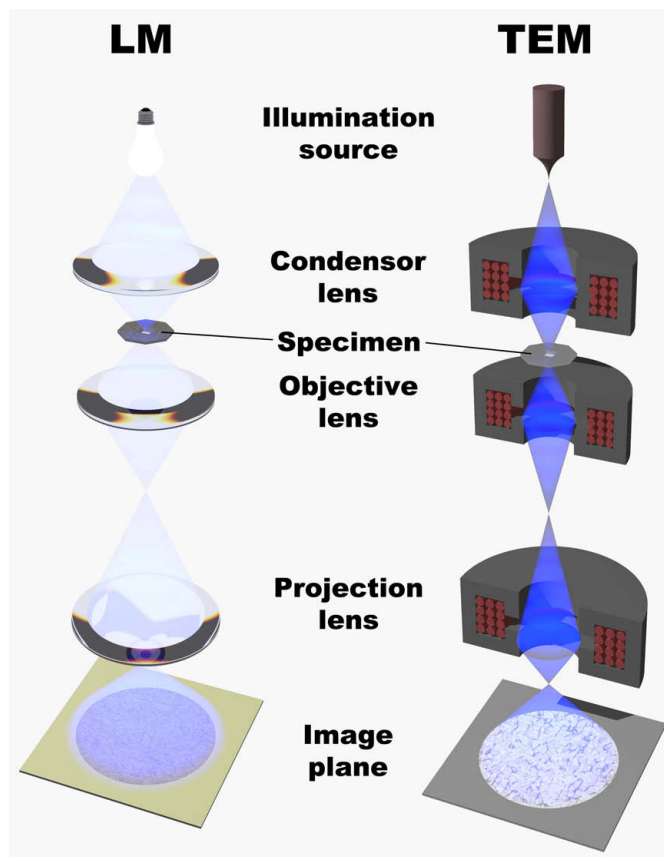


**Figure 2.4: Comparison between light and electron microscopy.** The construction of light microscopes and transmission electron microscopes is basically the same. Instead of glass lenses TEM uses electro-magnetic lenses and reaches much higher magnifications due to the smaller wavelength of the electrons in the beam.

costly machines, e.g. ion mills or microtomes. By contrast, conducting SEM samples don't have to be treated in a special way and non-conducting samples are simply covered by a thin conducting layer, like carbon or gold.

TEM, as well as SEM, use either thermal emission of a tungsten or  $\text{LaB}_6$  cathode or a field emission gun to create the electron beam. In the SEM the electrons are accelerated by tensions between 1 and 30 kV, whereas TEM normally works in the range of 100 to 300 kV. There are also TEMs with acceleration voltages up to 1000 kV. The electron beam is focused by the use of magnetic fields generated by passing a current through a set of windings. These lenses are comparable to convex lenses in optical microscopy. In SEM the size of the focused beam on the sample surface is crucial for high image quality, as the beam is scanning the surface line by line. So a smaller beam increases the



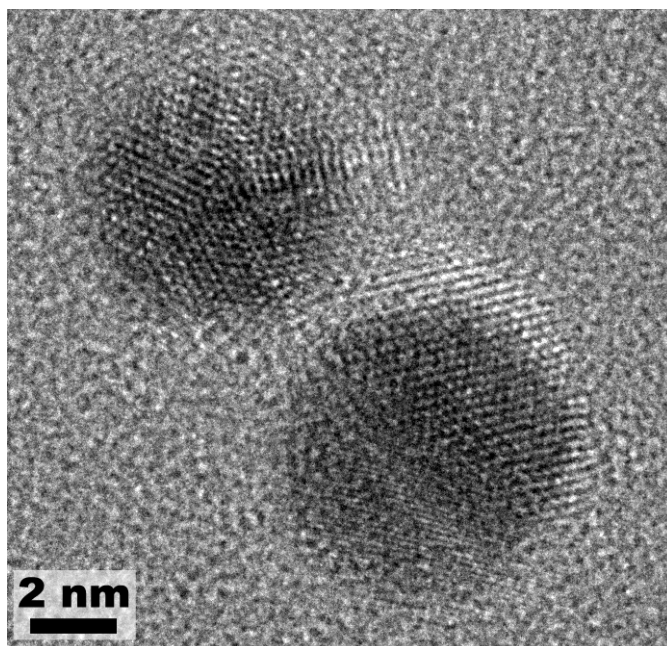


**Figure 2.5: HRTEM image of gold clusters.** If the particle's lattice planes are oriented parallel to the incident electron beam, interference caused by Bragg diffraction appears and creates strongly alternating contrast. The diffraction patterns vary, even within one particle, so that there are also parts only showing contrast caused by electron density fluctuation. Delocalization effects due to lens aberrations and defocus are also visible.

resolution of the microscope.

In conventional TEMs the electrons pass through the sample and an image plate or a CCD beyond the sample is recording the diffracted beam. That is why the electron spot must at least have the size of the sample area one is interested in. Much more crucial for image quality are the spherical and chromatic aberrations of the electro magnetic lenses. With high technical effort these aberrations can be minimized, but electro-magnetic lenses are still not working as well as optical lenses do. So the theoretical resolution of a TEM determined by its acceleration voltage and therefore normally in the range of a few picometers is approximately ten times better than the best resolution achieved in reality. Nevertheless, a resolution of  $0.5 \text{ \AA}$  achieved by the actual state of the art TEMs under ideal conditions is good enough to image single atoms.

One problem of TEM is that contrast is not only caused by different electron densities but also by diffraction of the beam at lattice planes parallel to it, comparable with XRD (see figure 2.5). Thus, the interpretation, especially of

high resolution TEM (HRTEM) images can be difficult and needs a high degree of experience. A combination of both SEM and TEM, the scanning transmission electron microscopy (STEM), overcomes this problem by scanning with a highly focused electron beam through the sample. The variation in beam intensity caused by the actual electron density at each sample position is imaged and diffraction is avoided. Then again the resolution is determined by the size of the electron beam, with the result that good STEM resolutions are only in the Å-range.

### 2.4.2 Electron Tomography

Electron tomography (ET) usually implies retrieving three-dimensional information of an object by the use of several TEM images at different tilt angles. The sample is fixed on a special tomography holder, which is able to rotate the specimen by a specified number of degrees around one or two axes. The TEM images collected at different tilt angles are two-dimensional projections of the object and the entirety of all projections is a so-called tilt series. Depending on the acquisition mode several different possibilities exist how contrast in the projections comes about. In biology “normal” bright-field TEM images are often used, but in materials science, especially in connection with mesoporous materials or nanoscale metal clusters, diffraction contrast occurs and hampers the reconstruction. In those cases STEM is often a better choice and by the use of high angle annular dark field (HAADF) imaging, contrast in the projections is produced due to variations in the atomic number of atoms in the sample (Z-contrast imaging).

The basic steps in ET are projection and backprojection. When light is shining on a semi-transparent cube its projection consists of different gray values representing the intensity loss after passing the cube. Longer pathways cause more absorption and therefore result in a darker gray value (see figure 2.6). Crucial is the exact correlation between absorption and projection intensity. In the easiest case a twofold higher gray value means a twofold higher absorption and therefore a twofold longer pathway through the sample. This direct correlation is preferred in ET.

For a better understanding figure 2.7 depicts the projection and backprojection steps by means of a two-dimensional rastered object. If an imaginary light beam hits this  $8 \times 8$  matrix and is partly absorbed, the projections in x and y direction would look like in figure 2.7a. Each gray value represents a dis-



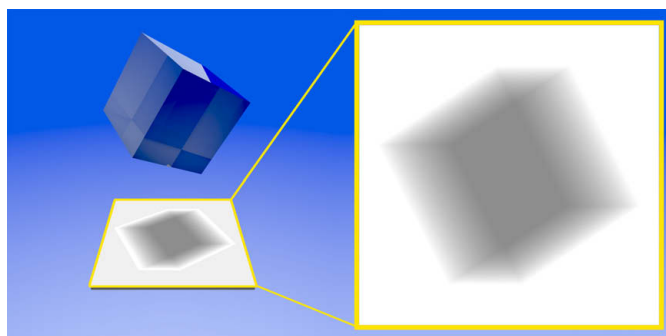


**Figure 2.6: Projection step.** Light shining through a semi transparent object is absorbed according to the path length within the object. Longer pathways absorb more light and hence the projection shows less intensity at this point. This is quite comparable to bright-field TEM measurements. The thicker the sample is the more electrons are absorbed.

tinct path length of 'light' through the object and can therefore be expressed as a number (see figure 2.7b). For a successful reconstruction these one-dimensional projections have to be extended into the second dimension. This is done by equally distributing the intensities of the projection to the matrix along the projection pathway (see figure 2.7c,d). Of course, both procedures can be applied to two-dimensional projections and three-dimensional objects as well.

Averaging over all backprojections is the easiest way for reconstruction and requires a minimum of computational power. To improve the reconstruction quality the projections are often filtered before backprojection and therefore this technique is called filtered back projection (FBP). The method is depicted in figure 2.8. Every filtered projection is smeared back into object space at the angle of the original projection. The superposition of all these volumes results in a three-dimensional image of the original object.

Iterative reconstruction algorithms, however, are more accurate but also computationally more intensive. According to FBP backprojection is applied to calculate a reconstructed volume. The main difference is that instead of the original projections so-called difference projections are used for backprojection. The actual tomographic reconstruction is used to calculate projections along the same pathways the original TEM images are derived from. If the reconstruction would be perfect there would be no difference between the original and the calculated projections. As this is normally not the case, these differences computed by subtracting the original projections from the calculated ones are the difference projections, which are used to get a difference

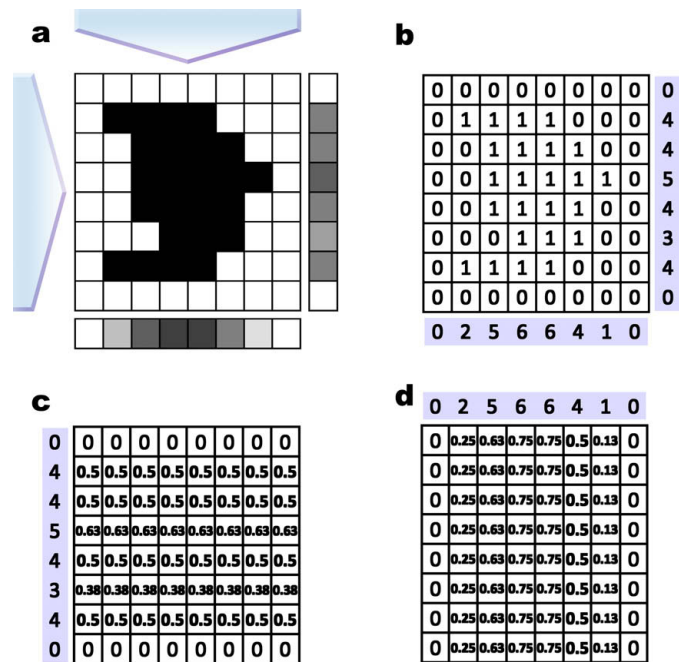


**Figure 2.7: Projection of a  $8 \times 8$  matrix and backprojection of the resulting one dimensional projections.** **a** An imaginary light beam passes through a matrix and is partly absorbed by the black shape. The resulting projections consist of distinct gray values according to the path length of the 'light' within the shape. **b** The gray values can be linked to numbers representing the sum of black squares along the projections pathway. **c, d** The one-dimensional information is extended into the second dimension by an equal distribution of the intensities along the projection pathway. **c** is representing the backprojection in x, **d** the backprojection in y direction.

volume by backprojection. The actual reconstruction combined with the difference volume is the new reconstructed volume from which the next projection(s) are calculated. Thus, step by step the differences are minimized and the reconstruction gets more accurate.

Depending on when the reconstructed volume is updated there are several different algorithms.<sup>138</sup> Using ART (algebraic reconstruction technique) this is done after the backprojection of every single point in the projections. ART is relatively fast for iterative methods, as the difference projections converge quickly to zero, but it often results in very noisy reconstructions. Slower converging, but less susceptible to salt and pepper noise is SART (simultaneous algebraic reconstruction technique). Here a new reconstruction is only calculated after the backprojection of a whole difference projection. Finally, there is the possibility to update the reconstructed volume only after backprojection

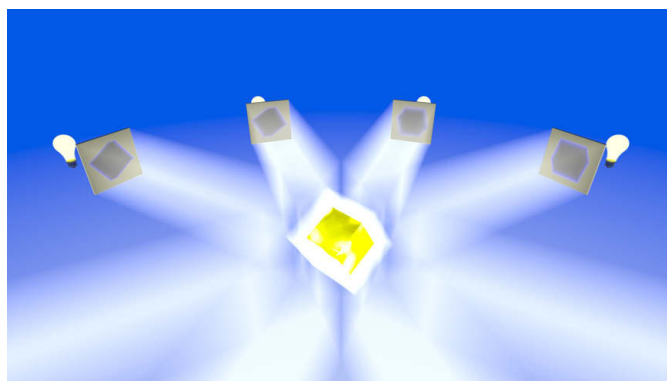


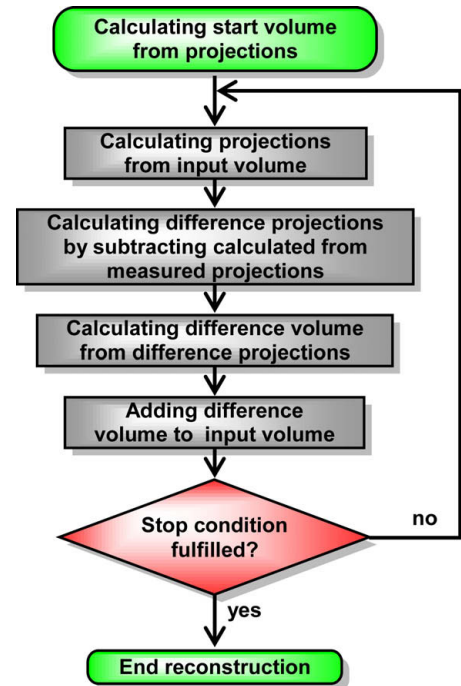
**Figure 2.8: Schematic representation of the backprojection procedure.** Every projection is smeared back into object space along the pathway it was originally taken. Superimposition of all these volumes reveals a three-dimensional image of the original sample.

of all difference projections. This method called SIRT (simultaneous iterative reconstruction technique) is definitely more time-consuming than the previous techniques, but provides very smooth reconstructions with minimum noise.

Beside FBP SIRT is the most common algorithm for reconstruction of biological samples. Nowadays, SIRT algorithms are executable even on normal desktop PCs in an acceptable period of time. As SIRT is also the basis for the discrete algorithm used in this work, it will be discussed in more detail (see also figure 2.9). Starting point is a reconstructed volume generated by backprojection of the whole tilt series. During one iteration step first all difference projections are calculated from the input volume and the original projections. From these projections the difference volume is computed and added to the actual reconstruction. The combined volumes then represent the new input volume and the next iteration step starts over again. The algorithm ends if a previously defined stop condition is fulfilled, e.g. a distinct number of iteration steps is reached.

In general the reconstruction quality increases with the number of projections (see figure 2.10), but this is equivalent to a higher electron dose, which can cause beam damage. That is the reason why in many cases reconstructions of beam sensitive samples are either not possible or have only very poor quality. Another limiting factor is the tilt range. In practice, at higher tilt angles the sample holder can hit the objective lens pole pieces, because there is only limited space between them. By tilting also the electron's pathway through the sample is lengthened, bringing about a drastically decreased image quality. In

**Figure 2.9: SIRT flow chart.** By the use of the original projections a starting volume is computed. From this input volume projections are calculated along the same pathways the original projections were imaged. By subtracting the original projections from the corresponding calculated ones so-called difference projections are obtained. These are used to compute a difference volume by backprojection with which the starting volume is updated. The updated reconstruction represents the new input volume and the procedure starts over again until a previously defined stop condition is fulfilled, e.g. a distinct number of iterations is reached.



addition, the copper grid that is used for many samples can block the beam at higher tilt angles. Only in special cases a full  $180^\circ$  rotation of the sample is possible<sup>139</sup>. If not, the so-called “missing wedge” problem causes an elongation of objects perpendicular to the tilt axis, resulting in an anisotropic spatial resolution of the reconstruction.<sup>140</sup>

Even if a high quality reconstruction could be obtained, the main problem of SIRT remains - segmentation. A SIRT reconstructed volume consists of thousands or millions of different gray values, but not each gray value is representing a single material or cell component. Such objects are always built up by a range of gray values having a minimum and maximum. As due to the SIRT algorithm the transition from one object to the next is very smooth, the intensity ranges of two different objects can overlap. Therefore, it is normally not possible to segment a reconstruction by simple joining distinct ranges of gray values. Also edge detection algorithms are not robust enough to do a complete automated segmentation. In any case, human intervention is necessary, which makes segmentation not only laborious and time-consuming, but also subjective, thus depending on the operator.

An approach to overcome these drawbacks is DART (discrete algebraic reconstruction technique), a new algorithm for discrete tomography (DT). DT allows the use of additional information for reconstruction. In the case of DART this

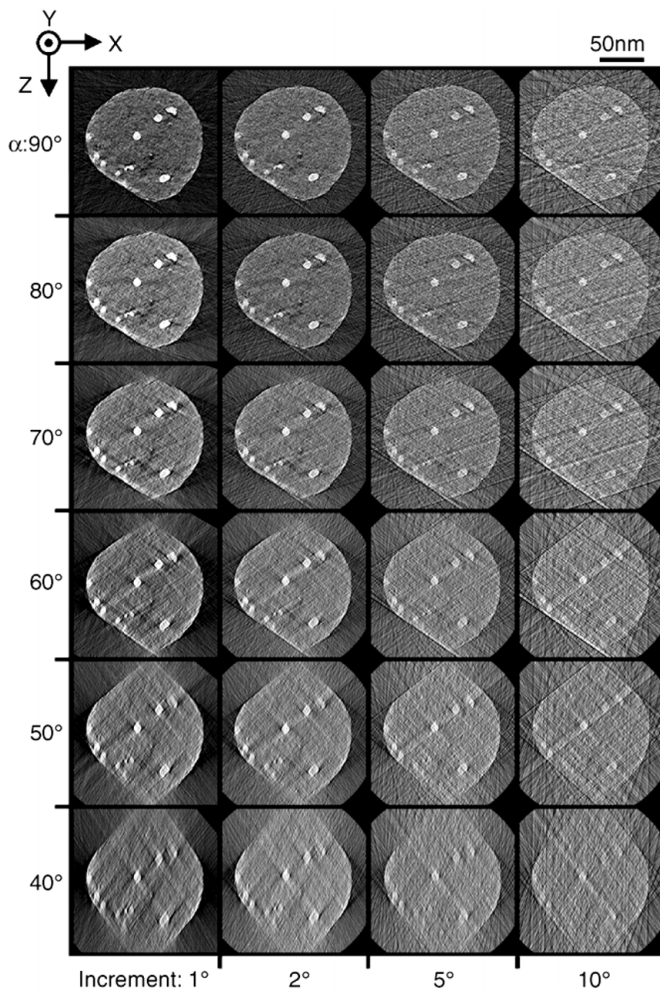
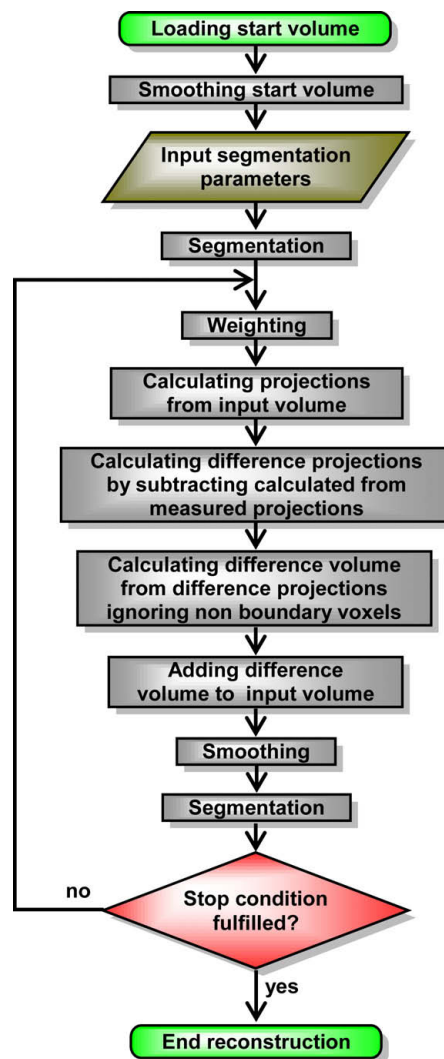


**Figure 2.10: The reconstruction quality is influenced by the number of projections and the tilt range.**<sup>139</sup> Cut through several SIRT reconstructions of a rod shaped specimen at the same region. The sample is a zirconia/polymer nanocomposite and its reconstructions were calculated with different tilt ranges and various numbers of projections. From top to bottom the tilt range decreases from  $\pm 90^\circ$  to  $\pm 40^\circ$ . From left to right the increment is increased, thus the number of projections is reduced. The top left image represents a nearly perfect reconstruction using about 180 projections. The zirconia particles are clearly distinguishable and the sample shape does not show any artifacts. By decreasing the tilt range elongation in z-direction occurs (missing wedge problem) and a reduced number of projections results in reconstructions with less contrast and ray-like artifacts.

**Figure 2.11: DART flow chart.** As starting volume a SIRT reconstruction is chosen. According to data given in advance the volume is segmented so that only a distinct number of gray values remains. In a weighting step boundary voxels are identified. From the segmented volume projections are calculated along the same pathways the original projections were imaged. By subtracting the original projections from the calculated ones so-called difference projections are obtained. These are used to compute a difference volume, but in contrast to a normal backprojection procedure the projection intensities are only distributed to boundary voxels. After the reconstruction is updated with the difference volume, it represents the new input volume and the procedure starts over again until a previously defined stop condition is fulfilled, e.g. a distinct number of iterations is reached.



is the number and the gray values of the different materials the sample consists of. Indeed, obtaining this information from biological systems is nearly impossible, but in combination with STEM - HAADF (scanning transmission electron microscopy in high angle annular dark field mode) DART is an excellent tool for materials scientists. In HAADF mode the collected intensity is approximately proportional to  $Z^2$ , which means that a gold cluster would show an intensity 2.8 times higher than a silver cluster of the same size and cause a 38.9 fold higher intensity than a comparable titanium dioxide nanoparticle.

DART can be considered as a modification of SIRT on which it is based on. As starting volume a SIRT reconstruction is used, which is segmented according to data given in advance. During segmentation every pixel is assigned to one of

the available materials by range selection. Afterwards the actual DART iteration begins by weighting the volume. In fact every voxel (the three-dimensional counterpart of a pixel) completely surrounded by voxels with the same value - therefore the same material - is defined as non-boundary voxel and will be left unmodified in the following projection/backprojection step. From the input volume projections are calculated at the same angles as the original STEM images. By subtracting an original projection from a calculated one the so-called difference projection is obtained. With these difference projections a new volume is reconstructed by backprojection distributing the projection intensities only to boundary voxels. After combining the difference volume with the actual reconstruction this volume becomes the new input volume and the iteration step starts over again as long as a given number of iterations is reached or another stop condition is fulfilled.

Using DART the number of projections can be reduced drastically and the reconstruction quality in comparison to SIRT is strongly increased with the same number of projections, respectively. "Missing wedge" artifacts are reduced and segmentation is accomplished in an automated manner. Only, the sample has to contain a known number of different materials with diffraction capabilities for electrons clearly distinguishable in the projection. Therefore DART is normally not applicable on biological systems, but it is an ideal method to characterize samples in materials science.

However, where can we obtain the gray values for each material? The most accurate, but also elaborate way is the determination by reference experiments. As this is not always possible, the gray values can also be estimated from the projections, the SIRT reconstruction and its histogram, respectively.

### **2.4.3 Single molecule fluorescence microscopy**

Conventional microscopy often suffers from low contrast, so that the objects of interest are poorly distinguishable from the background. One possibility to overcome this problem is fluorescence microscopy. By attaching fluorescing dye molecules to specific parts of the specimen, these objects can be illuminated and therefore stand out from the non-fluorescent background. In addition, with special methods like STED microscopy<sup>141,142</sup> it is even possible to achieve resolution far below the optical diffraction limit defined by Abbe - at present approximately down to 5 nm.<sup>143</sup> More information than with conventional fluorescence techniques is also gained by the use of single molecule



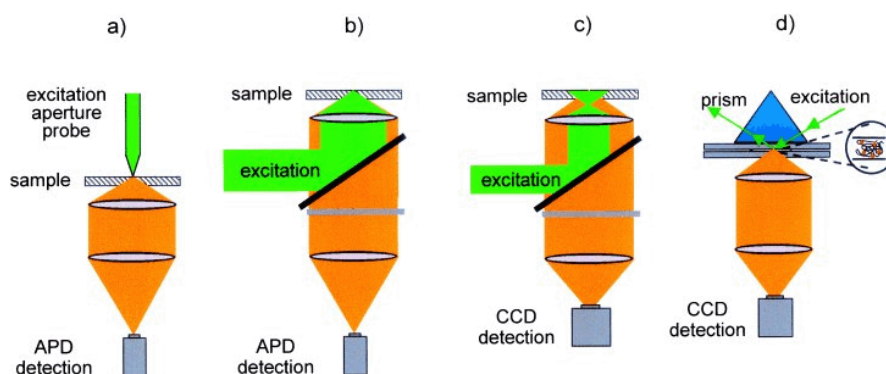


**Figure 2.12: Four experimental approaches to detect single molecules.**<sup>159</sup> **a** Near-field microscopy, **b** confocal microscopy, **c** wide-field microscopy and **d** total internal reflection (dark-field) microscopy.

fluorescence microscopy (SMM), as it provides the real distribution of a certain measurement parameter instead of the average value obtained by the common ensemble measurements. Even if Abbe's law has to be respected, it is possible to localize single dye molecules with a positioning accuracy of less than 3 nm.<sup>144</sup> SMM has become a widely used method<sup>145-147</sup> in various fields, ranging from biology<sup>148-153</sup> to materials science.<sup>135,154-158</sup> The requirements of severe background reduction, high detection efficiency and spatially selective imaging necessary for single molecule detection are achieved by several microscopic techniques as shown in figure 2.12.

By single-molecule tracking (SMT), which means taking image series and tracking the successive positions of an individual molecule, it is possible to resolve molecular trajectories and learn about the diffusional behavior, for example within a porous host.<sup>160-165</sup> For this purpose fast imaging techniques are needed and therefore wide-field microscopy is often the method of choice. Unlike the first experiments, today such measurements are carried out at room temperature, but still ultra-clean solvents, extremely sensitive CCD cameras and highly stable fluorescent dyes are needed, so that SMT can by no means be seen as a standard technique for diffusion studies. This may also be attributed to the fact that data evaluation is time-consuming and algorithms automating the work are often not stable, due to noisy data or crossing molecules.

To obtain a trajectory of an individual molecule its position in each frame of the image series has to be determined by fitting a two-dimensional gaussian



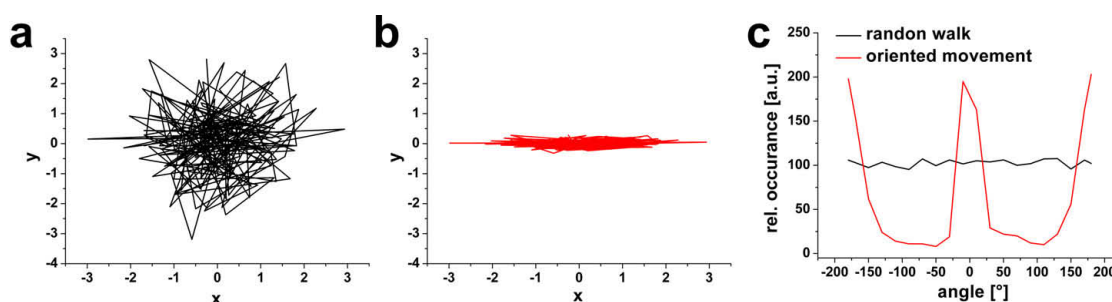


**Figure 2.13: Different types of trajectories in two dimensions.** **a** Random walk, unstructured movement. **b** Oriented, structured movement. **c** Histogram of angles between successive steps. An uniform distribution is characteristic for random walk, whereas a structured movement has maxima at  $0^\circ$  and  $\pm 180^\circ$ .

function to the fluorescence spot:

$$f(x, y, A, w) = A e^{-\left(\frac{x-x_0}{w}\right)^2} e^{-\left(\frac{y-y_0}{w}\right)^2}$$

$A$  and  $w$  are the amplitude and the width of the gaussian curve, respectively. All positions together represent the diffusion trajectory of the molecule. The movement in two dimensions can be either random-walk (2D) or structured (1D), as sketched in figure 2.13. But one should keep in mind that the diffusion is sampled at discrete points in time and space. The connecting lines are just a method of visualizing the trajectories; they do not represent the molecules' exact path. By collecting several tens or hundreds of trajectories of one sample, it is also possible to extract the diffusion coefficient and to identify sub-populations.

#### 2.4.4 1D X-ray diffraction

Although mesoporous silica is normally a non-crystalline material X-rays diffracted by such periodic structures can interfere and cause diffraction patterns similar to crystals. In this case the pore walls are acting as lattice planes (see figure 2.14a). A simple mathematical correlation between wavelength  $\lambda$ , d-spacing  $d$  and diffraction angle  $\theta$  is given if the angle of incidence equals the angle of reflection (Bragg's law, see also figure 2.14b):

$$\sin\theta = \frac{n \cdot \lambda}{2 \cdot d}$$

Figure 2.14c shows a typical powder diffractogram of SBA-15 bulk material. As the individual silica particles are randomly oriented, all lattice planes are

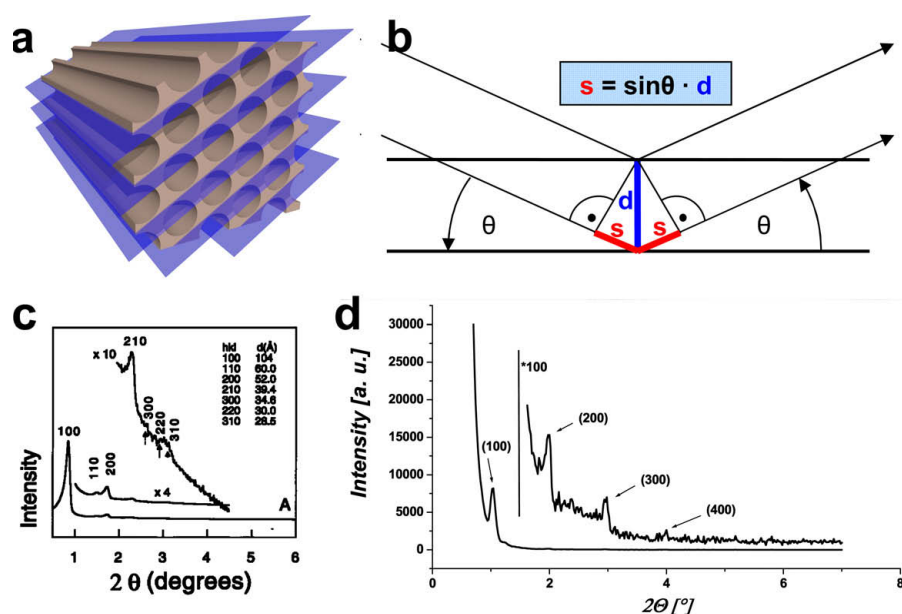


**Figure 2.14: X-ray diffraction caused by mesoporous material.** **a** Lattice planes of a  $P_6mm$  mesophase (e.g. SBA-15 or MCM-41). **b** Bragg's law. **c** Typical 1D-XRD of hexagonally ordered mesoporous Bulk-SBA-15.<sup>39</sup> **d** Typical 1D-XRD of a hexagonally ordered mesoporous SBA-15 film.

visible. In comparison, figure 2.14d depicts the XRD pattern for a thin mesoporous SBA-15 layer on top of a silicon wafer, also measured in standard Bragg-Brentano geometry. Due to the alignment of the silica rods relative to the substrate surface, only the (h00)-reflections are visible.<sup>166</sup> Their spacing of about  $1^\circ$  is quite comparable to the bulk material and is caused by a lattice plane distance of 8 to 10 nm (Cu  $K_\alpha$  irradiation). No reflection at all would occur if the channels were oriented perpendicular to the substrate and only if the 100 face is parallel to the surface a pattern similar to fig 2.14d is obtained (see supplementary figure 9.1).

#### 2.4.5 X-ray reflection

XRD diffraction in  $\theta/2\theta$  geometry (standard powder diffraction) is using the specular reflection of X-rays at interfaces. These interfaces are caused by layers with different electron densities, similar to two different refraction indices in optics. If the incident angle  $\theta$  is greater than  $\theta_c$  (critical angle of total reflection, e.g.  $\theta_c(\text{Si}) \approx 0.223^\circ$ ) and thin ( $< 100$  nm) films are investigated, the X-rays will penetrate the sample and can be reflected on the upper and the lower side. In contrast to optical spectroscopy methods, like Raman or IR,

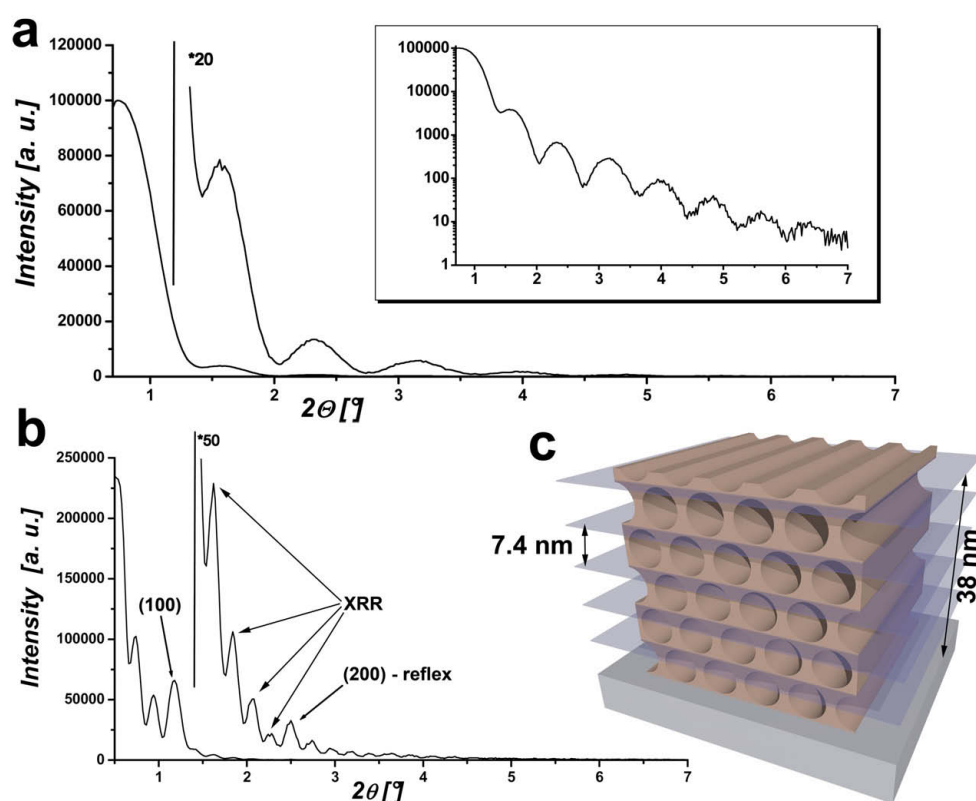


**Figure 2.15:** **a** XRD of a thin silica layer ( $\sim 10$  nm). The periodicity is clearly visible in a semi-logarithmic plot (inset). **b** XRD of a  $P_6mm$  mesophase. The thickness derived from XRR is about 38 nm, the (h00) d-spacing approximately 7.4 nm. **c** This corresponds to five layers of silica rods lying upon another.

these reflections do not result in frequency-dependent interferences. In fact, as the geometry is equivalent to reflection at lattice planes (figure 2.14b) the interferences cause periodic reflections quite similar to a damped oscillation (see figure 2.15a). The period can be used to calculate the film thickness via Bragg's law and the damping provides information about surface roughness. The accuracy of thickness measurements using XRR is strongly dependent on the angular range the reflections are obtained and their periodic spacing. A pattern with many reflections over a wide range (up to  $5^\circ 2\theta$ ) can provide accuracies below 1 Å.

XRD patterns of mesoporous thin films often show a superposition of (h00)-reflections and XRR-reflections. The exponential decay of XRR-reflections, visible in the inset of figure 2.15a, is then disturbed by higher reflections caused by the (h00) lattice planes. Figure 2.15b shows the XRD pattern of a  $P_6mm$  mesophase. The thickness derived from XRR is about 38 nm, the (h00) d-

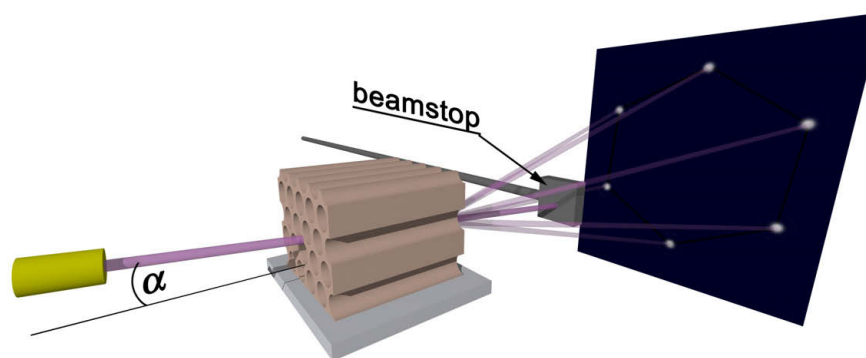


**Figure 2.16: Idealized 2D-GISAXS of a  $P_6mm$  mesophase.** The angle of incident  $\alpha$  is in the range of the critical angle  $\theta_c$ . The small angle results in a very surface sensitive characterization method, well suited for studying nanostructured films. In the case of a  $P_6mm$  mesophase the pattern in reciprocal space itself is again hexagonal.

spacing approximately 7.4 nm. This corresponds to five layers of silica rods lying upon another (see figure 2.15b).

#### 2.4.6 2D X-ray diffraction

Due to the fact that only lattice planes parallel to the substrate are detectable, the sole use of 1D-XRD data is not sufficient for structure determination of mesoporous layers. A reliable differentiation between thin mesophases on flat substrates is given by using for example two-dimensional grazing incidence small angle X-ray scattering (2D-GISAXS), where the incident angle  $\alpha$  is in the range of  $\theta_c$  (see figure 2.16). Because of higher brilliance and intensity, 2D-GISAXS experiments are normally carried out with synchrotron irradiation. In this case, even micrometer-sized samples can be measured, and motorized stages ensure an exact sample alignment.<sup>167</sup> Due to the small angle of incidence, the penetration depth of the X-ray beam can be limited to several nanometers. Therefore, GISAXS is a surface sensitive method, not only used for structure characterization of mesoporous thin films<sup>48,168-178</sup> but also for studying thin films of block co-polymers,<sup>179</sup> or visualizing nanocrystal growth in real-time<sup>180</sup> or investigating polymer/nanocrystal mixtures<sup>181</sup>.

#### 2.4.7 Ellipsometry

Ellipsometry measures a change in polarization as light reflects or transmits from a sample. The polarization change is represented as an amplitude ratio,  $\Psi$ , and the phase difference,  $\Delta$ . The measured response depends on optical

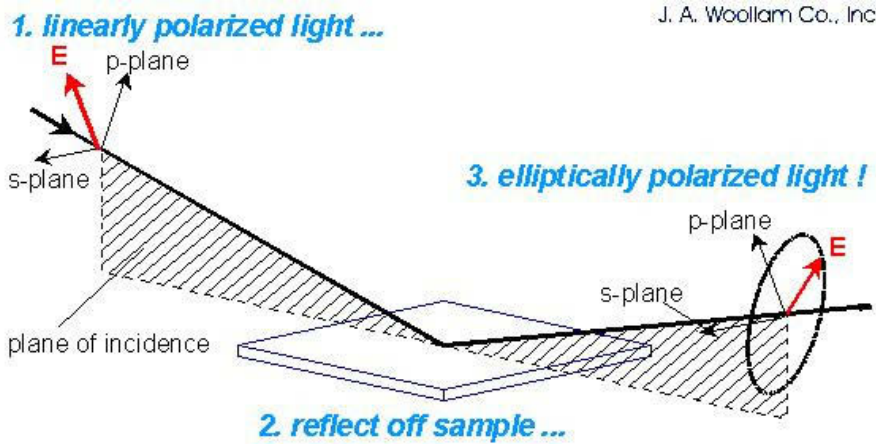


**Figure 2.17: Typical ellipsometry configuration.**<sup>182</sup> The linearly polarized light is reflected from the sample surface and the polarization change is measured to determine the sample response.

properties and thickness of individual materials. Thus, ellipsometry is primarily used to determine film thickness and optical constants. However, it is also applied to characterize composition, crystallinity, roughness, doping concentration, and other materials properties associated with a change in optical response.

The incident light is linearly polarized and can be considered as a superposition of two orthogonal light waves, the so-called p- and s-components. Damping and phase shift upon reflection/transmission is normally not the same for the two components and therefore the measured output polarization is elliptical (see figure 2.17).

The new amplitudes normalized to their initial values, are denoted by  $r_s$  and  $r_p$ , respectively.  $\Psi$  and  $\Delta$  are calculated from the reflectance ratio,  $\rho$  (a complex quantity), which is the ratio of  $r_p$  over  $r_s$ , the values measured by ellipsometry:

$$\rho = \frac{r_p}{r_s} = \tan(\Psi)e^{i\Delta}$$

Since ellipsometry is not measuring absolute data, but the ratio (or difference) of two values, it is very accurate, robust, and reproducible. For example, reference beam or standard sample are not necessary and it is not very sensitive to fluctuations and scatter. Ellipsometry is an indirect method, so in general the measured  $\Psi$  and  $\Delta$  values cannot be converted directly into the optical constants of the sample. For data analysis normally a layer model is established, which considers the optical constants (refractive index or dielectric function

tensor) and thickness parameters of all individual layers of the sample including the correct layer sequence. An iterative procedure is applied to calculate  $\Psi$  and  $\Delta$  values using the Fresnel equations. The optical constants and thickness parameters of the sample are obtained from those calculated  $\Psi$  and  $\Delta$  values that match the experimental data best.

#### 2.4.8 Infrared and Raman spectroscopy

Vibrational transitions of molecules are induced by energies in the range of infrared (IR) light. The wavenumber of the absorbed photon is given by following equation:

$$\tilde{\nu} = \frac{\omega_{osc}}{c} = \frac{1}{2\pi c} \sqrt{\frac{k}{\mu}}$$

$k$  is the force constant for the bond and  $\mu$  is the so-called reduced mass. In the case of a two atomic model  $\mu$  is determined as

$$\mu = \frac{m_1 m_2}{m_1 + m_2}$$

As one can deduce from the first equation, stronger bonds and lower reduced masses will increase the vibrational energy.

Normal IR spectra are measured from  $400 \text{ cm}^{-1}$  to  $4000 \text{ cm}^{-1}$  in transmission or reflection. Today's state of the art is Fourier Transform Infrared (FT-IR) spectroscopy. The whole spectrum is measured at the same time and by Fourier transformation the intensity at each wavelength is calculated. These data are compared to a reference, e.g. KBr (shows nearly no IR bands), to extract the absorption bands of the sample. Roughly speaking, single C-C or similar bonds can be observed up to  $1500 \text{ cm}^{-1}$  and then double bonds occur up to about  $1800 \text{ cm}^{-1}$ . From  $2100 \text{ cm}^{-1}$  to  $2300 \text{ cm}^{-1}$  triple bonds are measured, from  $2800 \text{ cm}^{-1}$  to  $3200 \text{ cm}^{-1}$  the C-H stretching vibrations show up and at higher wave numbers, for example O-H or N-H vibrations are detected.

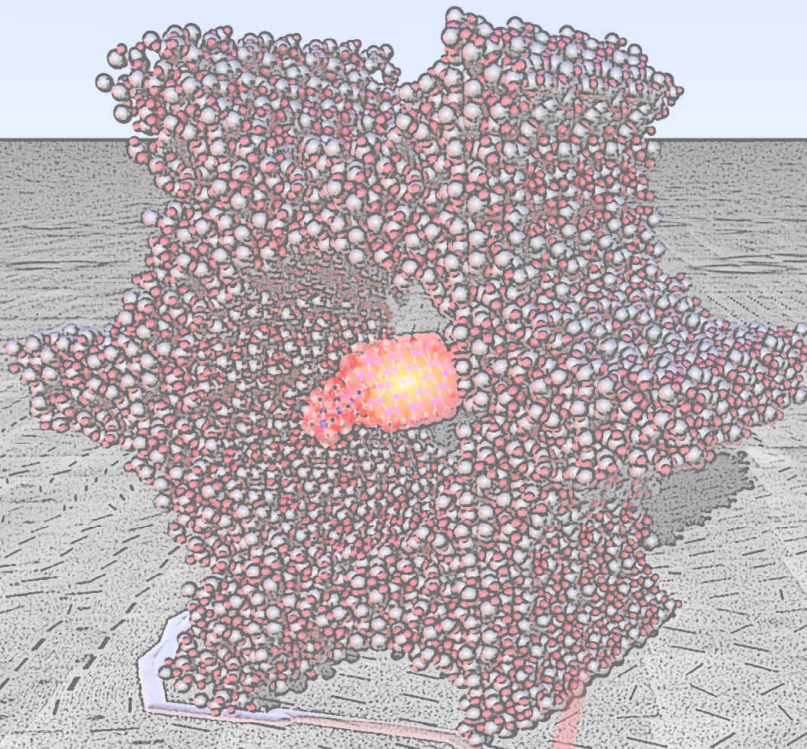
If a vibrational transition attended by a change of the dipole moment, than it is IR active and the corresponding band is visible in the IR spectra. A complementary method to IR, detecting IR-inactive vibrations, is Raman spectroscopy. This technique uses the inelastic scattering of light. When a very intense monochromatic light source irradiates a sample, light is scattered. Most photons are of the same wavelength as the irradiating source, however, some photons have changed their frequency. The frequency change is based on en-

ergy transfer between light and sample, including a vibrational transition. If the molecule is excited to a higher vibrational state, light with lower energy is emitted (Stokes shift). If the molecule is already in a higher excited state, than it can relax and light with higher energy is emitted (Anti-Stokes shift).





# 3



INTRODUCTION

**EXPERIMENTAL METHODS**

RESULTS AND DISCUSSION

CONCLUSION

APPENDIX



## 3 Experimental methods

### 3.1 Starting materials

**Chemicals:** Tetra ethyl orthosilicate (TEOS, Fluka, >98%), (3-Chloropropyl)-triethoxysilane (Cl-TEOS, Aldrich, 95%), 1-ethyl-3-(3-dimethylaminopropyl) carbodiimide (EDC, Fluka, 97%), sodium azide (Fluka, 99%), 4-pentynoic acid (Fluka, 97%), 2-(N-morpholino)ethanesulfonic acid (MES, Sigma), L-Ascorbic acid (Vitamin C, Sigma), Pluronic F-127 (BASF), Brij 56 (Sigma), CuSO<sub>4</sub> (Sigma-Aldrich), gold colloid solution (diameter 5 nm, concentration corresponding to ~0.01% HAuCl<sub>4</sub>; Sigma-Aldrich), trypsin from bovine pancreas (Sigma, lyophilized, essentially salt-free, TPKC treated), Hydrochloric acid standard solution (1M, Fluka) were purchased from Sigma-Aldrich or ABCR. Doubly distilled water from a Millipore system (Milli-Q Academic A10) was used for all synthesis and purification steps. All solvents and buffer contents were purchased from Sigma-Aldrich. All chemicals were used as received without any further purification. Normally, absolute ethanol was used for the synthesis of mesoporous films. Only if fluorescence measurements were performed spectroscopic ethanol was used.

**Film substrates:** The substrate is chosen depending on the analytics. For X-ray diffraction measurements silicon wafers, broken into pieces of about 2.5 cm × 1.8 cm, were found to give the best results, because of their extremely even surface. For fluorescence microscopy, of course, transparent substrates are needed and therefore thin glass slides, sized approximately 2 cm × 2 cm and 200 μm thick, are used. Transmission electron microscopy needs extremely thin substrates for minimal electron absorption. Normally several nanometer thick carbon films on round copper grids (3.05 mm in diameter) are used. But their hydrophobicity and bumpiness made film synthesis impossible. Hence, special Si<sub>3</sub>N<sub>4</sub> membranes (PLANO, Wetzlar) 30 nm in thickness supported by a small silicon wafer with a 500 μm × 500 μm window were used (figure 3.1). Si<sub>3</sub>N<sub>4</sub> membranes are nearly as hydrophobic as SiO<sub>2</sub> membranes, but stable enough to get around an additional support, like a copper grid. Therefore, it is almost as flat as a silicon wafer.

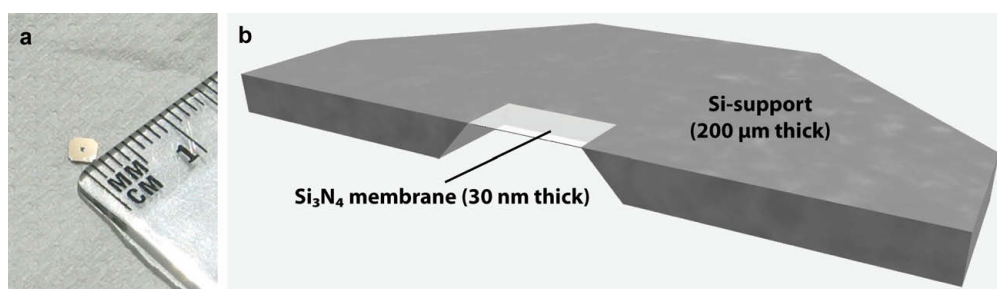


**Figure 3.1:** **a** Photo of a Si<sub>3</sub>N<sub>4</sub> membrane with silicon support. **b** Cross-sectional view (Diagram).

### 3.2 Instruments

**Transmission electron microscopy:** Bright-field TEM images, used for mapping in section 4, were obtained with a JEOL 2011 transmission electron microscope operated at 200 kV by using the software-controlled mapping function of the charge-coupled device camera (model TVIPS F114).

Tilt series (TEM and STEM) for electron tomography (section 7) were obtained with a FEI Titan 80-300 microscope.

**Scanning electron microscopy:** For SEM images a JEOL JSM-6500F scanning electron microscope was used.

**Widefield microscopy and Single Particle Tracking:** The optical microscopy in section 4 including data evaluation and single particle tracking was done by Johanna Kirstein from the group of Prof. Bräuchle. Fluorescence microscopy images were recorded with a wide-field setup as described in more detail elsewhere.<sup>135,183</sup> The wide-field microscopy setup was based on an Eclipse TE200 (Nikon) epifluorescence microscope with a high-numerical-aperture (NA) oil-immersion objective (Nikon Plan Apo 100×/1.40 NA oil). The fluorescent dye molecules were excited at 633 nm with a HeNe gas laser (75 mW max. at 632.8 nm; Coherent) with an intensity of about 0.3 kW cm<sup>-2</sup>, and their fluorescence was detected with a back-illuminated EM-CCD camera in frame transfer mode (iXon DV897, 512 pixels × 512 pixels; Andor). Incident laser light was blocked by a dichroic mirror (640 nm cutoff; AHF) and a bandpass filter (730 nm/140 nm; AHF). Additional lenses (f = 150 mm, f = 200 mm, achromat; Thorlabs) in the detection pathway give an overall magnification of ×133. This means that the side of one square pixel on the camera chip (16 μm) should represent 120 nm on the sample. By using the USAF test target (1951 Chromium

positive; Melles Griot) this value was experimentally determined to 122 nm, which agrees well with the theoretical value.

In section 6 a Ti-U epifluorescence microscope (Nikon) with a high-numerical-aperture (NA) oil-immersion objective (Nikon Plan CFI PLANAPOCHROMAT VC 100 $\times$ /1.40 NA oil) was used. The fluorescent dye molecules were excited by a metal halide lamp (C-HGFI HG INTENSILIGHT; Nikon) and their fluorescence was detected with a back-illuminated EM-CCD camera in frame transfer mode (iXon DV897, 512 pixels  $\times$  512 pixels; Andor). Incident and emitted light passed a filter cube (Nikon EPI-FL FILTER BLOCK CY5: dichroic mirror 660 nm cutoff, excitation bandpass filter 620 nm/60 nm and emission bandpass filter 700 nm/75 nm). By using the USAF test target (1951 Chromium positive; Melles Griot) one pixel was experimentally determined to correspond to 154.5 nm.

**1D X-Ray Diffraction/Reflection:** 1D-XRD/XRR patterns were obtained in a Bragg-Brentano geometry using an XDS 2000 diffractometer (Scintag) and the Cu K $_{\alpha}$  wavelength at 0.15405 nm. Mesoporous films were measured from 0.5 $^{\circ}$  up to 7 $^{\circ}$  2 $\theta$  with a step size of 0.01 $^{\circ}$  2 $\theta$  and a scanning rate of 1 step per second.

**2D Grazing-Incidence Small-Angle X-ray Scattering:** 2D-GISAXS studies were carried out at the Hamburger Synchrotronstrahlungslabor, HASYLAB, in Hamburg (Germany) and at the ELETTRA in Trieste (Italy).

**Ellipsometry:** The ellipsometry measurements were obtained with a Woolam ESM-300.

**Infrared spectroscopy:** Infrared spectra of films on silicon wafers were measured with a Bruker IFS 66v/S FTIR spectrometer, powder IR spectra with a Bruker Equinox 55 DRIFT spectrometer.

**Fluorescence measurements:** Fluorescence spectroscopy was performed using a PTI fluorescence spectrometer with a double monochromator on the excitation side.

### 3.3 Synthesis of mesoporous films used in section 4

#### 3.3.1 Pre-mixed stock solutions

In order to simplify the synthesis several stock solutions were prepared. Small amounts of these solutions were mixed up with TEOS to give the actual synthesis solution, which could not be stored longer than one or two days because of condensation of the TEOS. By contrast, the stock solutions could be stored for several months.

**Hydrolyzation solution** 42 g H<sub>2</sub>O were mixed with 6.12 g 1 M hydrochloric acid and 79 g ethanol.

**Template solution** As the structure of the mesoporous materials highly depends on the silica to template ratio, different template solutions were used. Table 4 gives the amount of Brij 56 diluted in 12.5 g ethanol for each solution and the corresponding structures that were achieved with it.

Amount Brij 56 in mg	250	600	906	2000
Resulting structure	cubic	2D-hexagonal	mixture of 2D-hexagonal and lamellar	lamellar

**Table 4:** Composition of used template solutions

#### 3.3.2 General synthesis

First, 100  $\mu$ l of TEOS were mixed with 645  $\mu$ l of the hydrolyzation solution in a 1.5 ml poly propylene microcentrifuge tube with screw cap and heated at 60 °C for 1 h to accomplish acid-catalyzed hydrolysis and condensation of the silica precursor. After cooling to room temperature this solution was mixed with 735  $\mu$ l of one of the template solutions. Parts of this parent solution were diluted with water or ethanol and, if necessary, gold colloids or poly styrene beads were added. This solution was immediately spin-coated on the substrate at 3000 rpm at various humidities resulting in mesoporous films with thicknesses from approximately 30 nm up to several hundred nm. The humidity was adjusted by a gas flow (dry air or nitrogen), which was divided into two streams. One stream was humidified by passing through a water-filled

wash bottle, the other one remained dry. Before flushing the sample chamber of the spin-coater both gas flows were recombined. This procedure ensured a constant gas flow within the spin-coater, but offered at the same time humidity control only by varying the amount of gas passing the water filled wash bottle. The resulting films were analyzed as synthesized, thus no further sample preparation is needed.

## **3.4 Synthesis of enzyme functionalized mesoporous thin silica films**

### **3.4.1 sp-Functionalization of trypsin**

The acetylene-functionalization of trypsin was already described elsewhere.<sup>184</sup> Briefly, the amount of 10 ml of a solution containing trypsin (1 mg/ml) in 2-(N-morpholino)ethanesulfonic acid (MES) buffer (10 mM, pH 5.5) was prepared. Subsequently, the amount of 500  $\mu$ l of an aqueous solution of 4-pentynoic acid (0.1 M) was added. The resulting mixture was vortexed for 2 minutes and then stored at 4°C for 15 minutes. Subsequently, the amount of 9.9 mg 1-ethyl-3-(3-dimethylaminopropyl) carbodiimide (EDC) hydrochloride was added. The resulting mixture was vortexed for 2 minutes. The reaction mixture was stored at 4°C for 4 h, after which time the sample was dialyzed in a cold room at 6°C against sodium phosphate buffer (10 mM, pH 7.2) for a period of 24 h. The resulting acetylene-functionalized trypsin was used for the click reaction without further purification.

### **3.4.2 Chloropropyl functionalized films by cocondensation**

In a typical experiment (according to literature,<sup>185</sup> slightly modified) 2 g TEOS, 1  $\mu$ l (3-Chloropropyl)triethoxysilane (Cl-TEOS), 8.8 g EtOH, 0.2 g 1M HCl and 1.4 g H<sub>2</sub>O were stirred at 65°C for one hour. The warm solution was mixed with 0.95 g Pluronic F127 in 8.8 g EtOH and stirred at room temperature for at least two hours. The molar ratio of the final synthesis solution was 1 TEOS :  $5.49 \times 10^{-4}$  Cl-TEOS :  $7.84 \times 10^{-3}$  F127 : 39.7 EtOH : 8.09 H<sub>2</sub>O :  $2.08 \times 10^{-2}$  HCl. Films were deposited on silicon wafers (~2.8 cm  $\times$  1.5 cm) or thin glass slides (2.5 cm  $\times$  2.5 cm) by dip coating at a speed of approximately 30 mm/min in a dry (5-15% r.h.) atmosphere.

### 3.4.3 Template removal

After a drying time of several hours at room temperature, the films were kept in an ammonia-saturated atmosphere for 30 min in order to stabilize the mesoporous structure by further condensation of residual silanol groups. The template could then be easily removed by washing the films several times with ~2 ml acetone followed by several ml of ethanol.

### 3.4.4 Azide exchange

Azide exchange was accomplished by placing the films in a stirred solution of saturated sodium azide in DMF at 85°C for 4 h. Afterwards, the films were stored several days in high purity ethanol to remove the last organic residues.

### 3.4.5 Enzyme attachment by click reaction

Covalent bonding of the modified trypsin was achieved through a Cu(I)-catalyzed Huisgen cycloaddition at 4°C over night. For this purpose the film was placed in 6 ml PBS buffer (pH 6.0) containing 300 µl of the sp-trypsin solution (~1 mg/ml), 1 µl vitamin C solution (6.6 mmol/l) and 1 µl CuSO<sub>4</sub> solution (0.66 mmol/l). After the click reaction the films were thoroughly washed with water and stored in PBS buffer (pH 6.0) at 4°C.

## 3.5 Synthesis of large domain mesoporous thin silica films

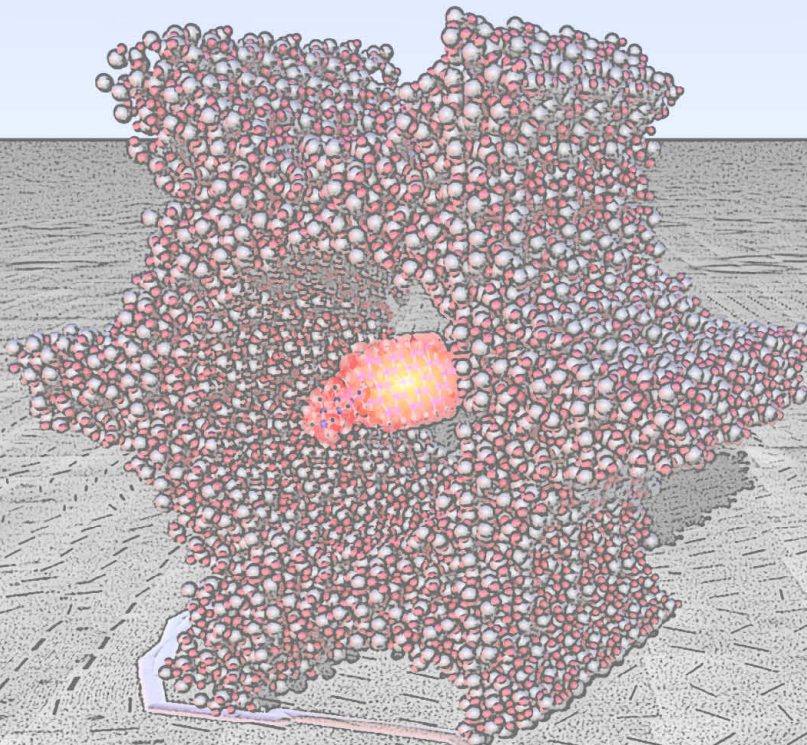
In a typical synthesis 1 g Pluronic F127, 17.6 g EtOH (spectroscopic), 1.4 g H<sub>2</sub>O and 0.2 g HCl (1M) were stirred at room temperature until a clear solution was obtained. 2 g TEOS were added and the solution was stirred for additional five minutes at room temperature. Afterwards, dip coating of silicon wafers was carried out in a dry atmosphere (< 10% r.h.) at a dipping rate of 0.45 mm/min, followed by framework stiffening and template removal according to section 3.4.3.







# 4



INTRODUCTION

EXPERIMENTAL METHODS

**RESULTS AND DISCUSSION**

CONCLUSION

APPENDIX



## 4 Visualizing single-molecule diffusion in mesoporous materials

As the molecular movement in the pore system is the most important and defining characteristic of porous materials,<sup>68</sup> it is of great interest to learn about this behavior as a function of local structure. Generally, individual fluorescent dye molecules can be used as molecular beacons with which to explore the structure of - and the dynamics within - porous hosts.<sup>135,183,155,156,186</sup> Single-molecule fluorescence techniques, for example, provide detailed insights into the dynamics of various processes, ranging from biology<sup>187,150</sup> to heterogeneous catalysis<sup>188</sup>. However, optical microscopy methods cannot directly image the mesoporous structure of the host system accommodating the diffusing molecules, whereas transmission electron microscopy provides detailed images of the porous structure,<sup>189</sup> but no dynamic information. It has therefore not been possible to “see” how molecules diffuse in a real nanoscale pore structure.

To reveal how a single luminescent dye molecule travels through linear or strongly curved sections of a mesoporous channel system electron microscopic mapping and optical single-molecule tracking experiments were combined. In a cooperation with Johanna Kirstein from the group of Prof. Bräuchle, we succeeded for the first time with the direct correlation of porous structures detected by transmission electron microscopy with the diffusion dynamics of single molecules detected by optical microscopy. This method could have the potential to open up new ways of understanding the interactions between host and guest.

The first step in order to apply single molecule and transmission electron microscopy successively on the same sample was the modification of an existing recipe for mesoporous films.<sup>135</sup> This recipe produces a phase mixture, indicated by two reflections in the 1D-XRD pattern (figure 4.1). They can be assigned to the lamellar (at  $\sim 1.4^\circ 2\theta$ ) and the 2D hexagonal (at  $\sim 1.6^\circ 2\theta$ ) structure, respectively. The thickness obtained by ellipsometry is about 200 nm. Three main modifications of the original recipe were necessary:

- The thickness of the mesoporous film had to be adjusted to less than 100 nm, in order to be transparent for the electron beam (section 4.1).
- The mesoporous structure had to be changed into a purely 2D-hexagonal phase (section 4.2).

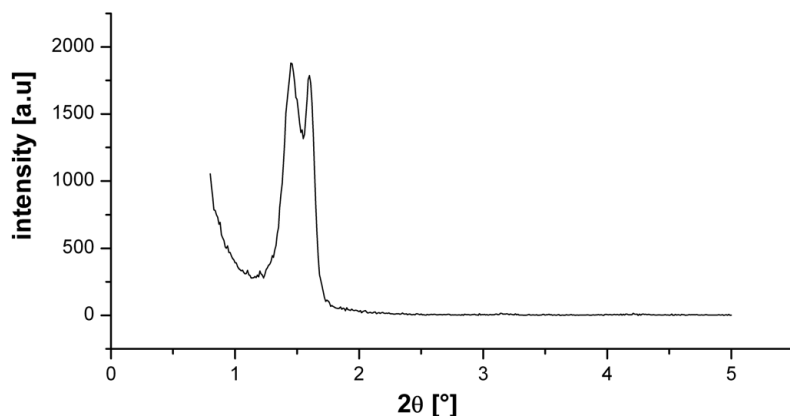


**Figure 4.1:** One-dimensional small angle X-ray diffraction pattern of a mesoporous film synthesized according to the original recipe. The two reflections indicate a mixture of a lamellar (at  $\sim 1.4^\circ 2\theta$ ) and 2D hexagonal structure (at  $\sim 1.6^\circ 2\theta$ ).

- Fluorescent dye molecules, as well as markers for the overlay and markers for merging multiple TEM micrographs had to be incorporated into the mesoporous structure (section 4.3).

After an appropriate mesoporous film and a suitable substrate were found, the samples were investigated by single-molecule fluorescence microscopy and then mapped in TEM without any additional sample preparation (sections 4.4 - 4.6). By the use of markers the data of both techniques are combined and provide new insights into the interactions between host and guest (sections 4.7, 4.8).

#### 4.1 Adjusting film thickness

Unless otherwise noted, the 1D-XRD patterns of the films synthesized in the following experiments do not have a significant deviation from the pattern in figure 4.1 and therefore the films should have in principle the same structure.

As the samples are synthesized by spin-coating in an EISA process the film thickness is highly dependent on the evaporation speed of the solvent. There are two main parameters that have a great influence on it, temperature and humidity. Experiments varying the temperature during spin-coating were rather hard to realize and unfortunately non-reproducible. But as the laboratories are air-conditioned and therefore the temperature only varies by 2 or 3°C, it was assumed constant. Spin-coating at different humidities could be carried out

much easier (section 3.3.2) and resulted in thinner films at higher humidities (figure 9.2). However, the adjustment of a certain humidity is difficult, so that this parameter was kept constant by floating the chamber of the spin-coater with dry air or nitrogen, adjusting the relative humidity to 0%.

Another well-known procedure exerting an influence on film thickness is calcination, meaning the removal of the template at higher temperatures ( $> 400^{\circ}\text{C}$ , see section 4.2). Calcination provokes contraction perpendicular to the substrate surface caused by the removal of residual water contained in the inorganic walls of the porous structure and by supplementary condensation between neighboring silanol groups<sup>190</sup>. The same mechanism is assumed for the aging of films at room temperature, even though the effect is not as striking as during calcination (figure 9.3).

A parameter with low influence on film thickness is the amount of solution dropped on the substrate before spin-coating (figure 9.4), indicating that before the critical micelle concentration is reached always the same amount of material is left on the substrate.

Of course, up to now the most influencing parameter was disregarded, the dilution of the parent solution. By dilution, the residual material on the substrate contains less building blocks and template. Therefore, thinner films are easily obtained (figure 4.2). The different behavior of water and ethanol as

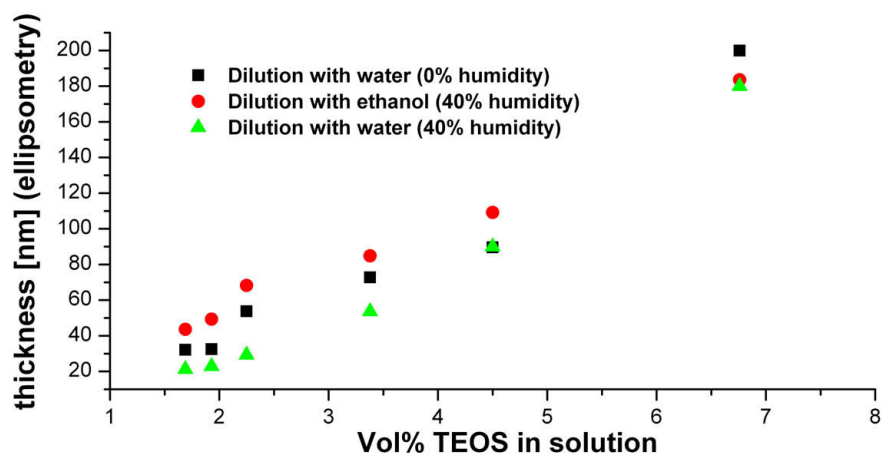


**Figure 4.2:** By dilution the film thickness decreases as expected, however the effect is not only affected by the amount of TEOS in solution and the humidity, but also by the solvent used for dilution.

solvents for dilution indicates already what is proven by the X-ray data of the dilution series with water. A dilution with EtOH does not affect the film structure, whereas a synthesis solution with higher water content produces more lamellary films (figure 9.5). This is important as the markers which have to be added to the solution (see section 4.3) are dissolved in water, implying a higher water content in the final synthesis solution.

## **4.2 Synthesis of thin mesostructured silica films with pure phases**

The main parameter for the film structure is the surfactant to silica ratio. From comparable surfactants it is known that with increasing amount of surfactant the structure changes from cubic to 2D hexagonal to lamellar.<sup>191</sup> As the original synthesis solution with a surfactant to silica ratio of 0.220 produces a mixture of 2D hexagonal and lamellar phases, pure cubic and pure 2D hexagonal structures should be accessible by decreasing the surfactant amount, whereas the lamellar phase should be obtained by increasing the Brij56 portion.

### **4.2.1 Films with 2D-hexagonal arrangement of rod-like pores.**

Mesoporous films were synthesized with a slightly lower surfactant amount than the original recipe. In addition the solution was diluted with half the volume of water in order to get thinner layers. The corresponding 1D-XRD data are depicted in figure 9.6 in the appendix section. At a surfactant to silica ratio of 0.170 both reflections of the pattern in figure 4.1 are still visible. At a ratio of 0.146 only the Bragg reflection caused by the hexagonal phase can be detected. By calcination at 500°C in air the template is nearly completely burned (see figure 9.7). The 1D-XRD pattern of the calcined film (see figure 9.8) still shows one reflection shifted to higher angles. This indicates a shrinkage perpendicular to the surface of about 35 %. The 2D hexagonal arrangement of the pores was proven by TEM (see figure 4.3a) and 2D SAXS measurements (see figure 4.3b). Both data clearly show the hexagonal order.

### **4.2.2 Films with cubic structures.**

As mentioned above further decrease of the surfactant to silica ratio should result in pure cubic phases. The corresponding 1D-XRD patterns are presented in figure 9.9. A significant shift of the reflection indicating a structural change is not visible. Therefore, any of these silica to surfactant ratios would probably

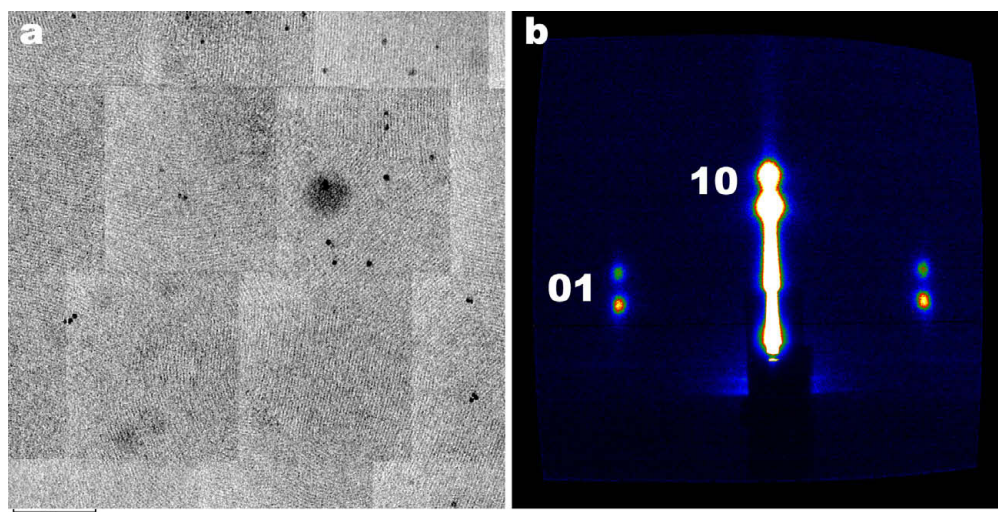


**Figure 4.3:** **a** TEM image of an as-synthesized 2D-hexagonal film on a thin Si<sub>3</sub>N<sub>4</sub> membrane. The channels are clearly visible and parallel to the substrate surface. **b** Two-dimensional GISAXS pattern of an as-synthesized film on a silicon wafer. The reflections show the typical pattern of a 2D hexagonal ordering. (Reflection splitting is caused by diffraction of the reflected zero beam.)

result in a cubic film. As the diluted solution produces films too thin, undiluted solutions were also used to synthesize thicker films. Their 1D-XRD patterns are shown in figure 9.10. At a ratio of 0.061 the lowest reflection shift in comparison to the thinner films is obtained, as well as the best signal to noise ratio. This recipe seems to produce cubic films with good quality depending only slightly on water dilution. The appropriate thickness was achieved by mixing the parent solution with 37.5 Vol% of water. The reflection shift after calcination (see figure 9.11) is not as strong as in hexagonally ordered films. It only corresponds to a shrinkage of 24 % and can be explained by the higher silica amount which results in a more stable framework. The cubic structure is also proven by TEM and 2D-SAXS (see figure 4.4a and 4.4b).

#### 4.2.3 Films with lamellar structure.

A higher surfactant to silica ratio in comparison to the original synthesis solution should result in lamellary ordered films. Corresponding 1D-XRD patterns are shown in figure 9.13. Too high surfactant amounts produce poorly ordered films, but a Brij56 to silica ratio of 0.487 seems to produce well ordered lamellar structures. Although the synthesis solution was diluted half the volume with water the resulting films are far too thick. That is why a dilution series



was performed (see figure 9.14) to estimate the optimal TEOS amount (see figure 9.15). 2.7 Vol% of TEOS, which corresponds to a dilution of the parent solution with 1.5 the volume of water seemed to be suitable. As expected the calcined film doesn't show the characteristic Bragg reflection anymore (see figure 4.5a). The remaining reflections correspond to the thickness of the amorphous silica layer of  $\sim 20$  nm (see 2.4.5). The nearly complete burning of the surfactant is proven by IR (see figure 9.16). TEM micrographs of lamellar films, including cross sections as well as removed pieces, never showed the characteristic layer stacking, but via 2D-SAXS measurements (see figure 4.5b) lattice planes parallel to the substrate could be proven. (This is characteristic for lamellar structures.) A possible explanation for the lack of structure in TEM is the decomposition and evaporation of surfactant within the TEM column due to the electron beam and the high vacuum. Thus the remaining silica layers collapse and the structure is destroyed. In fact, this is also a form of "calcination".

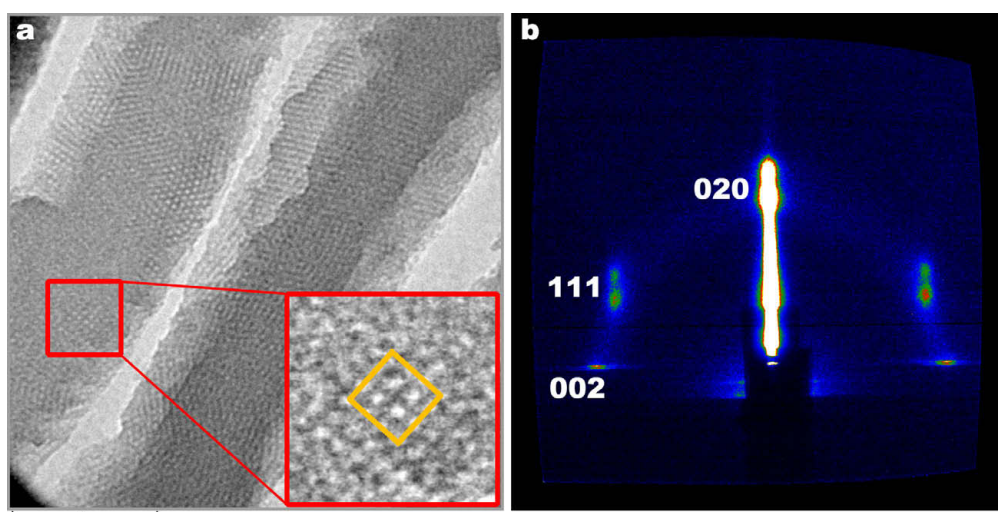


**Figure 4.4:** **a** TEM image of an as-synthesized cubic film scratched from a silicon wafer and transferred on a TEM carbon grid. Depending on the orientation, different patterns are observed. Characteristic for a cubic structure is a rectangular arrangement of pores (see magnified area in red box). **b** Two-dimensional GISAXS pattern of an as-synthesized film. The reflections show the typical pattern of a  $Im\bar{3}m/Fm\bar{3}m$  structure.<sup>192</sup> (Reflection splitting is caused by diffraction of the reflected zero beam.)

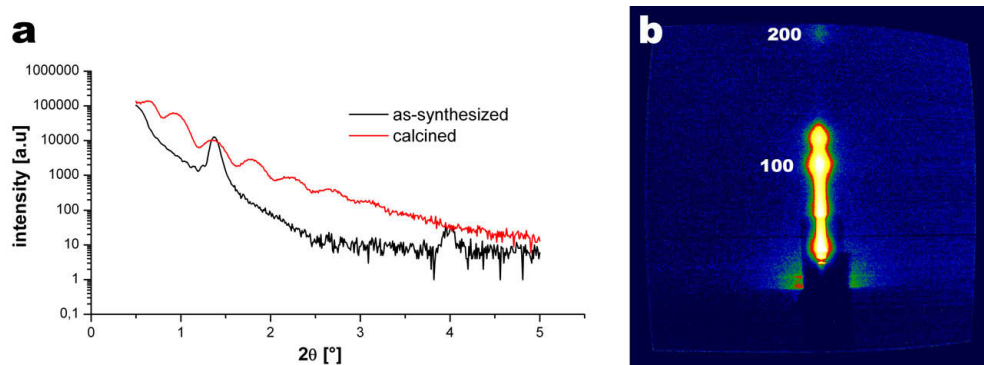


**Figure 4.5:** **a** 1D-XRD patterns of an as-synthesized and calcined lamellar film, respectively. (Intensity is plotted in logarithmic scale.) The characteristic Bragg reflection disappears upon calcination, indicating a destroyed structure. The residual reflections in the calcined sample result from X-ray reflection. **b** Two-dimensional GISAXS pattern of an as-synthesized lamellar film. Only the 100 reflection and higher orders are visible. (Reflection splitting is caused by diffraction of the reflected zero beam.)

### 4.3 Final recipe and reproducibility

Following the general synthesis procedure described in section 3.3 a parent solution with the corresponding template solution was mixed and diluted with water at the ratios shown in table 5. Reproducibility was tested by the syn-

Used template solution - amount Brij56 solved in 12.5 g EtOH (mg)	250	600	2000
Amount parent solution ( $\mu\text{l}$ )	400	400	200
Amount water ( $\mu\text{l}$ )	150	200	300
Resulting structure	cubic	2-D hexagonal	lamellar

**Table 5:** Parent solution for synthesis of pure phase films

thesis of three films of each phase and comparison of their XRD data and ellipsometry measurements. The data show a 5 % variation in film thickness and reflection shifts in the XRD pattern of  $\pm 0.05^\circ$   $2\theta$ . Both deviations are within the measuring inaccuracy. For single molecule tracking a 2D hexagonal phase was needed, as fluorescent dye molecules within the pores of cubic and lamellar structures would only show random walk, and, as mentioned above, markers for TEM mapping and for the overlay procedure have to be incorporated within the film. Therefore, 75  $\mu\text{l}$  of the undiluted solution for 2D hexagonal films were combined with 4  $\mu\text{l}$  of a highly diluted TDI solution

( $\sim 10^{-8}$  mol l<sup>-1</sup> in ethanol), 20  $\mu$ l of a gold colloid solution (diameter 5 nm, concentration corresponding to  $\sim 0.01$  % HAuCl<sub>4</sub>; Sigma-Aldrich), 15  $\mu$ l of a polystyrene bead solution (Polybead microspheres, diameter  $0.281 \pm 0.014$   $\mu$ m, 2.6% solids (latex); Polysciences) and 40  $\mu$ l of deionized water. The composition (molar ratio) of the final spin-coating solution was 1 TEOS : 0.144 Brij 56 : 0.06 HCl : 61.69 ethanol : 210 water.

#### 4.4 Using silicon nitride membranes as substrates

Normally mesoporous thin films are formed on silicon wafers or - if fluorescence microscopy should be applied - on thin glass cover slips. For TEM measurements both substrates are far too thick to be penetrated by the electron beam. In principle, there are only two ways getting TEM images of mesoporous thin films.

An easy method is scratching. With a razor blade small flakes of the mesoporous film are lifted off the substrate. The material is dispersed in a solvent (e.g. water or ethanol) and dropped onto a TEM copper grid covered with a thin carbon layer. But due to self-fluorescence of the carbon layer and a random orientation of the mesopores in all three dimensions, an overlay is not possible. Other attempts to directly synthesize the mesoporous thin films on TEM copper grids covered with thin SiO layers (e.g. by spin-coating) were also not successful. This is probably due to the corrugation of the SiO layer caused by the copper grid.

Another widely used preparation technique for TEM measurements of mesoporous materials is the so-called cross-section. The material is embedded in epoxy resin and a small slice is cut out. After grinding, dimpling and ion milling only a small fringe encircling the opening is thin enough to be penetrated by the electron beam. However, not only is this area quite small for optical microscopy, the whole procedure can damage the mesoporous structure and is therefore not applicable for the purpose of this study.

That is why a substrate was needed that makes sample preparation after synthesis unnecessary. The solution was a 30 nm thin Si<sub>3</sub>N<sub>4</sub> membrane on top of an etched silicon wafer, forming a quadratic window with a side length of 500  $\mu$ m. The membrane is stable enough for film synthesis and at the same time nearly as flat as a silicon wafer. The fluorescence background caused by the membrane is acceptable and the substrate can be purchased from TEM suppliers. Due to the short working distance of the used objective ( $\sim 300$   $\mu$ m),

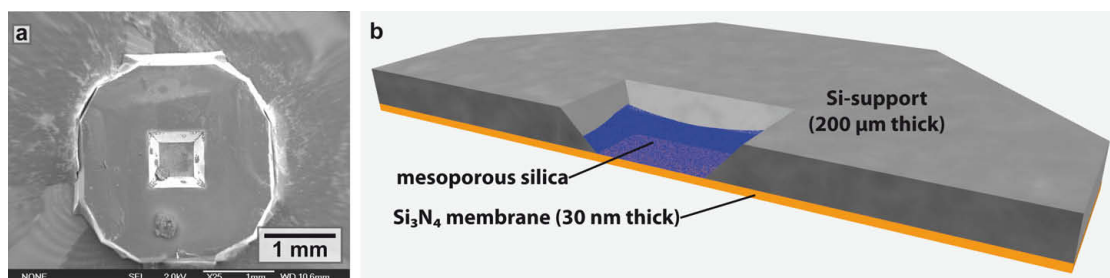


**Figure 4.6:** **a** SEM image of a coated membrane. The etched window is clearly visible. **b** Scheme of coated membrane. The increasing film thickness near the window borders is caused by the spin-coating process.

the mesoporous film was spin-coated into the interior of the membrane window (see figure 4.6).

#### 4.5 Widefield microscopy and Single Particle Tracking

At first the membrane was mapped in white-light transmission merging single images of adjacent areas (see figure 4.7a) using the ‘Photomerge’ function of Adobe® Photoshop® software (Version CS2). Then series of 1,000 images were acquired with a temporal resolution of 200 ms per frame. In each movie frame, single molecules show up as bright spots. Because the  $\text{Si}_3\text{N}_4$  membranes give a relatively high and inhomogeneous background signal, the background was subtracted frame to frame from the films before tracking of the molecules. Single-molecule trajectories were then built up by fitting the positions of the spots from frame to frame. The individual molecule patterns are fitted by a gaussian function

$$f(x, y, A, w) = Ae^{-\left(\frac{x-x_0}{w}\right)^2} e^{-\left(\frac{y-y_0}{w}\right)^2}$$

with a positioning accuracy of down to 10 nm, where A and w are the amplitude and the width of the gaussian curve, respectively. Because the films were much thinner than the focal depth of the microscope objective used ( $>1 \mu\text{m}$ ), images contain data from molecules at all heights inside and on the surface of the sample.

To overlay these trajectories on the TEM images, the positions of the polystyrene beads had to be determined from the same movie. For this purpose the laser shutter was closed for the last 240 frames of the movie and the polystyrene beads were imaged in transmission in white light (see also Supplementary Movie 1 on the CD). Their positions were fitted in inverted images with the same

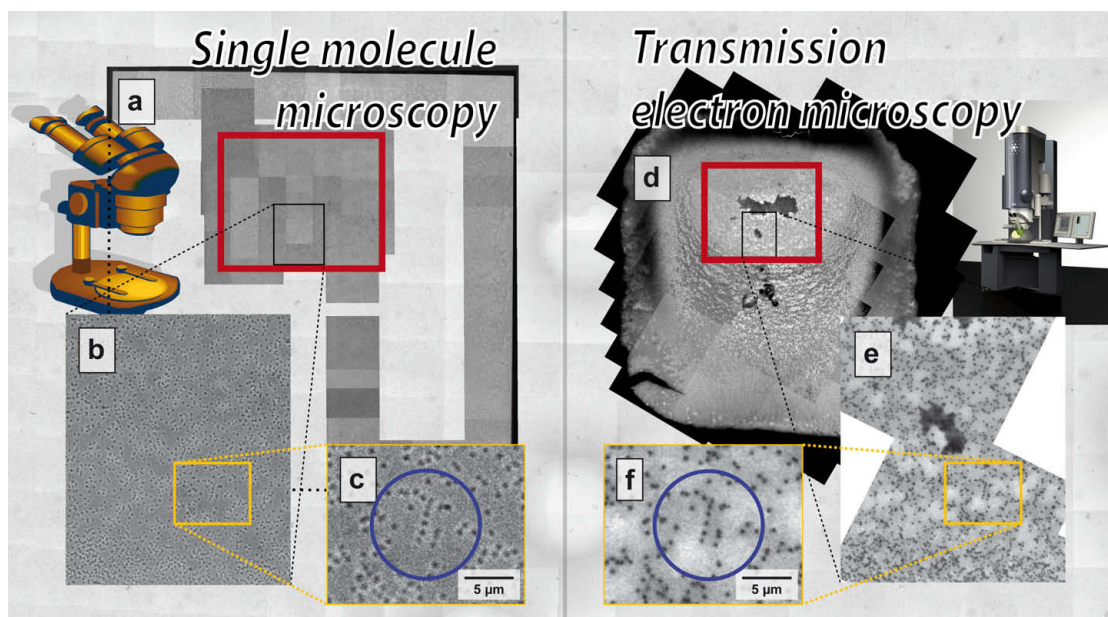


**Figure 4.7:** **a** Optical white light transmission images were merged together to give an impression of the whole sample ( $\sim 500 \mu\text{m} \times 500 \mu\text{m}$ ) and to define an area of interest (red box). **b** In this area a characteristic arrangement of PS spheres (**c**) is identified. **d** In TEM a map of the whole membrane was also created by merging several low resolution images and the region of interest was identified (red box). **e**, **f** At higher magnifications the characteristic arrangement of PS spheres could be retrieved.

gaussian fit routine as the single molecules (red crosses in figure 4.9a). Mean and standard deviations of the fitted positions were calculated and tabulated.

#### 4.6 Transmission electron microscopy

After optical microscopy the sample was analyzed with TEM. Again, during the first step the whole membrane was mapped at low resolution (see figure 4.7d). The central region with the appropriate thickness was then mapped at a magnification high enough to distinguish single polystyrene beads (see figure 4.7e). In this map we could retrieve the same geometric arrangement of polystyrene beads as in the white-light transmission images (see figure 4.7f). In all, 400 ( $20 \times 20$ ) images in the neighborhood of the tracked trajectories were taken at  $\times 40,000$  magnification using the software-controlled mapping function of the microscope's charge-coupled device camera. The single images were merged using the 'Photomerge' function of Adobe<sup>®</sup> Photoshop<sup>®</sup> software (Version CS2) to obtain a map of an area of about  $3.5 \mu\text{m} \times 3.5 \mu\text{m}$  (see fig-



ure 4.8a). The center positions of the polystyrene spheres in the TEM images were determined by fitting a circle on the outside margin of their patterns using DigitalMicrograph™ (see 9.4.1). To show the orientation of the pores in the TEM images better, fast Fourier transformation (FFT) was applied to adjacent square regions of 133 nm × 133 nm. The results of the FFT are plotted as black lines. The orientation of each ‘director’ depicts the average orientation of the pores in the square region around it, and the line thickness is a measure for the intensity of the maxima in the FFT fit and thus for the degree of structural order in this region. In addition to the orientation of the channels, these directors give a good overview of domain size and domain borders (see figure 4.8b). Calculating the FFT directors of all TEM maps is done by a script executed in DigitalMicrograph™ (see 9.4.2).

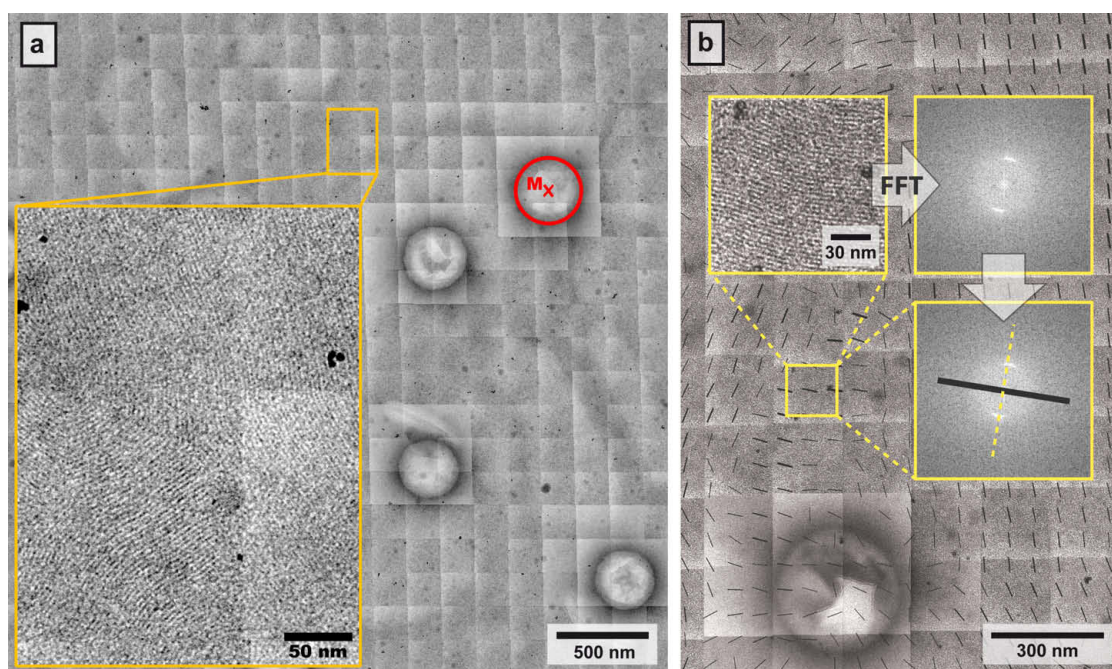


**Figure 4.8:** **a** 400 (20 × 20) single TEM images are merged together to obtain an area of about 3.5 μm × 3.5 μm. The magnification (× 40,000) is chosen high enough to resolve the structure of the mesoporous channel system (orange inset). The position of the PS beads is determined by fitting a circle to their borders (red circle). **b** Fast Fourier transformation (FFT) was applied to adjacent square regions of 133 nm × 133 nm. The main direction of the channel system is depicted by a line perpendicular to the two maxima in the FFT, as the structure is 2D hexagonal. The line thickness corresponds to the intensity of the maxima and is therefore a degree of structural order in this region.

## 4.7 Overlay

Overlays of TEM and wide-field images were accomplished by fitting the best overlay of the polystyrene bead positions in the respective images by the use of a script written in php (see 9.4.3). First the original positions of the PS beads in pixel are given. From these data scaling and rotation of the optical image with respect to the TEM map are calculated. Then an iterative algorithm is used to determine the translation producing the smallest over-all positioning error. With these three values (scaling, rotation and translation) the overlay was performed using Adobe® Illustrator® software (see figure 4.9). Table 6 shows the positions of the four PS beads used for the overlay of TEM images and wide-field data in figure 4.9 before and after the fitting procedure. In the TEM images (columns two and three) the positions are given in units of nanometer. Before the overlay the bead positions in the wide-field images are tabulated in units of pixel on the CCD chip of the set-up, as in the raw tracking data (columns four and five). The scaling factor should thus be equal to the experimentally determined magnification of the microscope setup of 122 nm per pixel (see 3.2), which is indeed the case. The deviations of the bead positions in TEM and wide-field after the fitting procedure are shown in the last column. Their average value is 26 nm, which is taken as a measure for the accuracy of the overlay. The two beads at the left edge of the TEM image are too close to

Bead	Position in TEM		Position in Widefield before overlay		Overlay	Position in Widefield after overlay		Deviation (nm)
	X in nm	Y in nm	X in px	Y in px		X in nm	Y in nm	
1	1680	1781	18.73	28.62	<b>Factor</b> <b>121.3</b> <b>Angle</b> <b>156.7</b>	1698	1814	37
2	2668	2983	15.13	16.62		2675	2977	9
3	1660	1130	16.98	33.95		1637	1136	23
4	801.6	1830	25.48	31.69		799	1796	34
Average								26

**Table 6: Bead positions in the TEM images and in wide-field tracking data of figure 4.9 before and after the overlay procedure.**

be resolved by optical microscopy. They are therefore not included in the overlay process. However, in some cases such pairs of closely neighboring beads had to be used for the overlay to have a minimum of three anchor points for the overlay. In such cases, the individual positions of the closely neighboring



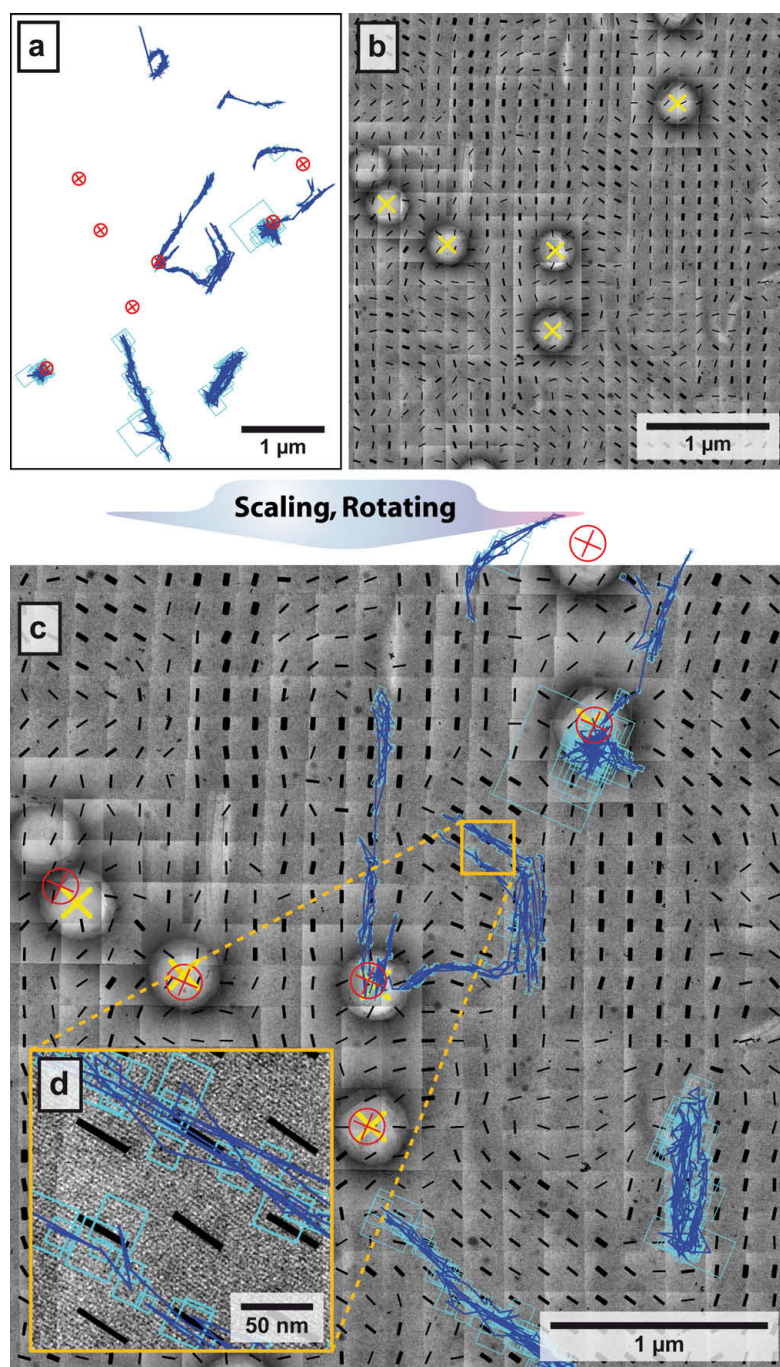


**Figure 4.9:** **a** Diffusion pathways of single molecules through the pore system (blue trajectories) and positions of the polystyrene beads (red crosses). **b** The same area as in **a** is imaged by TEM, with lines indicating the direction of the channels (FFT directors) and yellow crosses marking the centers of the polystyrene beads. **c** Final overlay of trajectories on TEM images; this was obtained by fitting to the best overlay of the polystyrene bead positions. **d** Enlargement of a region in **c**, showing the trajectories running along the channels.

beads were determined in the TEM images. The center position between the two beads was then correlated with the center position of the single spot resulting from the two beads in the respective white-light transmission images, fitted by the gaussian function. For example, in figure 4.12 two such doubled beads had to be used for correlating tracking data and TEM images, which resulted in an average deviation of 48 nm. Altogether five maps were overlaid with their corresponding fluorescence tracking data. The deviation in all maps is about  $29 \pm 13$  nm (see table 9 in appendix).

## 4.8 Results

The combination of the two techniques provides the first direct proof that the molecular diffusion pathway through the pore system correlates with the pore orientation of the two-dimensional hexagonal structure. In addition, the influence of specific structural features of the host on the diffusion behavior of the guest molecules can be clearly seen. With this approach we can uncover, in

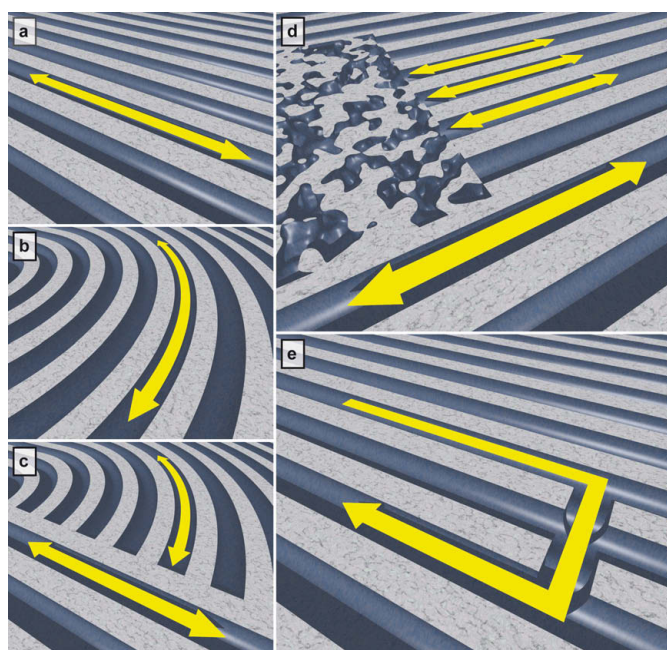


**Figure 4.10: Structural elements found in real two-dimensional hexagonal mesoporous silica film.** Straight **a** and curved **b** segments. **c**, Domain boundaries forcing molecules to turn back. **d**, Molecular travel stopped at less ordered regions. **e**, Lateral motion between neighboring channels.

unprecedented detail, how a single fluorescent dye molecule travels through linear or strongly curved sections of the hexagonal channel system in a thin

film of mesoporous silica (as sketched in figure 4.10a, b), how it changes speed in the channel structure, and how it bounces off a domain boundary with a different channel orientation (see figure 4.10c). Furthermore, we can show how molecular travel is stopped at a less ordered region (see figure 4.10d), or how lateral motions between 'leaky' channels allow a molecule to explore different parallel channels within an otherwise well-ordered periodic structure (see figure 4.10e).

Figure 4.11 and 4.12 depict several examples of specific pore ordering, indicated by the FFT directors, in combination with the overlaid trajectories, showing the various structural features that are shown in figure 4.10. The positioning errors for the single molecule trajectories are shown by the light blue boxes, which indicate the standard deviation of the fitted (x,y) positions. It is in the range of only 10 - 20 nm; the molecular positions can therefore be assigned to an ensemble of about five to ten parallel channels. Figure 4.11a depicts a trajectory of a molecule that is following the porous system along different structural domains. The corresponding wide-field movie and the tracked trajectory of the single molecule overlaid with the TEM images are provided in Supplementary Movie 1 and 2 on the CD. In this case the average deviation of the overlaid images is 34 nm. The molecule in figure 4.11a and Supplemen-

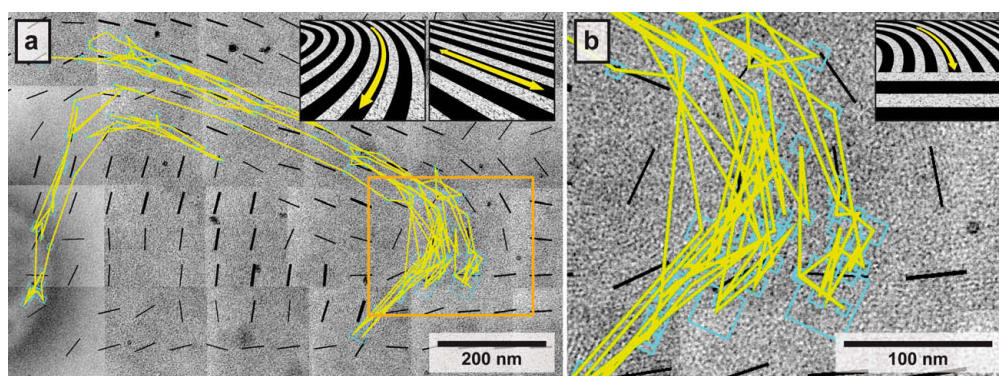


**Figure 4.11: Structural elements and molecular trajectories found in a real two-dimensional hexagonal mesoporous silica film.** **a**, Molecule exploring regions of parallel channels, strongly curved regions and domain boundaries. **b**, Magnified area from **a** showing the domain boundary at which the molecule is forced to turn back.

tary Movie 2 diffuses along linear pores in the middle part of the trajectory and follows the curvature on the right and on the left side. In addition, it is forced to turn back at a domain boundary, as shown in more detail in figure 4.11b. The insets in the upper right corners of figure 4.11a, b show the different



structural elements of this trajectory that were sketched in figure 4.10. To analyze the diffusion along this trajectory the data points were projected onto a manually defined backbone of the trajectory. Then the averaged mean-square displacement  $\langle r^2 \rangle$  along the backbone is plotted as a function of time. The linear relation of  $\langle r^2 \rangle$  with time was fitted in accordance with the Einstein-Smoluchowski equation for onedimensional (1D) diffusion for the first few time lags,<sup>160</sup> resulting in a 1D diffusion coefficient  $D_{1D}$  of  $(3.2 \pm 0.1) \times 10^2 \mu\text{m}^2 \text{s}^{-1}$ . It is important to analyze the 1D diffusion along the backbone, because the  $r^2$  in the curved region would otherwise tend towards smaller values for longer time lags.

Figure 4.12a shows another example of a molecule faithfully following the pores and mapping out specific elements of the host structure (see also Supplementary Movie 3 on the CD). Here the average deviation of the overlay is 48 nm. In this case only one single bead and two pairs of closely neighboring beads could be used for the overlay, which explains this relatively high value. The molecule was blinking several times for intervals of up to 6.6 s, and the trajectory is therefore divided into 11 parts, with durations ranging from 0.6 s to 11.8 s, shown in different colors. The perfect overlay of the S-shaped trajectory on the pore system is shown well by the FFT directors.

In figure 4.12b-d the specific regions marked with rectangular boxes in figure 4.12a are shown, and the insets sketch the different behaviors at specific regions of the trajectory (as in figure 4.10). Although the resolution of the optical microscope was not high enough to assign the position of a molecule to one specific channel, the width of the middle of this trajectory (magnified in figure 4.12b) shows that the molecule was moving in different straight parallel channels of the same domain. Especially interesting is the short element at the end of the yellow trajectory where the molecule makes a U-turn and diffuses back in a parallel track that is different from the original track, as shown at the left of figure 4.12b. On the basis of the spatial resolution of the optical pathways, we conclude that the molecule is diffusing in different parallel pores. At the left end of the trajectory in figure 4.12a the molecule diffuses in a well-ordered straight structure and bounces back repeatedly from an amorphous region having no apparent pore ordering, as shown in figure 4.12c. At the right of figure 4.12a a domain boundary region is visible; this structure is shown in more detail in figure 4.12d. Here, the molecule bounces back from the domain boundary with channels having different orientations, as sketched in figure 4.10c and in the inset.

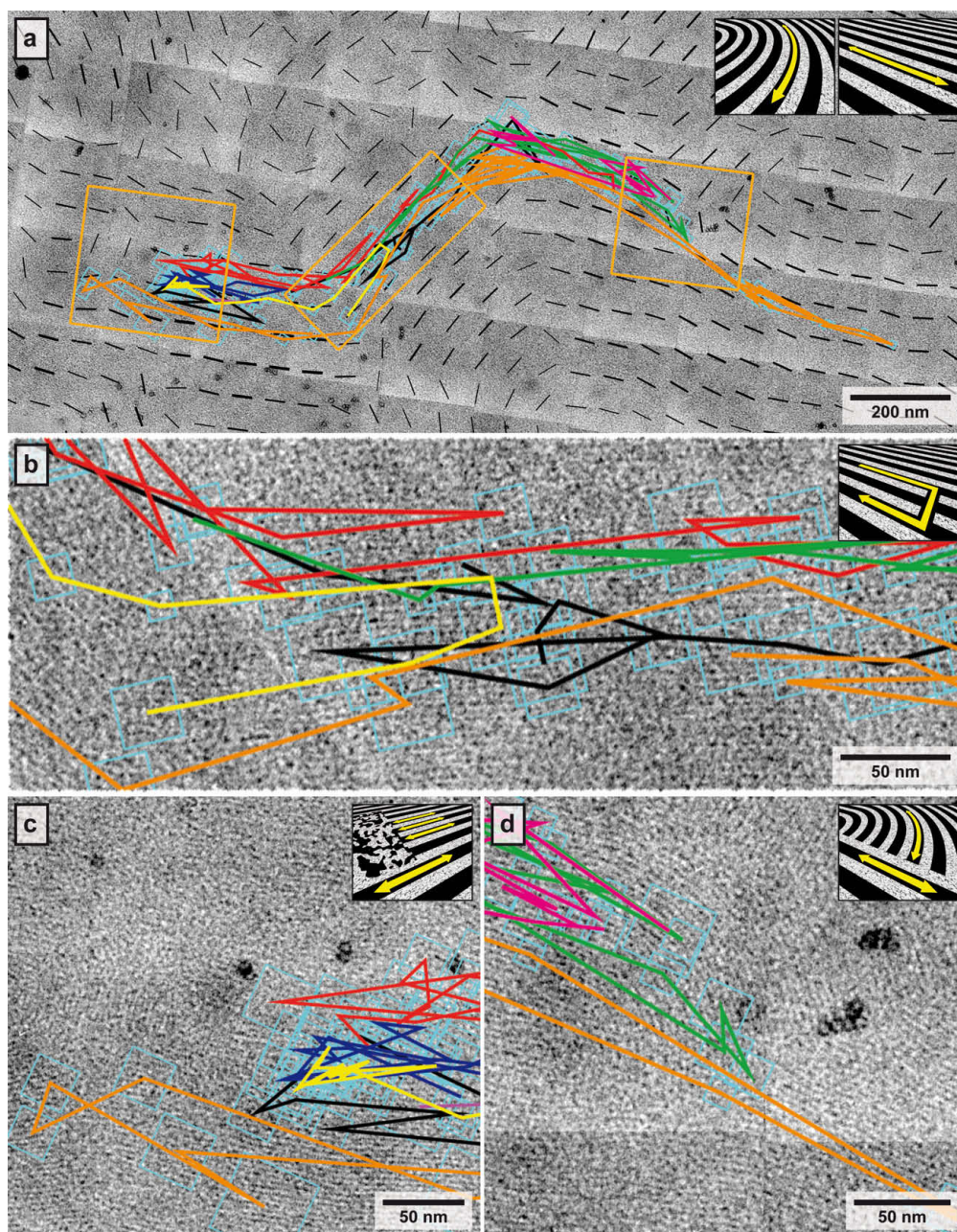


**Figure 4.12: Structural elements and molecular trajectories found in a real two-dimensional hexagonal mesoporous silica film.** **a**, Trajectory of another molecule, showing an S shape corresponding to the underlying channel structure. The trajectory is divided into several sections as a result of blinking of the fluorescent molecule; the sections are plotted in different colors. **b**, Lateral motions between 'leaky' channels (yellow trajectory). **c**, Area in which the molecular movement is stopped at a less ordered region. **d**, Forcing of the fluorescent molecule to turn back (green pathway) at a domain boundary. In all panels the light blue boxes depict the standard deviation of the fit to the single-molecule signals; that is, the positioning accuracy. Movies showing the diffusion of the single molecules in **a** and **c** are available as Supplementary Movies 1, 2 and 3 on the CD.

The orange lines in figure 4.12d are situated slightly above the region of linear channels. However, if the average deviation of the overlay of 48nm is taken into account it is highly probable that the molecule was actually diffusing along the linear structure in the bottom region of the figure. Furthermore, one should keep in mind that we are sampling diffusion at discrete points in time and space. The connecting lines are just a method of visualizing the trajectories; they do not represent the molecules' exact path.

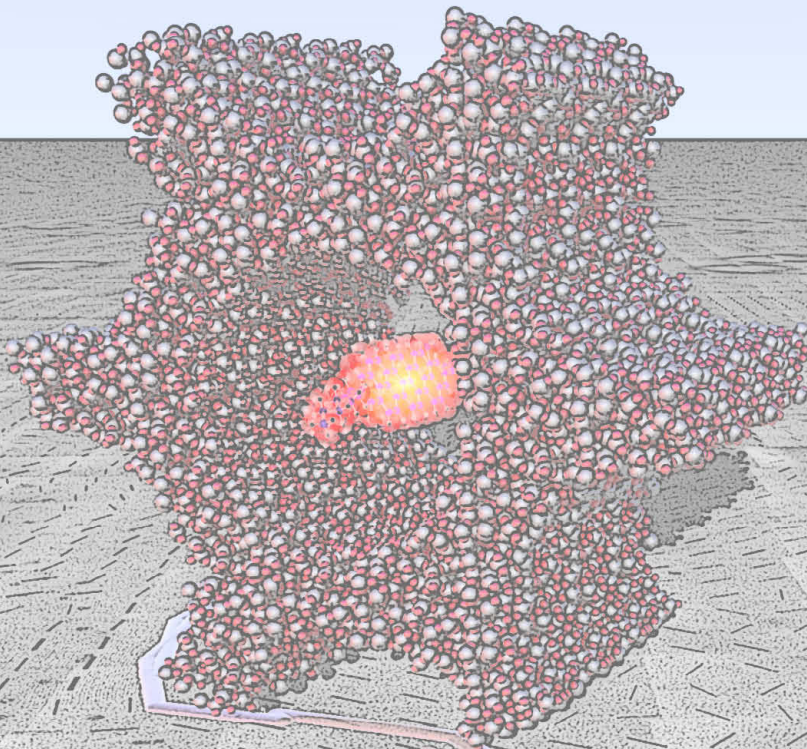
Projection of the trajectory shown in figure 4.12a onto its backbone and calculation of the average diffusion coefficient along the backbone gives  $D_{1D} = (3.0 \pm 0.1) \times 10^2 \mu\text{m}^2 \text{s}^{-1}$ . In addition, we calculated the following individual average diffusion coefficients for the parts of the trajectory showing no blinking for at least 20 frames: red (frames 1-33),  $D_{1D} = (3.6 \pm 0.2) \times 10^2 \mu\text{m}^2 \text{s}^{-1}$ ; green (frames 37-82),  $D_{1D} = (1.1 \pm 0.1) \times 10^2 \mu\text{m}^2 \text{s}^{-1}$ ; blue (frames 100-119),  $D_{1D} = (1.0 \pm 0.1) \times 10^2 \mu\text{m}^2 \text{s}^{-1}$ ; yellow (frames 135-157),  $D_{1D} = (2.0 \pm 0.1) \times 10^2 \mu\text{m}^2 \text{s}^{-1}$ ; orange (frames 176-244),  $D_{1D} = (5.5 \pm 0.1) \times 10^2 \mu\text{m}^2 \text{s}^{-1}$ ; and violet (frames 308-328),  $D_{1D} = (1.3 \pm 0.1) \times 10^2 \mu\text{m}^2 \text{s}^{-1}$ . Parts of the trajectory with fewer than 20 points are drawn in black. The noticeable changes of the 'local' diffusion coefficient show that the diffusion behavior of the molecules is strongly dependent on the surrounding pore structure. When the molecule is 'bouncing back' at an unstructured region, as in the dark blue part of the trajectory,  $D_{1D}$  is smaller than in regions where the molecule is diffusing along the trajectory (orange and red). On average the values are in the same range as the diffusion coefficient for the U-shaped trajectory shown in figure 4.11a and also many other trajectories observed in the same sample (not shown).

In this study we correlate directly the dynamic information from the diffusion trajectories of single guest molecules with the detailed structure of the porous host in regions up to  $3.5 \mu\text{m} \times 3.5 \mu\text{m}$  in size. This approach reveals the nature of the real space porous defect structure, as detected by the movement of fluorescent single molecules, containing linear or strongly curved sections of the hexagonal channel system, domain boundaries, boundaries between ordered and disordered sections, and 'leaky' channels that permit lateral travel. We emphasize that our approach provides detailed information on the real defect structure of porous materials with high spatial resolution that cannot be obtained by scattering methods because of the intrinsic averaging effects. Similarly, we also obtain highly resolved dynamic information in real time that cannot be extracted from conventional diffusion techniques because of ensemble averaging. This new methodology is expected to provide detailed insights

into the real structure and dynamics of other classes of porous materials and important host-guest systems, such as bioactive molecules in porous materials for drug delivery or reactants in porous catalysts.



# 5



INTRODUCTION

EXPERIMENTAL METHODS

**RESULTS AND DISCUSSION**

CONCLUSION

APPENDIX



## 5 Enzymes covalently bound to the surface of mesoporous thin films

Based on their superior selectivity and activity at moderate temperatures, enzymes are attractive catalysts with numerous industrial and consumer uses such as detergents, starch saccharification, food and feed additives, fuel alcohol production, and also in the pulp and paper industry.<sup>193-199</sup> An important issue in catalytic reactions is the separation of the catalyst from the product after reaction. In the case of enzymes, this is mainly realized in three different ways: Carrier binding, cross-linking, and entrapment,<sup>200</sup> whereas carrier binding is achieved by covalent or ionic bonding or physical adsorption. Immobilized enzymes can offer advantages such as enhanced stability, repeated or continuous use, possible modulation of the catalytic properties, prevention of protein contamination in the product, and effective prevention of microbial contaminations.<sup>201</sup>

But, often immobilized enzymes show a lower activity than free biocatalysts. Possible explanations are steric hindrances due to confined space in a porous host or slight changes in enzyme conformation due to functionalization needed for binding. SMM would be an excellent tool for observing such effects, as the pathway of both species, enzymes as well as substrates, can be followed by tagging with fluorescent dyes. In addition, techniques using Förster resonance energy transfer (FRET) allow the determination of distances in the nanometer range, for example for detecting substrate conversion or enzyme conformation.

Therefore, the original intention of this section was the visualization of an enzymatic reaction within the pores of a mesoporous thin silica film. It was planned to decorate the enzyme with gold clusters acting as markers for TEM and labeled with a fluorescent dye for SMM. Both ends of a suitable substrate should be tagged with dyes capable to do FRET. The pathway of the substrate would be followed and by FRET its conversion could be detected. The positions of the enzyme in SMM and TEM would then be used to overlay both data as it was done in the previous section in order to correlate the enzyme activity with the real mesoporous structure.

During this work at least two main challenges were mastered. On the one hand a covalent bonding of trypsin to the pore walls of a mesoporous thin silica film was achieved and the catalytic activity of the enzyme functionalized sample was proven (described in this section). On the other hand the domain

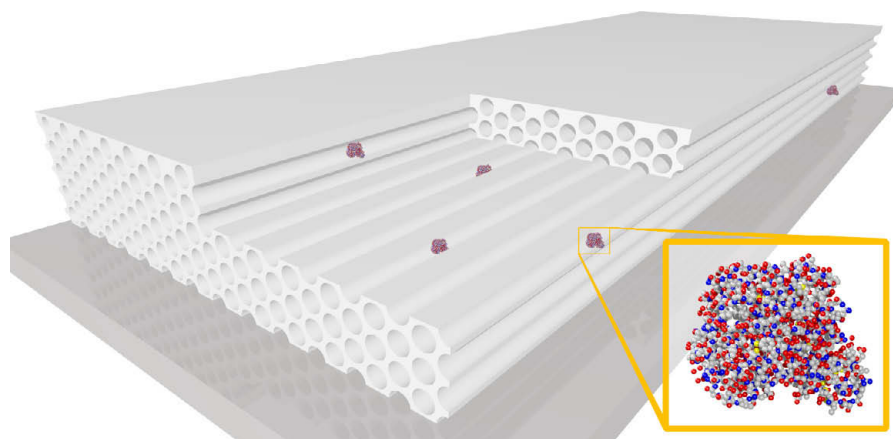


**Figure 5.1: Enzyme functionalized mesoporous silica thin film.** Scheme of a 2D hexagonal mesoporous film on a silicon wafer with covalently bound trypsin (inset) molecules.

size of the mesoporous structure of such a film was drastically increased in comparison to section 4 (described in the following section).

## 5.1 Covalent binding

A low binding energy between enzyme and support associated with physical adsorption can create issues such as enzyme leaching<sup>202,203</sup> and repeated or continuous use can become problematic. Usually, the most efficient immobilization is achieved if the enzymes are covalently bonded to porous supports, for example sol-gel glasses or ordered mesoporous silica materials,<sup>33,39</sup> as sketched in figure 5.1. The latter materials offer large, regular pores (up to 30 nm), high surface areas and allow a precise control over pore size.

Several methods have been reported for covalent enzyme binding to supports, e.g., with cyanogen bromide, condensing reactions and diazo-coupling or epoxide functionalities,<sup>204</sup> but to the best of our knowledge enzymes have not yet been covalently attached to mesoporous thin films. Although, catalytically active thin films are highly desirable for a number of applications, including biosensors<sup>205</sup>, optical investigations of enzyme reactions<sup>206</sup> or as active layers in microreactors<sup>207</sup> or microfluidic devices.

In this chapter the covalent binding of trypsin to the pore walls of a mesoporous thin silica film by the use of a copper(I)-catalyzed Huisgen 1,3-dipolar cycloaddition of alkyne and azide functionalities (“click-reaction”) is reported. This regioselective reaction can be performed at room temperature in very short

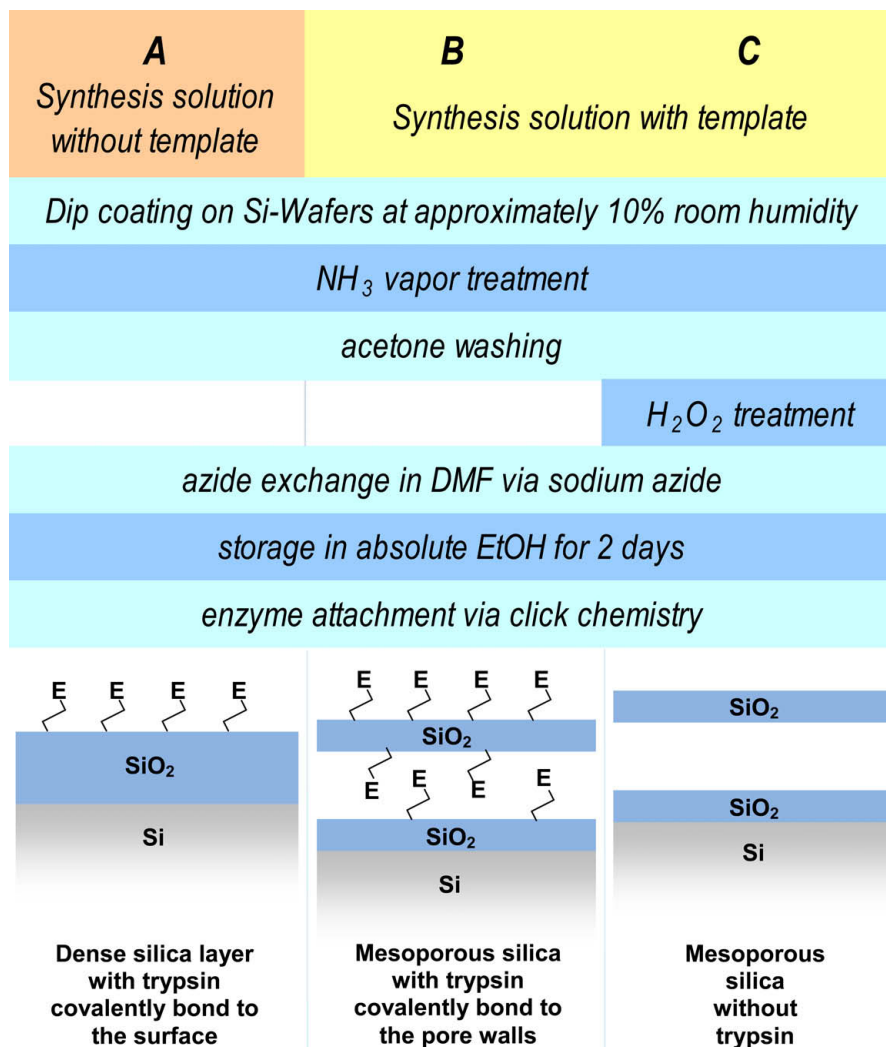


**Figure 5.2: Samples A, B and C for investigation of enzyme effectivity.** Sample A represents a dense silica layer with enzymes bound to the surface. As sample B is mesoporous the surface is larger and therefore more enzyme is bound. By  $H_2O_2$  treatment the organic linkers are destroyed and so no enzyme molecules are attached to the surface.

reaction times, it is bio-compatible, and this approach was already successfully applied on micrometer sized mesoporous silica spheres.<sup>184</sup> Regarding the reactants, Cu(I) is inexpensive and both alkyne and azide functional groups can be incorporated into a wide range of compounds by several very general methods.<sup>208,209</sup>

## 5.2 Synthesis

A general film synthesis is described in section 3.4. By ellipsometry measurements the thickness was determined to approximately 130 nm. To investigate the enzyme activity three different samples (A, B and C, according to figure 5.2) were prepared. Sample A was dip coated from a solution containing no F127 in order to give a non-porous dense silica layer with a little amount of Cl-propyl linkers on the surface. Samples B and C were dip coated from a solution with template, resulting in thin mesoporous silica layers with 2D-hexagonal structure (see figure 5.3).

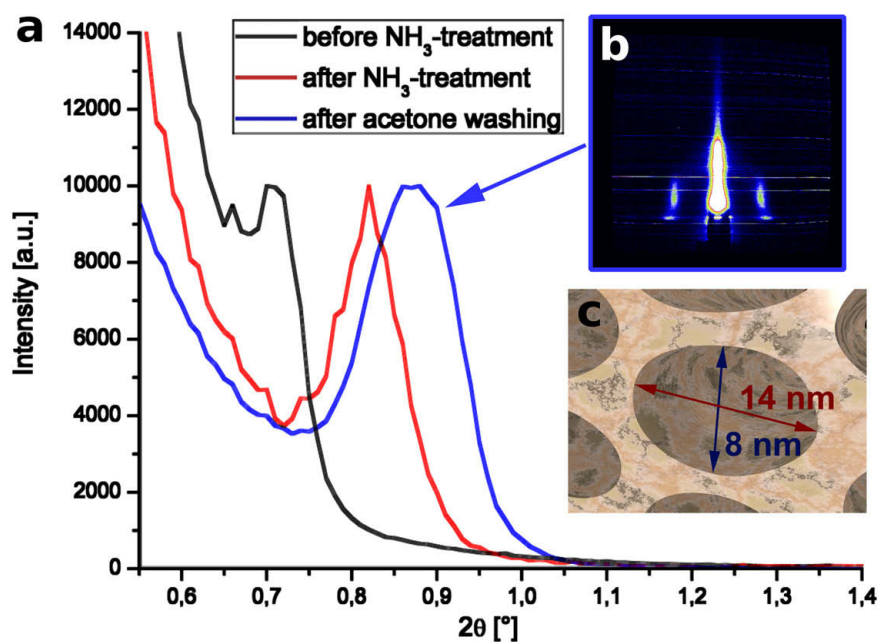


**Figure 5.3: XRD patterns of sample B after different synthesis steps.** **a** The 100 reflection is shifted to the right representing a decrease in d-spacing from about 12.5 nm to 10 nm. (The 100 reflection in all patterns is normalized to 10000 a. u.) **b** Inset shows the 2D-GISAXS data of a template-free film on silicon. (The shrinkage of about 36% is clearly visible.) **c** With an estimated pore wall thickness of 2 nm the pore has an elliptical shape with diameters of 8 and 14 nm.

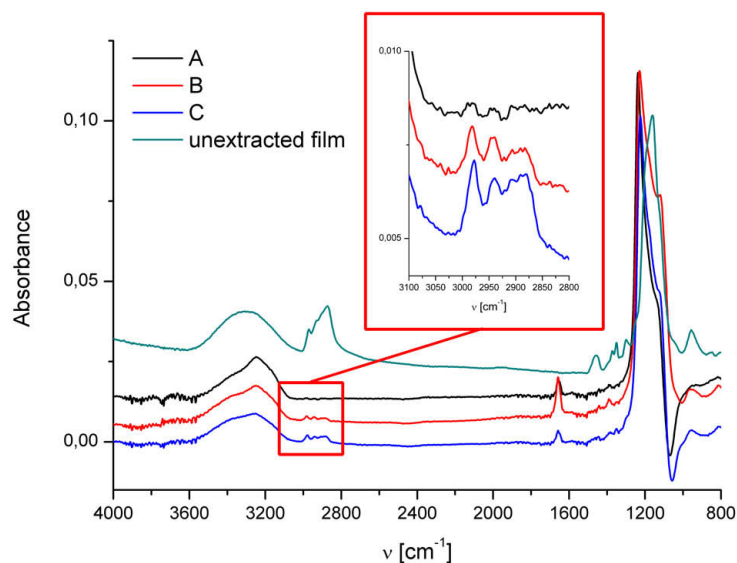


**Figure 5.4:** RAIR measurements of samples A, B and C before enzyme attachment and of an unextracted film. The bands from  $2800\text{ cm}^{-1}$  to  $3000\text{ cm}^{-1}$  indicate organic residues in all three samples, but these residues are strongly minimized in comparison to the as-synthesized sample.)

All three samples were treated according to the procedure described in section 3.4 and in figure 5.2. Additionally, sample C was put for 30 min in 30%  $\text{H}_2\text{O}_2$  at  $70^\circ\text{C}$  prior to azide exchange.<sup>210</sup> Before enzyme attachment via click chemistry the organic components in the films were investigated by reflection absorption IR (RAIR) measurements (figure 5.4). As sample A does not contain any template, the organic bands visible in the spectrum represent the amount of linker. Based on these data and comparing with the spectra of samples B and C, we can conclude that sample B and C still contain some template. As this residual template could not be washed out by extraction, even after a  $\text{H}_2\text{O}_2$ -treatment, and because the SEM images show some 3D hexagonal areas, an explanation could be that during film formation some F127 micelles were completely surrounded by silica and not accessible for solvents any more.

### 5.3 Activity measurement

Conventional characterization methods such as NMR, Raman or IR could not be used for enzyme quantification in sample films, as the amount of enzyme is below the detection limits. However, fluorescence spectroscopy is sensitive

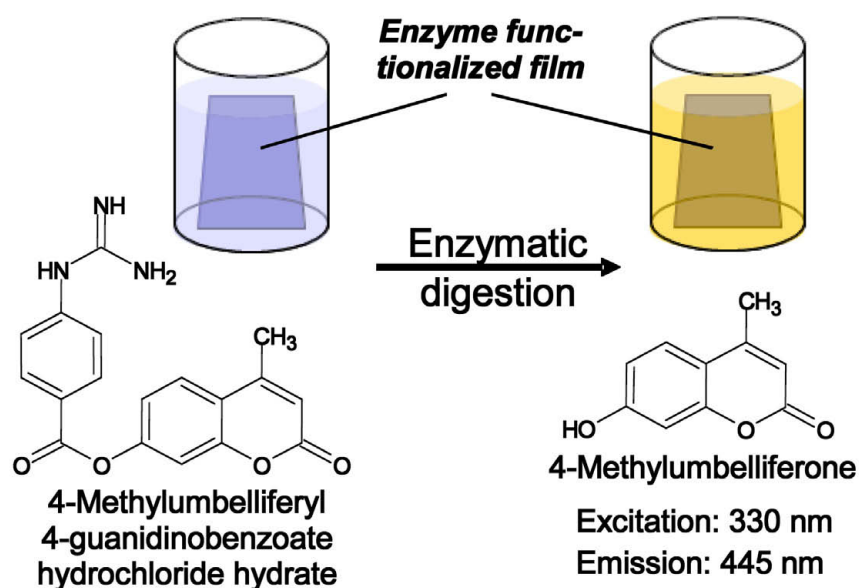


Figure 5.5: Procedure for enzyme activity measurements.

enough and so the activity of the encapsulated enzyme in the mesoporous films was studied by conversion of 4 methylumbelliferyl 4-guanidinobenzoate hydrochloride hydrate (MuGB) according to literature<sup>211</sup> (figure 5.5). 1  $\mu\text{l}$  of a 10 mM MuGB solution in pyrrolidinone was diluted with 1 ml  $10^{-3}$  M HCl. The film was placed in a polypropylene vessel with 20 g of PBS buffer solution (pH 7.4) and shaken at 150 rpm. 2  $\mu\text{l}$  of the MuGB solution were added. Every five to ten minutes 3 ml of the solution were transferred into a cuvette and the fluorescence at 445 nm was measured (excitation at 330 nm).

## 5.4 Results

The amount of enzyme bound to the mesoporous surface of sample B was estimated by comparing its activity to that of the free acetylene-functionalized trypsin. With dimensions of 15 mm x 28 mm x 130 nm (thickness measured by ellipsometry) the mesoporous layer volume is  $1.09 \times 10^{-4}$   $\text{cm}^3$ , and with an estimated density of  $1.3 \text{ g/cm}^3$  (also derived from ellipsometry) the film mass is about  $1.5 \times 10^{-4}$  g, because by dip-coating both sides of the silicon wafer are covered with mesoporous silica. The activity of sample B was compared with that of 1  $\mu\text{l}$  of the original sp-trypsin solution (figure 5.6a). The amount of free enzyme that would have the same activity as the mesoporous film is 0.455  $\mu\text{g}$ . From literature<sup>184</sup> it is known that the activity of the bound enzyme is only



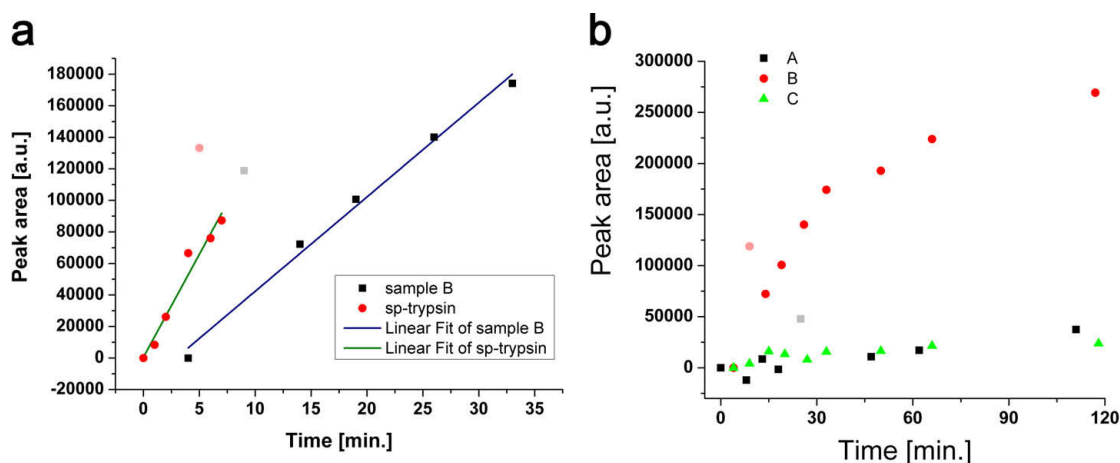


**Figure 5.6: Activity of trypsin functionalized mesoporous thin films.** **a** Comparing the activity of sample B with that of 1  $\mu\text{l}$  of the original sp-trypsin solution. The free enzyme is approximately twofold more active than sample B. (Two outliers are depicted in their corresponding pale colors and not included in the fit.) **b** Enzymatic activity of samples A, B and C. Peak area was calculated by integration from 390 nm to 550 nm. (Two outliers are depicted in their corresponding pale colors.)

about 20% the activity of free acetylene-functionalized trypsin, so the amount of bound enzyme can be estimated to be five times higher, namely 2.3  $\mu\text{g}$ , or approximately 1.5 weight percent of the film.

In order to prove the covalent bonding of trypsin samples B and C are compared. As  $\text{H}_2\text{O}_2$  destroys nearly all organic functionalities,<sup>210</sup> the enzymes in sample C could only be physically adsorbed. In addition, it is known that with increasing pore size the activity of trypsin on mesoporous materials is also increased.<sup>212</sup> Therefore, F127 was chosen as template, such that the resulting mesoporous films have rather large pores of approximately 8 nm in diameter and could, in principle, show a high activity. Nevertheless, the activity of sample C is far below the activity of sample B - almost at the detection limit (figure 5.6b). As the only differences between both samples are the missing linkers in sample C, this can only be explained with the successful linkage of trypsin molecules via Huisgen 1,3-dipolar cycloaddition in sample B, so that the functionalization density is higher and leaching is prevented.

Sample A represents a dense silica layer, hence a small surface area and a small amount of bound enzyme, which is reflected by the very low enzyme activity shown in figure 5.6b. The much higher activity of sample B demonstrates that trypsin is not only on the outer surface, but also bound to the pore walls within the mesoporous structure and still accessible for the MuGB molecules.

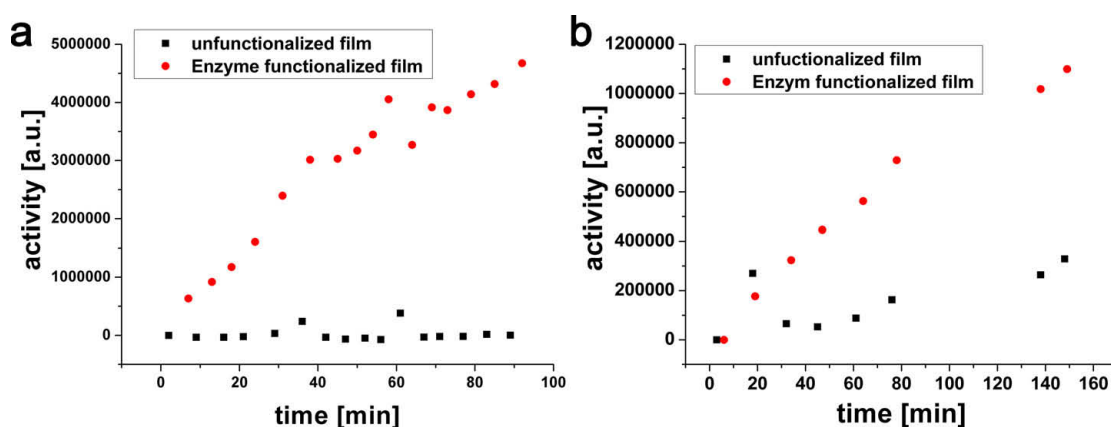


**Figure 5.7: Additional enzyme activity tests.** **a** The amount of  $1\ \mu\text{l}$  of a  $10\ \text{mM}$  MuGB solution in pyrrolidinone was diluted with  $1\ \text{ml}$   $10^{-3}\ \text{M}$  HCl. The films were placed in a polypropylene vessel with  $\sim 13\ \text{g}$  of PBS buffer solution (pH 7.4) and shaken at 150 rpm.  $2\ \mu\text{l}$  of the MuGB solution were added. Every five to ten minutes  $3\ \text{ml}$  of the solution were transferred into a cuvette and the fluorescence at 445 nm was measured (excitation at 330 nm). **b** The amount of  $1\ \mu\text{l}$  of a  $10\ \text{mM}$  MuGB solution in pyrrolidinone was diluted with  $1\ \text{ml}$   $10^{-3}\ \text{M}$  HCl. The films were placed in a polypropylene vessel with  $\sim 11\ \text{g}$  of PBS buffer solution (pH 7.4) and shaken at 150 rpm.  $1.6\ \mu\text{l}$  of the MuGB solution were added. Every five to ten minutes  $3\ \text{ml}$  of the solution were transferred into a cuvette and the fluorescence at 445 nm was measured (excitation at 330 nm).

Further activity measurements (see figure 5.7) in principle confirmed these results, but the activity differs by a factor of  $\sim 5$  indicating that the synthesis is not quite reproducible.

Nevertheless, 1.5 wt% enzyme is not a high loading and it would be desirable to increase this value, if such films should be applied in one of the fields mentioned at the beginning of this section. As in calcined films it was not possible to bind a detectable amount of enzyme (presumably due to the pore shrinkage normal to the substrate), we estimate that the size of trypsin with its hydration shell has just about the size of the pores in the template-extracted films. Because the pore diameter varies slightly, many pores are inherently too small and in addition some bigger pores can be blocked for further trypsin molecules, if there is already an enzyme bound. Possibilities to overcome these issues include the synthesis of films with larger pores and the usage of cubic frameworks with multiple interconnections between the pores.

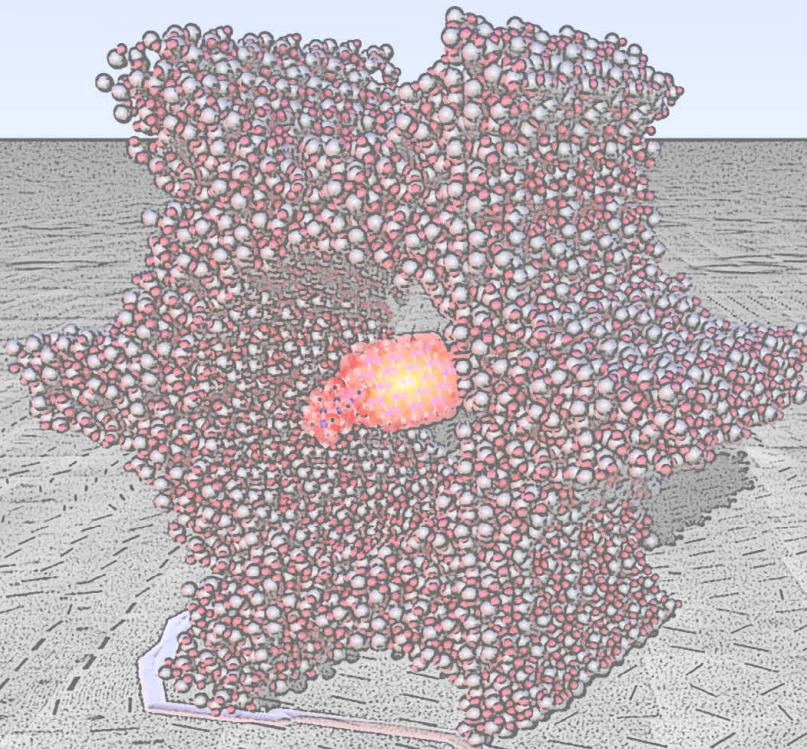
Up to now the activity of the enzyme-functionalized films decreases quite fast during re-usability tests, due to the degradation in PBS buffer solution. But calcined films, which are functionalized by grafting, are much more stable.

Also for this problem films with bigger pores may be a solution.

The synthesis of mesoporous silica thin films with covalently bound trypsin molecules was achieved by a click chemistry approach. The layers are much more active than samples produced by immobilization of enzymes due to physical adsorption. Moreover, the films are functionalized by a co-condensation procedure and extracted by organic solvents. Calcination and subsequent grafting is avoided and the incorporation of different linker groups is feasible in one step. This approach provides the bases for a direct correlation of enzyme activity and real mesoporous structure. Future experiments will have to deal with the decoration of the enzyme with TEM markers and fluorescent dyes.



# 6



INTRODUCTION

EXPERIMENTAL METHODS

**RESULTS AND DISCUSSION**

CONCLUSION

APPENDIX



## **6 Mesoporous thin films as sample systems for silica based drug delivery systems**

The main problem of cancer drugs is their high toxicity, which on the one hand is needed to kill cancer cells, but on the other hand also affects healthy cells as well. Actually, there are efforts to concentrate the drugs to specific areas in the human body, for example by magnetic effects.<sup>213</sup> But, healthy tissue is damaged or even destroyed all the same and in the case of metastasis these approaches are not applicable. Intelligent drug delivery systems aim to address this problem. These include nano spheres containing drug molecules in their interior and having proteins targeting the diseased cells on their outer surface. Studying diffusion in those systems by single molecule microscopy is quite difficult due to their small size, but would give valuable knowledge about drug uptake and release depending on the functionalization of the inner pore walls.

In this context mesoporous films are able to serve as sample systems, if they fulfill several conditions:

- Reasonable diffusion studies by SMM need a 2D hexagonal structure with domain sizes of at least several microns.
- Different functionalizations should be introduced, preferably two or more within the same film to simulate the nanoparticle systems.
- The template has to be removed and the pores should be accessible for molecules of the size of commonly used cancer drugs.

This section deals with the synthesis of mesoporous thin films matching all of these points.

### **6.1 Structure and pore size**

In order to get 2D hexagonal films with big pores ( $\sim 10$  nm in diameter or even more) Pluronic F127 was used as template (see also section 5) and the influence of the silica-to-surfactant ratio was investigated. The same tendency as in section 4.2 (lamellar  $\rightarrow$  2D hexagonal  $\rightarrow$  cubic, with decreasing template amount) could be observed and a silica to surfactant weight ratio of  $\sim 2$  (see table 10 in appendix) seemed to be suitable. It was also found that the relative humidity (r. h.) during dip coating is crucial, as well. Using the same synthesis

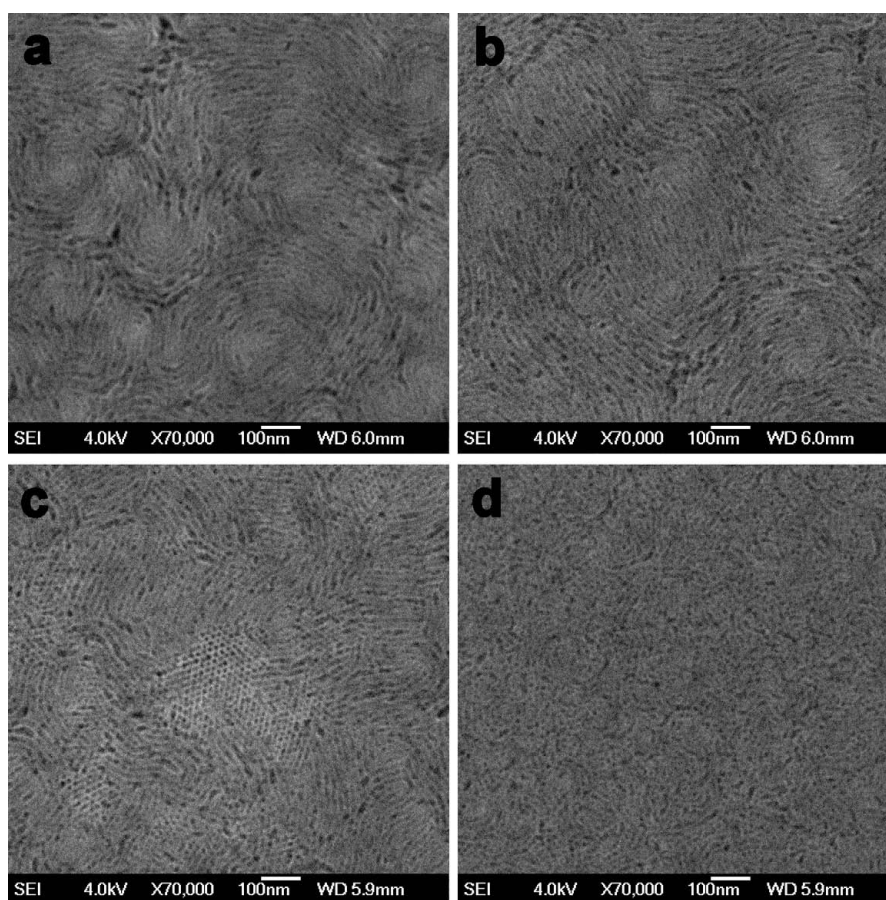


**Figure 6.1: Samples dip coated from one solution at different humidities.** In a drier atmosphere (**a** 7% r. h. and **b** 22% r. h.) predominantly a 2D hexagonal structure is formed. **c** At 50% r.h. isolated cubic domains appear. In addition, the domain size of 2D hexagonal ordered areas is reduced. **d** At 70% r.h. finally, the structured mesoporous ordering is lost. The resulting framework can be considered as worm-like.

solution a change from a predominant 2D hexagonal (up to 20% r. h.) to a more cubic (at ~50% r. h.) to a nearly worm-like (at ~70% r. h.) structure could be observed (see figure 6.1).

## 6.2 Functionalization and template removal

Functionalization is achieved by co-condensation allowing also the introduction of different species in one step. But with respect to the organic template compounds, removal has to be carried out under moderate conditions. Therefore, extraction is the method of choice. During first experiments with acetone



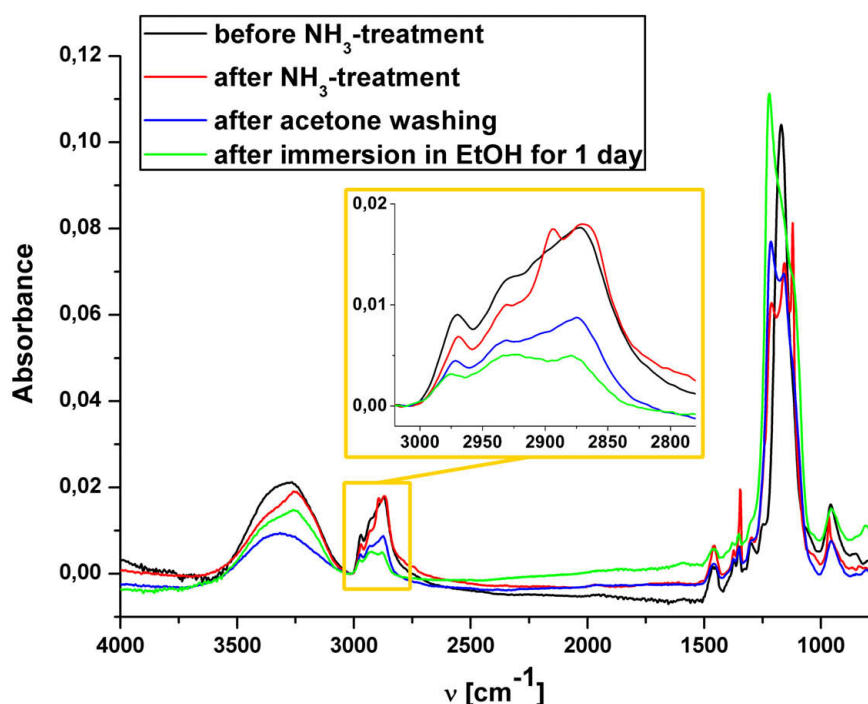


**Figure 6.2: RAIR spectra of a mesoporous thin film after each step during template removal.** Comparing the intensities of the C-H vibrations ( $\sim 2800 \text{ cm}^{-1}$  to  $3200 \text{ cm}^{-1}$ ) permits a rough estimate on the template amount. As expected, the ammonia treatment itself does not affect the template amount, but after acetone washing the intensities of the organic bands are drastically reduced to less than 50% comparing to the as-synthesized sample. A further decrease down to approximately 30% of the initial value is achieved by a subsequent storage of the film in spectroscopic ethanol. (Percentages calculated by integration of the IR intensities from  $2780 \text{ cm}^{-1}$  to  $3020 \text{ cm}^{-1}$ .)

the film was often washed away completely. As mainly the freshly synthesized samples didn't resist acetone washing, films were aged prior to extraction. Best results were obtained if the silica framework is stiffened by ammonia vapor. For this purpose the films are stored for 30 min in a closed container together with a small petri dish containing ammonia saturated water.

Template removal was investigated by RAIR (see figure 6.2). C-C and C-H vibrational bands are visible after ammonia treatment, but drastically reduced by acetone washing. Subsequent storage of the films in spectroscopic ethanol further decreases the organic bands. A complete removal is not achieved, probably due to template micelles fully enclosed by silica and therefore not accessible to solvents.

Thickness and XRD measurements accompanying this procedure revealed a

film thickness of about 100 nm for template extracted samples, but unveiled also another remarkable result. While the film thickness measured by ellipsometry or XRR is nearly unaffected by ammonia vapor treatment the XRD pattern shows a d-spacing decreased by about 20% (see table 7). The pore shrinkage most probably squeezes the template out of the pores on top of the film surface. This template layer would also explain the fact that in SEM structures of as synthesized and ammonia treated samples are not resolved. Only after template extraction both values - the thickness, as well as the d-spacing - exhibit the same shrinkage of approximately 30% and the structure is revealed by SEM.

Mesoporous sample	Thickness (by ellip- sometry)	Thickness (by XRR)	d-spacing (by XRD)
Ph, as-synthesized	144	157	11.6
Ph, ammonia treated	135	156	9.6
Ph, ammonia treated, extracted	90	107	8.0
CN, as-synthesized	142	159	11.5
CN, ammonia treated	139	158	9.2
CN, ammonia treated, extracted	99	119	8.7
SH, as-synthesized	155	190	11.0
SH, ammonia treated	149	155	8.5
SH, ammonia treated, extracted	86	—	7.3

**Table 7: Thickness and d-spacing of different functionalized films after distinct synthesis steps.** The mesoporous films functionalized with phenyl (Ph), cyanopropyl (CN) or mercaptopropyl (SH) were spin-coated from a solution containing the silica precursor, F127, HCl, EtOH and H<sub>2</sub>O in the following molar ratio 1.00 : 0.00828 : 0.00406 : 20.2 : 4.06. A 5% functionalization was obtained by co-condensation of TEOS with Phenyltriethoxysilane, (3-Cyanopropyl)triethoxysilane and (3-Mercaptopropyl)triethoxysilane, respectively (molar ratio 19:1). After ammonia treatment a shrinkage of the d-spacing is observed. A corresponding decrease of the thickness is only achieved with subsequent acetone washing.

### 6.3 Domain size

It was possible to retain the 2D-hexagonal structure up to 10% functionalization, but SEM measurements show that the domain sizes are too small for SMM and have to be enlarged. In the literature most studies aim to align the pores of the whole film using elaborate techniques. Yamauchi et al.<sup>214</sup> and

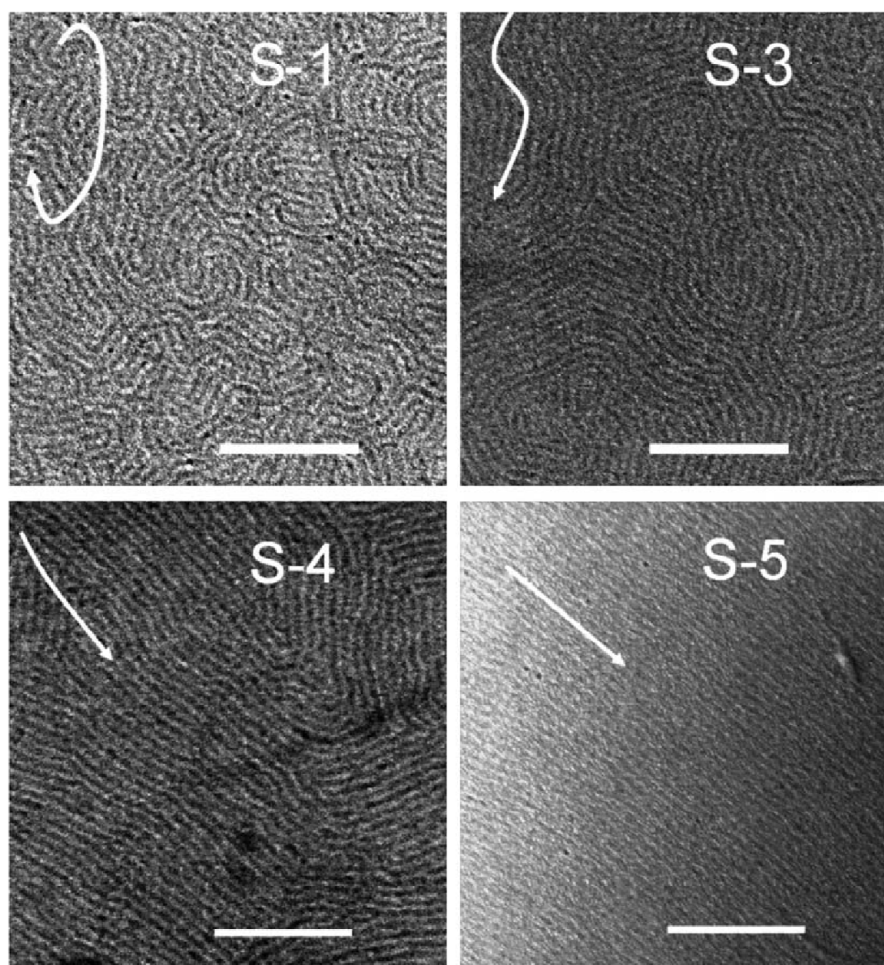


**Figure 6.3: FE-SEM images of the mesoporous silica films.**<sup>185</sup> S-1, S-3, S-4 and S-5, prepared at dip rates of 20, 2, 1, and 0.1 cm/min, respectively (the scale bar in the images equals 200 nm).

Tolbert et al.<sup>215</sup>, for example, applied a magnetic field of more than 10 tesla during casting and Miyata et al.<sup>216,217</sup> coated polyamide surfaces treated by rubbing. But, for single molecule microscopy an aligned domain of about five microns in length is enough to collect suitable trajectories for diffusion studies. Some parameters having influence on the domain size were investigated more closely and a method was developed in order to synthesize films with micrometer-sized domains in a reproducible manner.

The basic principle, as well as the composition of the synthesis solution were adopted from the literature.<sup>185</sup> In this paper film synthesis is carried out by dip coating under diverse conditions, inter alia, at different dip coating rates. At a dipping speed of less than 10 mm/min significant domain size enlargement is

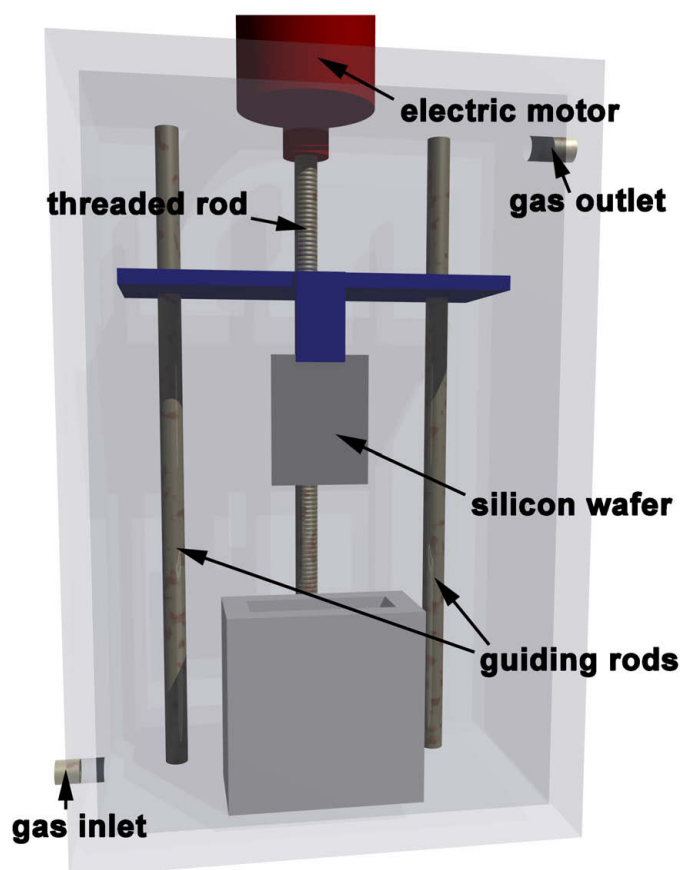


**Figure 6.4: Scheme of the dip coater manufactured by the university in-house precision engineering workshop.** Two guiding rods and one threaded rod actuated by an electric motor are built in an acrylic glass box in such a way that a sample stage can be lifted at different velocities. In addition, gas in- and outlets allow adjusting the atmosphere during dip coating.

visible (see figure 6.3). Very likely, a reduced dipping speed increases the time for pore arrangement leading to larger domains.

The dip coater used in our group was developed by the university in-house precision engineering workshop and consists of two guiding rods and one threaded rod actuated by an electric motor to lift and lower a sample stage at different velocities (see figure 6.4). The whole instrument is built into an acrylic glass box with gas in- and outlet to adjust the atmosphere during dip coating. The speed is adjusted by a potentiometer. Dipping rates below 0.5 mm/min were achieved and the reported tendency (bigger domains at lower speed) was observed.

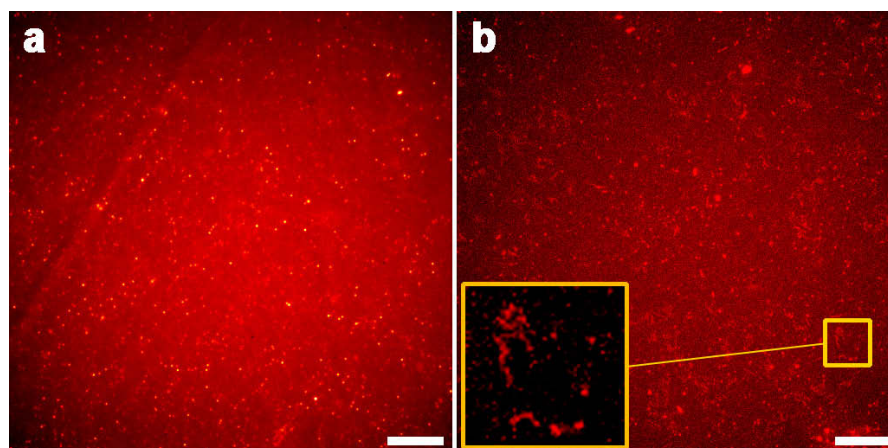


**Figure 6.5: Single molecule fluorescence microscopy images of mesoporous films loaded with TDI. a** TDI molecules in template free films are immobile. **b** In an EtOH saturated atmosphere most of the TDI molecules begin moving. The image represents a Z-Projection of a 200 frames movie showing the maxima values of each point over time. By this visualization method moving spots show up as thin traces in contrast to the individual bright points representing immobile molecules (see inset). Each scale bar represents 10  $\mu\text{m}$ .

## 6.4 Results

A reproducible synthesis of films with big domains was found for a dipping rate of 0.45 mm/min at a relative humidity of about 10%. The molar ratio of the coating solution is 1.00 TEOS : 0.00825 F127 : 39.7 EtOH : 8.09 H<sub>2</sub>O : 0.0205 HCl. Please refer to section 3.5 for more details on the synthesis.

After framework stiffening and template removal as previously described, the films could be loaded with a fluorescent dye by a simple spin-coating process. For this purpose 200  $\mu\text{l}$  of a  $10^{-8}$  molar solution of TDI (terrylene diimide) in EtOH was dropped onto the film surface to get a full coating, followed by spinning at 3000 rpm. At 100 $\times$  magnification single TDI molecules show up as bright immobile spots (see figure 6.5a).

The immobility is most probably due to attractive interactions between the TDI and the silica surface. Unlike in section 4 there is no template in which the TDI could move like in a solvent. But in an EtOH-saturated atmosphere at least a part of the TDI molecules begin moving. Apparently, EtOH adsorbs to the silica surface forming a sort of lubricating medium for the dye molecules. In contrast to the randomly moving spots representing molecules on top of the film surface and in unstructured regions, respectively, the molecules situated within the film pores stand out due to their oriented motion for- and backwards



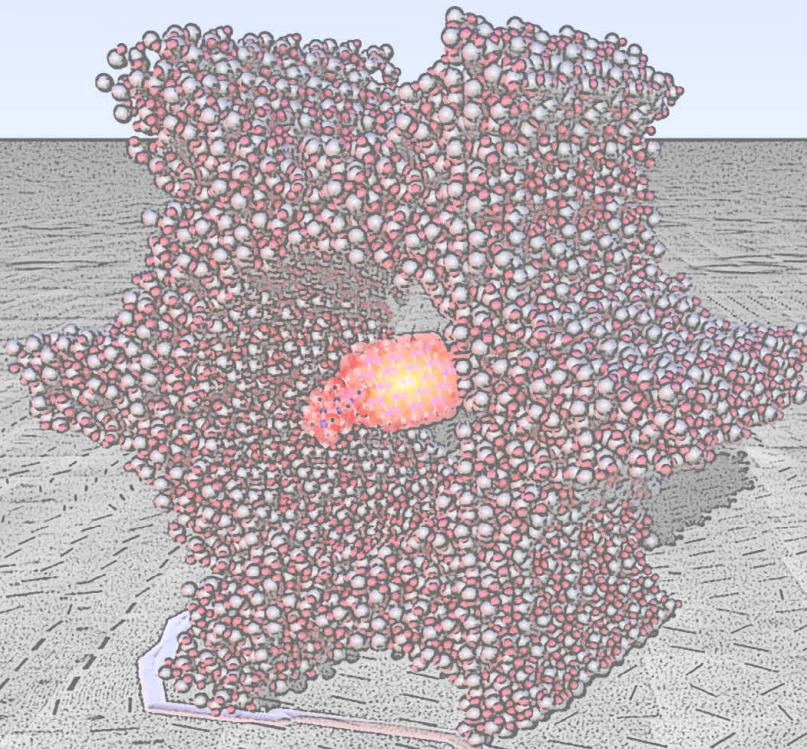
(see figure 6.5b and supplementary movie 4). Of course, an unambiguous distinction between unstructured and oriented movement has to be carried out by a more specific method, like single particle tracking. Then - according to section 4 - the oriented movement revealed by the trajectory of an individual molecule could be used to characterize its diffusion.

In conclusion, by using Pluronic F127 as template and dip coating at extremely slow dipping rates a reproducible synthesis for mesoporous thin films with big pores and large domains has been developed. Single molecule fluorescence measurements showed that these films can in principle serve as sample systems for diffusion studies. Nevertheless, more characterization is needed to better understand these systems and also the synthesis has to be adopted for functionalized films. Functionalization can be achieved through substitution of a part of the used TEOS by a functionalized silica source. By single particle tracking and the use of fluorescing drugs it should then be possible to study the influence of the functionalization on the diffusion behavior of the drug. These experiments would give useful information on drug uptake and release of colloidal mesoporous silica nano particles.





# 7



INTRODUCTION

EXPERIMENTAL METHODS

**RESULTS AND DISCUSSION**

CONCLUSION

APPENDIX



## 7 Visualizing nano scale objects by discrete tomography

The 3D structure of two particularly challenging samples was reconstructed by electron tomography. Due to sample limitations resulting in a large missing wedge and large tilt increments respectively the 3D structure could not be reconstructed by standard iterative algorithms; even a recently developed discrete algorithm failed until the input parameters for discrete reconstruction were improved. These challenges were addressed by adding a mask in each step of the preceding standard iterative reconstruction, setting all voxels known to be vacuum as zero, thus improving the segmentation and the 3D starting model. The position of these vacuum voxels is obtained from TEM images or other measurement data. The well-known free tomography software package TOM Toolbox was adopted and expanded by the above modifications including a new version of a discrete algorithm, thus succeeding in the 3D reconstruction of the samples.

In the field of materials science, electron tomography has developed rapidly in recent years with the emergence of various new techniques.<sup>218-222,89</sup> The increase of available methods has brought new potential insights in 3D structures through electron tomography, for example via added chemical or atomic number information. Most notably, Scanning Transmission Electron Microscopy (STEM) coupled with High-Angle Annular Dark Field (HAADF) or Annular Dark Field (ADF) imaging emerged to be a very useful method,<sup>140,223</sup> as most of the drawbacks of the 3D-TEM technique, like Fresnel diffraction and diffraction contrast, are overcome. In addition, STEM-HAADF is also chemically sensitive; it is able to resolve very small structures and does not suffer from phase contrast. Thus it enables the 3D structure and composition to be mapped simultaneously at high spatial resolution. However, as for many other non-conventional techniques in electron microscopy, issues of sample preparation and beam sensitivity have frequently become the limiting factor for obtaining high resolution data. In the case of electron tomography, one major limitation results from geometrical restrictions of the sample with respect to the tilt angle - the so-called missing wedge<sup>139,224</sup> - bringing about a blurring of the reconstructed objects along the beam direction at zero tilt. For example, for a tilt range of  $\pm 70^\circ$  the elongation for reconstructions with standard reconstruction techniques can be estimated to 30%,<sup>225</sup> therefore the angular range usually

is  $\pm 70^\circ$  or higher. The choice of the angular sampling rate can be another crucial factor limiting the resolution of the reconstruction<sup>224</sup>. Hence, small tilt increments of around  $2^\circ$  or less are commonly used for series acquisitions. As a consequence, the required number of images per series by far exceeds the maximum dose for many beam sensitive specimen. This problem can be overcome to a certain extent by using the imaging technique least prone to beam damage<sup>223,226,227</sup> or by adjusting the acceleration voltage<sup>228</sup> and the specimen temperature<sup>222</sup>. On the other hand, these measures may be unsuitable because of limited penetration depth in the case of lower acceleration voltages or sample drift under cryo-conditions, especially in STEM mode because of its long exposure times. FBP (Filtered Back Projection) and SIRT (Simultaneous Iterative Reconstruction Technique) are the most popular reconstruction methods in electron tomography. In both cases every TEM image is smeared back into object space along the original pathway (so-called backprojection), but only SIRT additionally reconciles the original projections with those calculated from the actual reconstruction and minimizes the differences in an iterative process. SIRT can be seen as a quadratic optimization method for solving a linear system of equations. Due to the fact that the function range is the set of real numbers it produces a blurring of the reconstructed objects, which affects the segmentation step after reconstruction.

If a sample consists of only a few different objects having different densities, discrete tomography can be used for the 3D reconstruction taking advantage of the reduced number of possible values in the reconstructed volume. Hence, the range of the function is a finite set of numbers. As a consequence of the drastic reduction of the number of potential solutions, high quality tomographic reconstructions can be obtained with significantly smaller data sets. For example, the sophisticated reconstruction algorithm proposed by Batenburg and Sijbers<sup>88</sup> was successfully applied to a reduced angular range, between  $-48^\circ$  and  $+74^\circ$  and to a reduced number of exposures of only 15 images.<sup>89</sup> It was noted that the assignment of gray scales is essential for the quality of the reconstruction and that sometimes the gray values had to be refined by a trial-and-error process.

In the following examples are presented showing tomographic reconstructions from series with even fewer exposures and smaller tilt ranges, respectively. These examples show how rather extreme acquisition parameters can still yield high quality results if additional information gained from experimental measurement data is included in the reconstruction process. Furthermore,



an unconventional image alignment procedure is presented since the common cross correlation and particle tracking failed due to the large angular increments of  $15^\circ$ . By combining these new techniques it is possible to visualize nano objects from projection series which by no means would result in suitable 3D images with conventional reconstruction techniques. We believe that our approaches can be easily applied to a broad spectrum of nanostructures and that they are especially useful for electron beam sensitive materials.

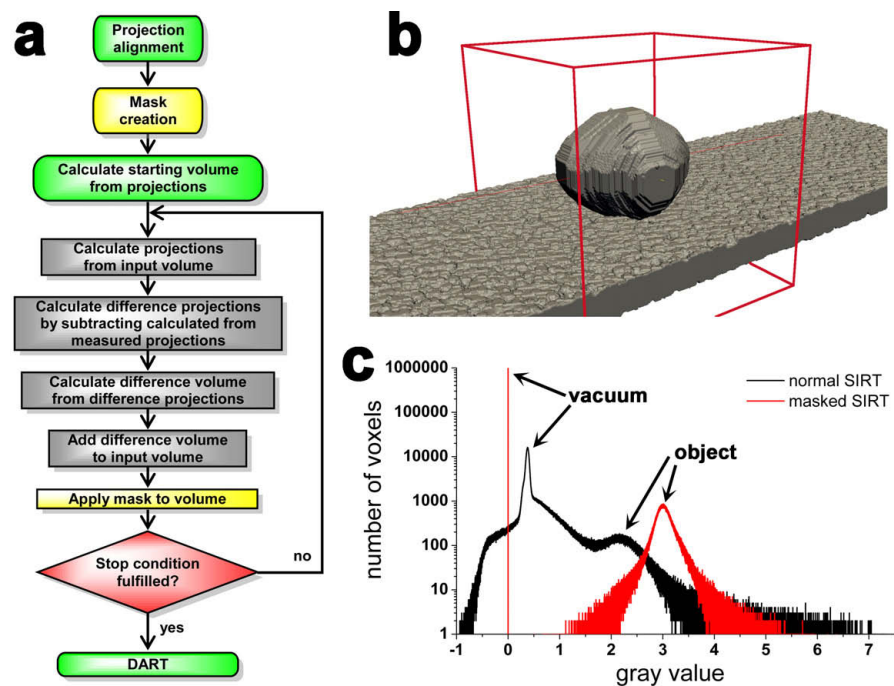


**Figure 7.1: Description of the masked SIRT process by means of a test object.** **a** Scheme of the modified SIRT algorithm including a masking step at the end of each SIRT iteration. During this procedure every voxel outside the mask is set to zero value, resulting in higher gray values for the voxels within the mask compared to commonly used SIRT algorithms. This is illustrated by the reconstruction of a test object **b** The test object consists of a particle lying on a thin membrane. Particle and membrane have the same gray value. Normal and masked SIRT reconstructions were calculated from nine projections of the test object ( $\pm 60^\circ$ ,  $15^\circ$  steps). Histograms of the volume enclosed by the red cube ( $256 \times 256 \times 256$  voxel) of both reconstructions are depicted in **c**. The object gray value is shifted from approximately 2.2 after normal SIRT reconstruction to the correct value (3.0) if the masked SIRT method is used. (For the number of pixels a logarithmic scale was chosen.)

### 7.1 Masked SIRT algorithm

In order to perform discrete tomography the recently developed algorithm by Batenburg and Sijbers<sup>88</sup> (Discrete Algebraic Reconstruction Technique, DART) was integrated into the well-known free tomography reconstruction package TOM toolbox.<sup>229</sup> DART uses as input an estimate of different grayscales corresponding to different compositions of the specimen. These values are determined from an initial SIRT reconstruction and the segmentation procedure is performed automatically during reconstruction. Due to the fact that SIRT tends to distribute intensities to a bigger volume, these gray values are always underestimated (e.g., Batenburg et al.<sup>89</sup> report that the gray value for a gold nanoparticle had to be refined by a trial-and-error procedure). Often, the underestimated gray values are attributed to poor-quality SIRT reconstructions, obtained from only a few projections or from a small tilt range. Hence, calculating a SIRT starting volume as realistic as possible is essential for a successful DART reconstruction.

For this reason, the initial SIRT reconstruction was modified by an additional “masking” step (see figure 7.1a). The mask is an approximation of the real object volume obtained from real measurement data. In each SIRT iteration step all voxels outside the mask will be set to zero. As a consequence, the intensity a normal SIRT reconstruction would have scattered over “vacuum voxels” is now added to the object’s voxels and increases their gray value. The reconstruction procedure is illustrated by a test object consisting of an oval particle lying on a thin membrane as shown in figure 7.1b. Particle and membrane were assigned the same gray value of 3.0. Normal and masked SIRT reconstructions were calculated from nine projections of the test object ( $\pm 60^\circ$ ,  $15^\circ$  steps). The normal SIRT reconstruction resulted in a histogram showing a broad peak lying considerably below the assigned voxel value for object and membrane. In contrast, the histogram from the masked SIRT reconstruction shows a pronounced peak at the correct gray value of the particle (see figure 7.1c).

### 7.2 Alignment using the “barycenter”

Large angular increments often prevent standard image alignment by cross correlation or by tracking of heavy metal nanoclusters because of the large positional changes. In the case of nearly spherical particles the alignment shifts can be calculated by integration in both dimensions of each background cor-

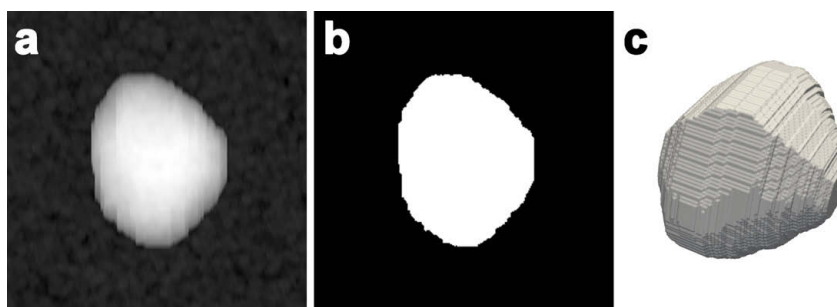


**Figure 7.2: Mask set-up for an individual particle.** **a** Projection of the test object at  $0^\circ$  ( $256 \times 256$  pixels). **b** Binary projection setting all values lower than the mean value to zero and all other values to one ( $256 \times 256$  pixel). **c**. Mask calculated from binary projections ( $256 \times 256 \times 256$  voxels).

rected projection and fitting a Gauss function to these data. The positions obtained by Gauss fitting represent the projected “barycenter” which is centered by shifting the projection.

### 7.3 Setting up the mask

According to different types of samples two procedures for creating masks were developed.

#### 7.3.1 Individual particles

For the reconstruction of individual particles a mask is calculated by subtracting the mean value from all projections, setting positive values to one and negative values to zero (see figure 7.2a,b). Afterwards, a volume is reconstructed with these “black and white” projections using one simple backprojection step. Every voxel encountering a zero value at least once during the back-projections is defined as vacuum. The remaining voxels are a rough approximation of the nanoparticle’s shape (see figure 7.2c).

#### 7.3.2 Continuous membranes and metal layers

The shape, position and thickness of continuous membranes or metal layers perpendicular to the  $0^\circ$  viewing direction cannot be determined from projections, especially at small tilt angles. However, small particles and defects on their upper and lower surface show up in reconstructions as brighter and darker spots, respectively. The localization of these spots is simplified if a thin volume of the standard SIRT reconstruction perpendicular to the tilt axis is

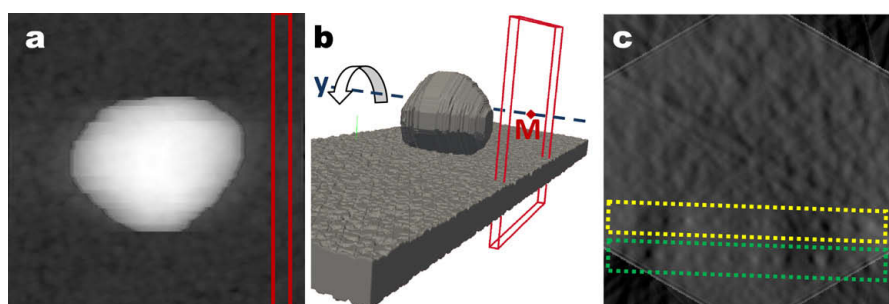


**Figure 7.3: Mask set-up for continuous membranes and metal layers.** **a** To determine a mask for a continuous membrane, a thin volume of the standard SIRT reconstruction was chosen (red box,  $256 \times 10 \times 256$  voxel). **b** The volume only contains the membrane and is centered on the tilt axis ( $y$ ). This volume is integrated along the  $y$  axis to reveal particles on the upper and lower surface of the membrane. This procedure is repeated with other volumes and the coordinates of the particles/defects are noted. To these data two planes are fitted representing the boundary of the membrane. **c**. Grayscale image ( $256 \times 256$  pixel) of the integrated volume from **a** showing defects/particles on the upper (yellow dotted box) and lower (green dotted box) side of the membrane.

integrated in the direction of the tilt axis (see also figure 7.3). Applying this technique to different volumes gives two sets of data points - one for the upper and one for the lower surface. The mask is generated by fitting planes to these points.

## 7.4 DART

The SIRT volume calculated by applying the mask after each iteration step is used as initial reconstruction for DART, which of course is then applied to the whole volume without the use of a mask. In principle, the DART algorithm also performs SIRT iterations, but it has an embedded segmentation step and applies SIRT only to boundary voxels. Segmentation parameters are either obtained from other measurement data combined with information provided by the projections or from the histogram of the starting volume as obtained by masked SIRT.

In the following the potential of this technique is demonstrated by means of three tilt series - one consisting of only 9 projections and the others having an angular range of only  $\pm 40^\circ$ . Commonly used reconstruction techniques, like SIRT, were not able to produce high quality reconstructions from these tilt series, neither was DART successful without prior modification to the initial SIRT.

## 7.5 Colloidal Mesoporous Silica Nanoparticle

Among many other potential applications,<sup>230</sup> colloidal mesoporous silica (CMS) nanoparticles can be used as hosts for drug delivery systems.<sup>66</sup> To maximize the drug uptake inside the particles and to graft gatekeeper molecules at the outer pore mouth for controlled release, the inner and the outer surface of the particles require specific functionalizations. These site-selective functionalizations can be visualized in STEM-ADF after specific staining with metal clusters or heavy atoms of the functional groups located in the CMS nanoparticle volume.<sup>231</sup>

Inner thiol-functionalized CMS nanoparticles (CMS-SH<sub>IN</sub>) were synthesized following a delayed co-condensation approach.<sup>232</sup> The nanoparticles are about 50 nm in diameter.

### 7.5.1 Acquisition and projection pre-processing

For image acquisition a FEI Titan 80-300 operating at 300 kV and equipped with a Fischione tomography holder was used at tilt angles between 60° and -60°. To maximize the signal-to-noise ratio at a minimum dose, we used STEM-ADF conditions at a detector inner diameter of 26 mrad and a beam convergence angle of 19 mrad. However, there was no indication for effects of diffraction contrast, which can be attributed to the small size and possibly multiple twinning of the gold particles. The whole tilt range was cycled three times decreasing the tilting step in each run by 5° using 15° in the beginning. As a result of the synthesis procedure which does not employ calcination, the CMS nanoparticles exhibit a considerable tendency to shrinkage under the electron beam, thus prohibiting standard procedures for the tilt series recording at high magnifications. To minimize beam damage, the sample was left for 30 min in an ammonia-saturated atmosphere, as ammonia is able to further stabilize the CMS framework<sup>170</sup>. However shrinkage is not avoided completely as shown in figure 7.4. The projections at 0° were used to determine alteration and shrinkage of the CMS nanoparticles, which can invalidate the reconstruction. Shrinkage of about 2% is observed after 14 excitations, after 22 additional images this value is doubled.

In order to minimize the influence of shrinkage and alteration the first tilt series with projections at -60°, -45°, -30°, -15°, 0°, 15°, 30°, 45° and 60° was chosen for reconstruction. As described in the methods section, the background-corrected projections were aligned by centering the computed “barycenter” and



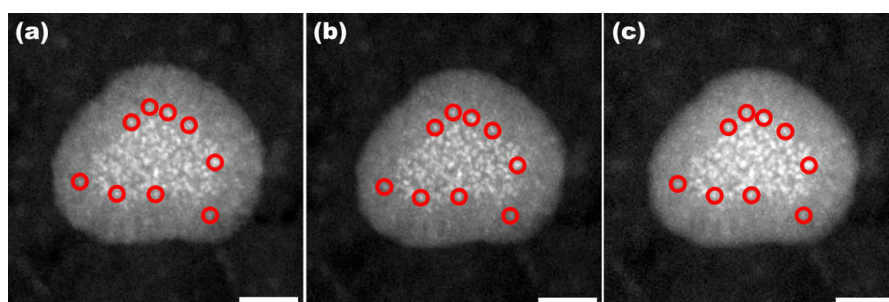


**Figure 7.4: Mask set-up for continuous membranes and metal layers.** During image acquisition shrinkage of the CMS nanoparticle occurs. A quantitative analysis is performed by evaluating the positions of different gold clusters (red circles) in the  $0^\circ$  projection (a). Shrinkage is calculated to 2% after 14 (b) and 4% after 36 (c) images, respectively. Alteration is hardly identified, but it seems that the porous structure is affected by the electron beam. All scale bars 20 nm.

the mask was generated following the procedure for single particles. However, as the carbon film thickness varies, the background correction (subtraction of a single value) leads to projections which still contain some intensity from the carbon film at distinct positions. For this reason and because the scattering powers of carbon and silicon dioxide are too similar, a thin layer corresponding to the carbon film was added. Its position and shape was determined as described in section 7.3 for continuous membranes, so that these intensities can also be reconstructed and do not cause artifacts.

### 7.5.2 Comparing original and DART projections

By setting vacuum voxels to zero during reconstruction the maximum for the silica gray value in the histogram (see figure 7.5) is shifted from approximately 2.65 for standard SIRT to 3.7 for masked SIRT reconstruction. A clear maximum for the gray value of gold could not be determined in either histogram. The segmentation within the DART algorithm sets all gray values below 1.85 to zero and every value from 1.85 to 7.4 to 3.7. Values above 7.4 are not segmented. This is not a rigorous DART approach, but in our view it works better than using an arbitrary value for gold. The result is a sort of envelope confining the peak open volume of gold. Outside the volume there is definitively no gold to encounter.

From the histogram of the masked SIRT reconstructed volume, the segmentation parameters were obtained and by applying the DART algorithm an improved 3D reconstruction with strongly reduced artefacts and a clear distinc-

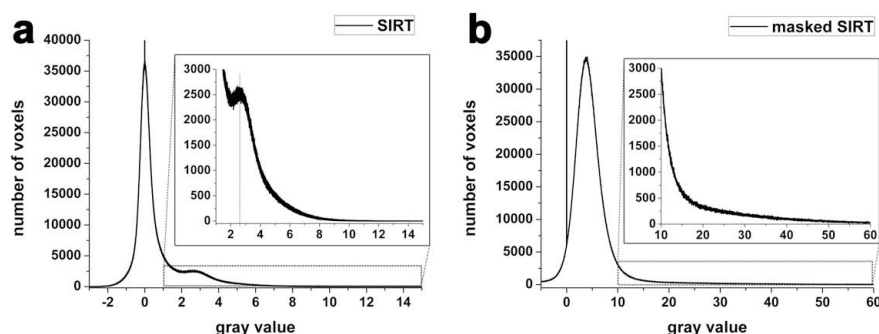


**Figure 7.5: Histograms of standard and masked SIRT reconstruction.** **a** Histogram of the standard SIRT reconstructed volume. The small shoulder at approximately 2.5 can be assigned to silica. Most of the voxels have a gray value in the range of  $\pm 1$ . A decision whether these voxels are vacuum or silica is quite difficult. Gray values for gold could not be identified. **b** Histogram of the masked SIRT reconstruction. Beside the highest intensity at a gray value of 0 – due to masking – another local maximum is visible at 3.7 attributed to silica. However, a gray value for gold is not noticeable.

tion between CMS and gold nanoclusters was obtained. Figure 7.6a depicts a cut through the DART reconstructed volume of the CMS nanoparticle, clearly showing the silica (gray) and the gold nanoclusters (white). In comparison, figure 7.6b shows the same cut through a volume calculated by a commonly used SIRT algorithm. Here, a clear distinction between the CMS and gold is not possible. Due to the artifacts caused by the strong scattering of the gold clusters, it is even challenging to roughly estimate the particle's shape. An exact determination of gray values is not possible. Finally, the same cut through a volume calculated from a masked SIRT algorithm is shown in figure 7.6c. The gold nanoparticles stand out more clearly and the intensity distribution within the CMS is more homogeneous.

Figure 7.7 shows the original STEM images of the CMS nanoparticle at  $0^\circ$ ,  $+45^\circ$  and  $-45^\circ$  (figures 7.7a,c,e) compared to the corresponding projections (figures 7.7b,d,f) calculated from the DART reconstructed volume. The slight smoothing visible can result from improper alignment shifts, as well as unsharp projections. However it is worth to note that these projections are very similar to the original projections, thus suggesting a satisfactory reconstruction by the DART algorithm.

To obtain a value for reconstruction quality, the standard deviation (STD) of each difference projection (calculated projections minus original images) were determined. In order to rank these values, two additional DART reconstruc-

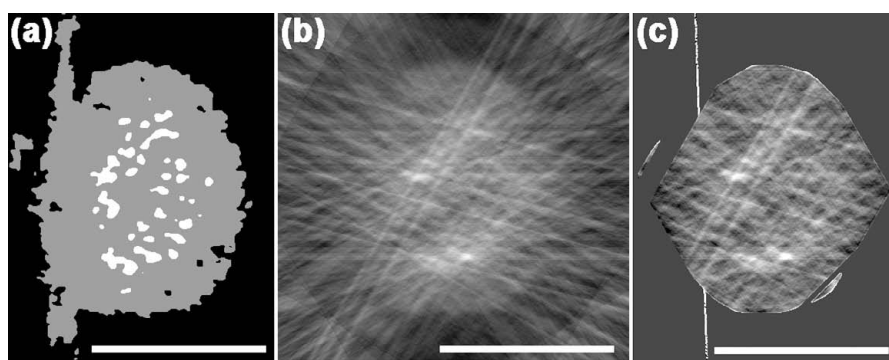


**Figure 7.6: Cuts through different reconstructed volumes of the CMS nanoparticle.** **a** 3D reconstruction of the CMS-SH<sub>IN</sub> sample with gold clusters in the inner core of the CMS nanoparticle after applying the DART algorithm (193 iterations). A defined volume is obtained, showing no artifact and a clear distinction between CMS (in gray) and the gold (white spots). The carbon substrate was reconstructed as well. The rotation axis is perpendicular to the drawing plane. **b** The image displays the same single cut through a volume reconstructed from 100 conventional SIRT iterations. No clear distinction between CMS and gold is visible and a lot of artifacts are present. **c** The same cut taken from the masked SIRT algorithm. The gold nanoparticles stand out more clearly. All scale bars 50 nm.

tions using standard SIRT reconstructions as starting volumes were performed and evaluated the same way (see table 8).

The rendered 3D volumes (created in Amira 5, Visage Imaging) of the CMS sample with the reconstructed gold nanoclusters are shown in figure 7.8 and in the supplementary movies 5 and 6 on the CD. The spatial distribution of the gold nanoclusters (in yellow) within the core of the mesoporous CMS nanoparticle (in gray) was reconstructed through the DART algorithm. An exact gray value for gold could not be determined from the initial SIRT reconstruction because the nanoclusters are only several voxels in size and hence strongly affected by blurring. As a consequence, these voxels were not segmented and therefore the space assigned to gold can be interpreted as the maximum open volume of gold. It was not possible to resolve the pores of the CMS nanoparticle. Due to the lack of pores in the starting volume there are no corresponding boundary pixels as starting points for the DART algorithm for pore refinement. Therefore, the CMS gray value determined is rather a mean value of CMS and vacuum resulting in a “dense” particle. Reconstructions with higher CMS gray values (according to an estimated porosity of 50%) do not yield a reliable volume either, probably because the starting volume is insufficiently structured.

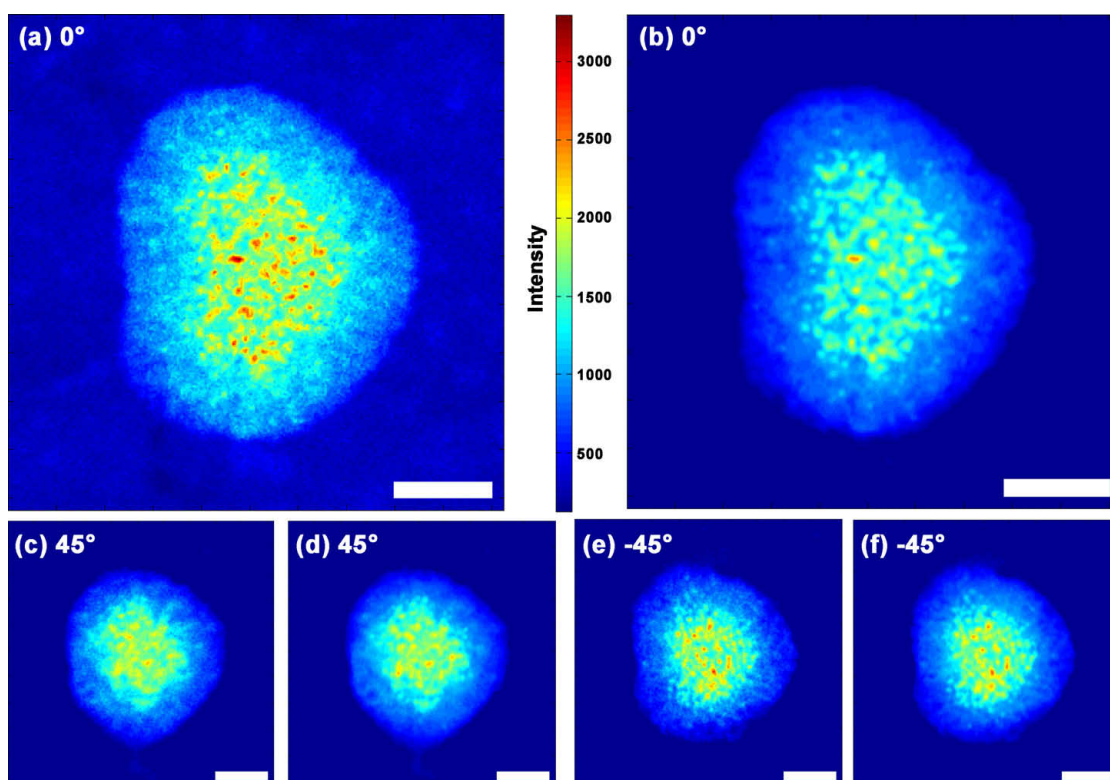


**Figure 7.7: Comparison of original STEM images and DART calculated projections of the CMS nanoparticle.** STEM images at **a**  $0^\circ$ , **c**  $+45^\circ$  and **e**  $-45^\circ$  of the inner thiol-functionalized CMS nanoparticle, showing the gold nanoclusters confined into the inner core. Calculated projections at **b**  $0^\circ$ , **d**  $+45^\circ$  and **f**  $-45^\circ$  were obtained from the reconstructed volume through the DART. All scale bars 20 nm.

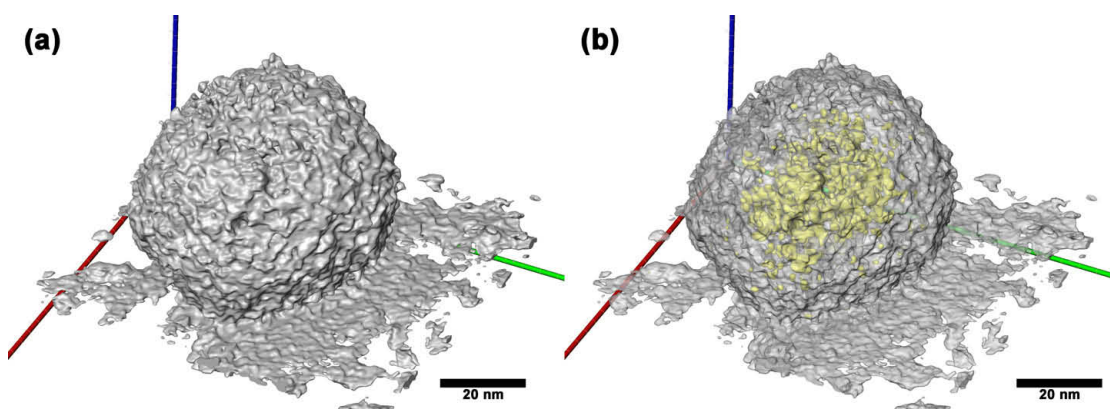


**Figure 7.8: Rendered 3D volumes of the DART reconstructed CMS sample.** **a** Final rendered 3D reconstruction of the CMS nanoparticle lying on the carbon grid. **b** Reconstructed volume with semi-transparent CMS material (gray) and the gold nanoclusters (yellow) immobilized in the inner core of the nanoparticle.

Angle	Masked SIRT (segmentation: 3.7/7.4/14.8)	Standard SIRT (segmentation: 3.7/7.4/14.8)	Standard SIRT (segmentation: 2.65/5.3/10.6)
-60°	70.3	107.3	95.3
-45°	51.6	77.2	73.5
-30°	60.5	86.3	82.9
-15°	50.1	79.8	71.7
0°	57.2	93.3	84.1
15°	60.8	90.3	82.0
30°	57.5	81.8	80.4
45°	43.1	66.2	61.0
60°	62.0	100.5	94.7
sum	513.1	782.7	725.6

Slice cut out of reconstructed volume at y=128

**Table 8:** Standard deviations (STD) of difference projections obtained by subtracting original STEM images from the corresponding projections calculated from reconstructed volumes. The DART volume used in column 1 was obtained using a masked SIRT reconstruction as starting volume. Segmentation was performed setting all values between 3.7 and 14.8 to 7.4, smaller values are assigned as 0, and bigger values are not segmented. Column 2 shows the STD values using the same segmentation, but standard SIRT as starting volume. The higher values indicate a lower reconstruction quality. Changing the segmentation parameters (column 3) according to the histogram in figure 7.5a results in better STD values, but at the cost of a strongly enlarged gold volume (see last row), thus a loss of resolution. (Original STEM images for these reconstructions were binned one time. Therefore, the segmentation parameters are doubled in comparison to the histogram of figure 7.5. All scale bars 20 nm.)



## 7.6 Nanopore in a silicon nitride membrane

Single nanometer-sized holes in otherwise impervious membranes constitute simple devices to analyze single molecules: when biological macromolecules like DNA or proteins traverse the pore from one side of the membrane to the other, a characteristic signature can be observed in the trans-pore ionic current.<sup>233</sup> One possibility to produce such pores is a combination of photolithography, e-beam lithography, reactive ion etching and wet chemical etching. By application to silicon nitride-coated silicon wafers, this procedure results in free-standing silicon nitride (SiN) nanopores with a diameter of several ten nanometers and a height of 50 nm.<sup>234</sup> The pores were metalized by subsequent physical vapor deposition.

### 7.6.1 Image acquisition

(S)TEM tomography was performed using a FEI Titan 80-300 on an unmetalized and a metalized nanopore and single-axis tilt series were recorded consisting of 43 TEM images from  $-41^\circ$  to  $+41^\circ$  and of 40 STEM-HAADF images from  $-36^\circ$  to  $+42^\circ$ , respectively. The maximum tilt angle was limited as a consequence of the silicon fringes casting a shadow on the SiN membrane.<sup>234</sup> As the SiN membrane is amorphous, it does not produce any diffraction contrast. Fresnel contrast was reduced by keeping the defocus to a value close to zero and by using an objective aperture cutting spatial frequencies beyond  $0.23 \text{ nm}^{-1}$ . Hence, TEM images of the pore are governed by mass-thickness contrast and can therefore be used for reconstruction with DART. As far as known, this is the first example for a successful application of DART on a TEM tilt series.

To visualize the shape of the metalized nanopore with a 20 nm thick Au film, STEM in HAADF mode with a beam convergence angle of 19 mrad was used. To minimize contributions of diffraction from the thick gold film, the camera length was set to 77 mm corresponding to a detector inner diameter of 160 mrad. Due to the large difference in atomic numbers between gold and SiN, only the evaporated gold film but not the SiN membrane is visible in the tomographic reconstruction.

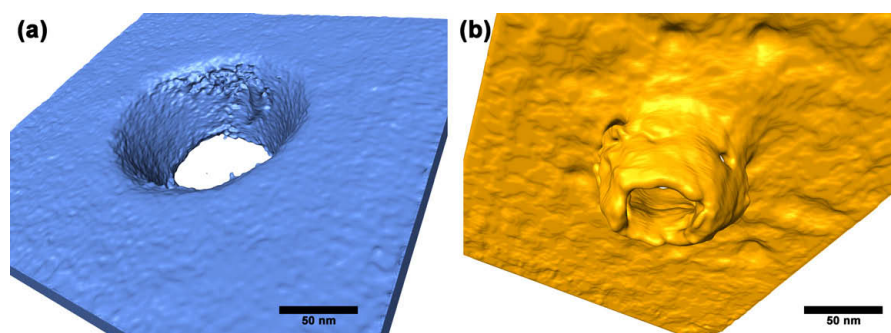


**Figure 7.9: Rendered 3D volumes of the DART reconstructed nanopore samples. a** Final rendered 3D reconstruction of the uncoated SiN-nanopore. **b** Reconstructed volume of a 20 nm thick gold layer on top of a SiN-nanopore. As gold is a much stronger electron scatterer, the SiN membrane itself could not be reconstructed.

### 7.6.2 Mask set-up and DART reconstruction

The projections of each series were aligned by cross correlation (Inspect 3D software, FEI) and background corrected by subtracting an average vacuum pixel value. An initial SIRT reconstruction with at least 20 iterations for each series was performed to coarsely determine the membrane position and thickness by localization of defects and particles on its upper and lower surface (see section 7.3). Afterwards data masks were created and applied in a second SIRT reconstruction. Segmentation parameters were calculated from the membrane thickness and a mean intensity value for the membrane was obtained from the  $0^\circ$  projection. DART reconstruction was performed including at least 50 iterations. Visualization of the resulting 3D data was carried out with Amira 5 (Visage Imaging) by surface rendering, see figure 7.9 and supplementary movies 7 and 8 on the CD.

### 7.6.3 Comparing DART reconstructions derived from different SIRT starting volumes

According to section 7.5.2 the STD values of DART reconstructions derived from standard SIRT and masked SIRT starting volumes were determined and then plotted against the projection angle (see figure 7.10). The masked SIRT approach results in much smaller STD values, thus higher quality reconstructions. Especially at large tilt angles the standard SIRT approach tends towards higher STD values.

A comparison of DART reconstructions of the metalized pore for unmasked and masked SIRT starting volumes is shown in figure 7.11. In both cases the

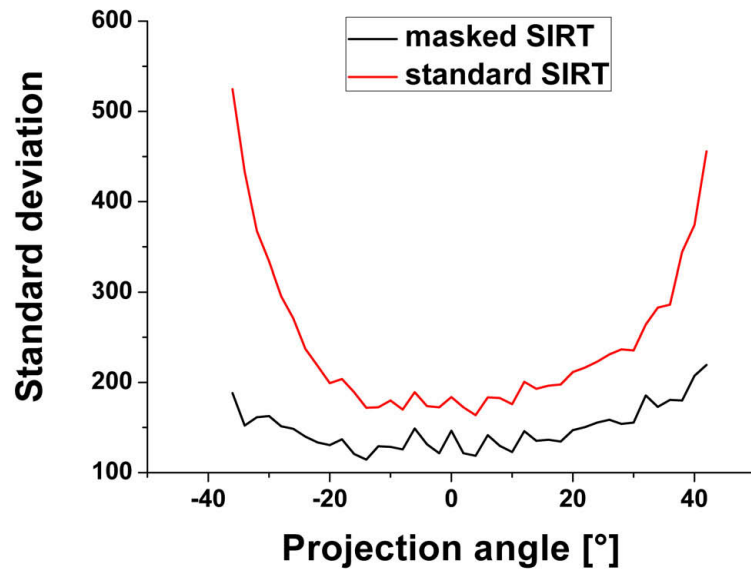


**Figure 7.10: Quality of DART reconstruction.** Standard deviation of the difference projections calculated from DART reconstructions using standard SIRT and masked SIRT, respectively, as starting volume. Standard SIRT leads to higher standard deviation values especially at large tilt angles.

same numbers of SIRT and DART iterations were used, as well as the same segmentation parameters. By using standard SIRT to calculate a starting volume finally a dubiously rough gold layer with holes and cracks was obtained. The masked SIRT approach results in a much smoother gold layer without defects. Comparing projections at  $+30^\circ$  and  $-30^\circ$  calculated from both reconstructions (figures 7.11c-d and figures 7.11g-h, respectively) to the original STEM images (figures 7.11e-f) indicate a more accurate result by using masked SIRT. A slight variation of the material's gray value results in shrinkage/stretching of the gold/SiN volume, but its respective shape is retained. Excessively high gray values lead to holes within the reconstruction.

## 7.7 Results

In the examples presented here, the use of DART is the precondition for high quality 3D reconstructions. However, for the extreme restrictions on tilt series parameters as encountered in these samples, additional information had to be included during reconstruction. The recently developed DART algorithm from Batenburg et al. was adopted as it stands, but masked SIRT iterations

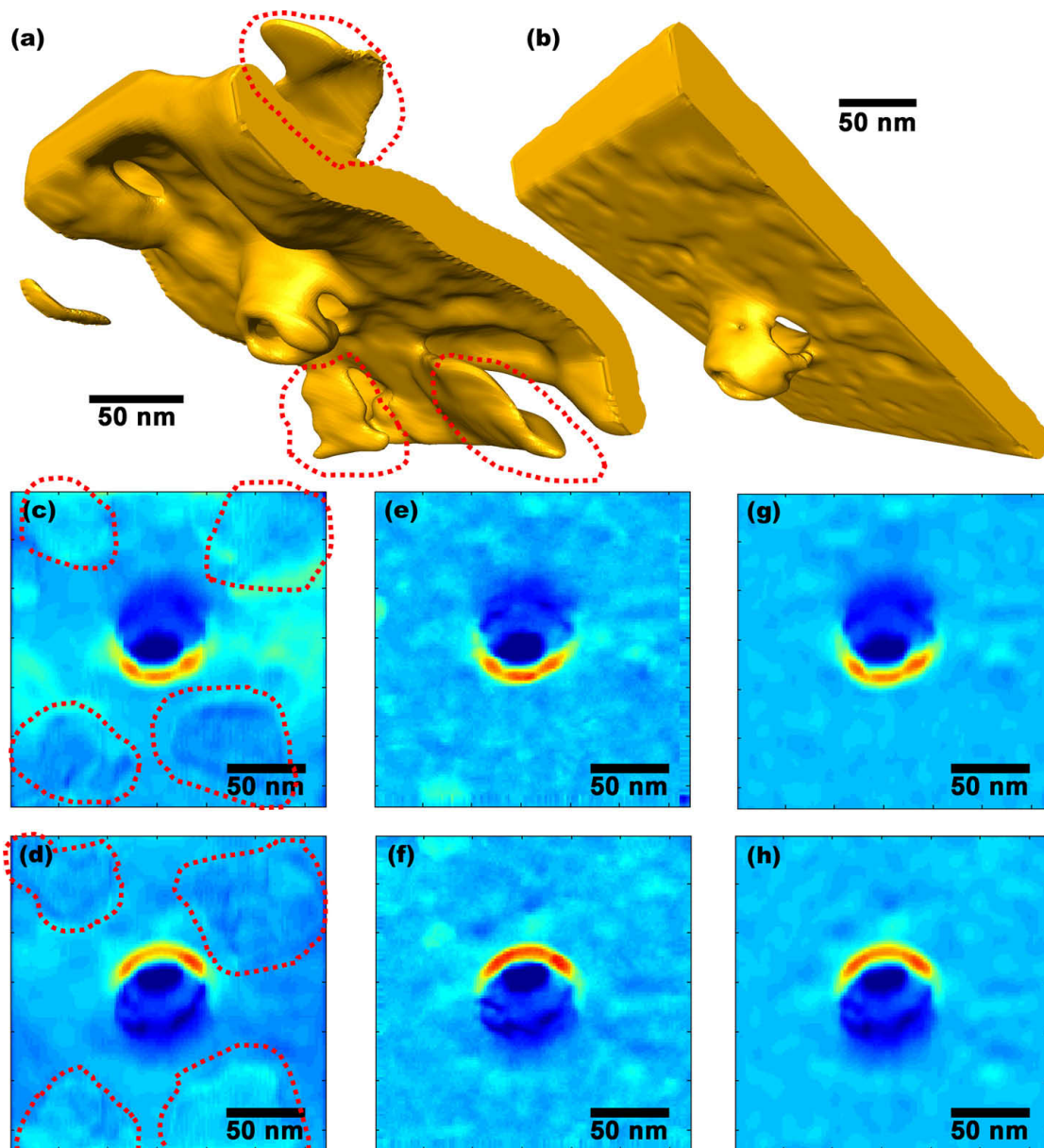
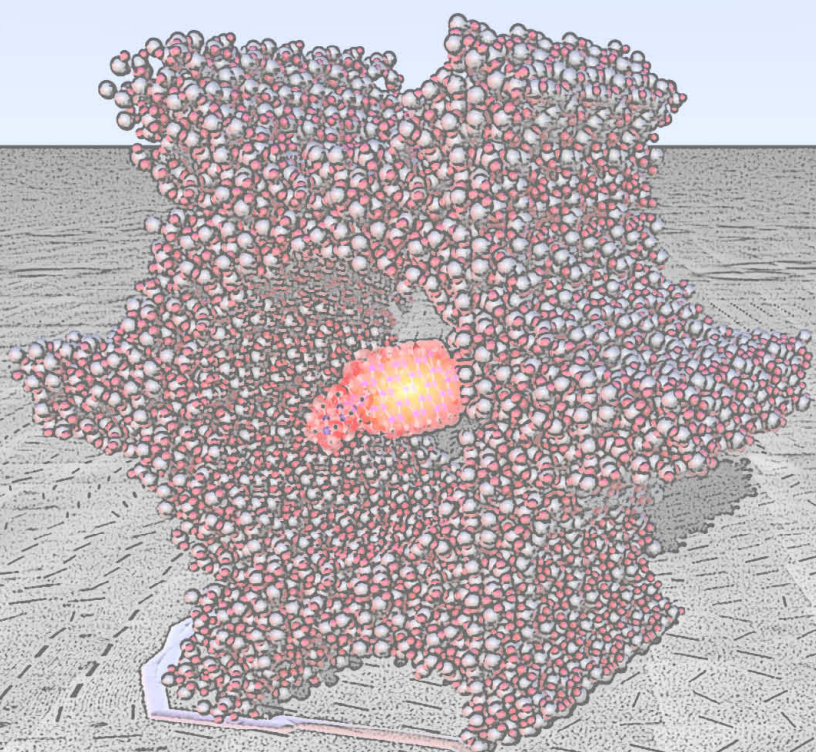


**Figure 7.11: 3D reconstructions (128 voxels edge length) of the gold pore rendered in Amira 5.1 (Visage Imaging).** **a** DART reconstruction using a start volume obtained from standard SIRT. The gold layer is extremely bumpy and holes as well as cracks are clearly visible. **b** The same pore reconstructed with DART using a starting volume obtained from a masked SIRT algorithm. In addition to the smooth gold layer showing no defects, it is remarkable that also the pore shape itself has changed in comparison to **a**. **c,d** Two projections calculated from (a) at  $-30^\circ$  and  $+30^\circ$ . **e,f** Original STEM images recorded at  $-30^\circ$  and  $+30^\circ$ . The wing-like artifacts visible in (**a**, **c** and **d**, outlined in red) do not show up. **g,h** The same projections calculated from **b**.

were used to get a more accurate starting volume from which, compared to standard SIRT, more accurate gray values were determined. Masking automatically sets vacuum voxels to zero intensity, such that the whole projection intensity is distributed to the object intended for reconstruction. Discrimination of vacuum and object voxels is carried out by the use of real measurement data. The masking step is straightforward and it provides a successful practical approach to the segmentation problem in discrete tomography. With the masking approach the distribution of metal nanoclusters in the mesoporous structure of colloidal silica nanoparticles could be resolved and high quality reconstructions were obtained. The problems related to the high fragility and shrinkage of this non-thermally treated sample are largely overcome by applying this technique, which does not require a large number of projections for 3-D reconstruction. Furthermore, nanopores in SiN membranes were visualized with high resolution, although the maximum tilt range was strongly reduced due to object geometry, which would normally produce serious missing wedge artifacts under standard SIRT conditions. Unless symmetry restrictions apply<sup>72</sup>, successful reconstructions with such large restrictions on tilt range or the total number of images have not been performed yet. We anticipate that this approach is transferable to a wide range of nanomaterials, including other particles, clusters and membranes, and particularly beam sensitive specimens.



# 8



INTRODUCTION

EXPERIMENTAL METHODS

RESULTS AND DISCUSSION

**CONCLUSION**

APPENDIX



## 8 Conclusion

Regarding the evolution with time of the dimensional ranges they address, 'top down' and 'bottom up' approaches are currently overlapping and their combination will lead to new hybrid methods of manufacture. In this context mesoporous silica seems to be very promising due to its thermal and chemical stability, as well as its simple and multifaceted modifiability. The broad variety of mesoporous silica is reflected by its diverse potential uses, e.g. as low  $k$  dielectrics in integrated circuits or as photo-luminescent material for light emitting diodes. By incorporation of bio(-active) molecules even an application in the medical sector would be conceivable, for example colloidal mesoporous silica nanospheres as intelligent drug delivery systems.

Drug uptake and release is mainly influenced by the interactions between the (modified) silica walls and the drug molecules. A detailed investigation of such host-guest interactions can be realized by diffusion measurements. Mesoporous silica thin films seem to be excellent reference systems for such investigations - not only due to their efficient synthesis, but also because functionalization by grafting or co-condensation proceeds similar to bulk material. In addition, there are manifold characterization methods for thin films, like electron and optical microscopy, XRD and especially GISAXS, as well as ellipsometry, IR/Raman and of course diffusion measurements.

In this thesis the method used for visualizing diffusion in mesoporous thin films is single particle tracking - a relatively new technique allowing the determination of local diffusion constants from areas down to only several square micrometers. By combining the obtained trajectories with high-resolution TEM maps of the same area the nature of the real space porous defect structure is revealed. This approach provides detailed information on the real defect structure of porous materials with high spatial resolution that cannot be obtained by scattering methods because of the intrinsic averaging effects. Similarly, highly resolved dynamic information that cannot be extracted from conventional diffusion techniques due to ensemble averaging is obtained in real time. In particular, the presented examples show how a single luminescent molecule travels along the channels of a mesoporous structure and how it bounces back at domain boundaries, forced to find a new way. Furthermore, lateral motion between 'leaky' channels is observed, allowing the molecule to explore different parallel channels within an otherwise well-ordered periodic structure.

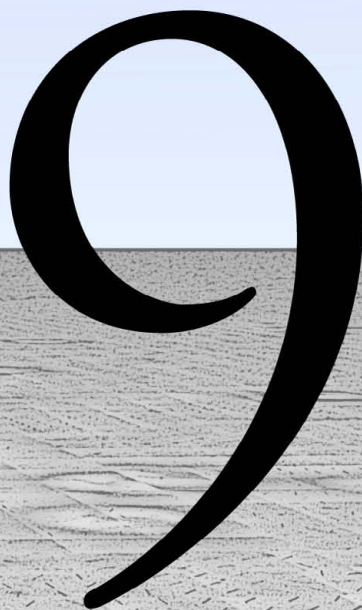
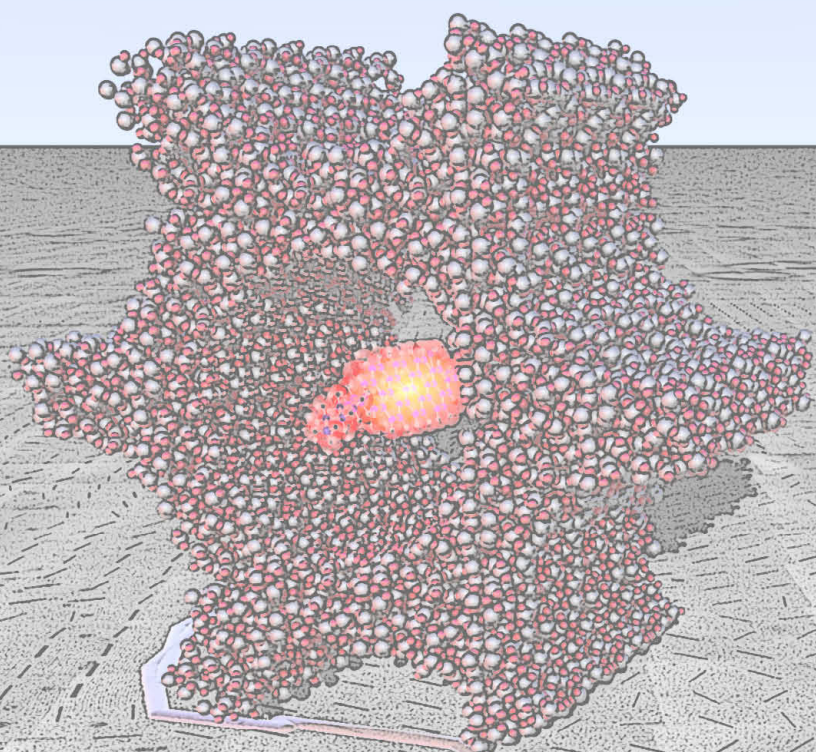
Based on these promising findings, the feasibility of directly observing an

enzymatic reaction within a mesoporous structure was investigated. For this purpose two main issues were examined in more detail: The covalent bonding of biomolecules to the pore walls of mesoporous thin films and the synthesis of mesoporous thin silica films with large, micrometer sized domains. A covalent bonding of trypsin molecules to silica was achieved via “click-chemistry” techniques. The enzymatic activity of such functionalized films was verified by fluorescence spectroscopy. Samples with covalently bound enzymes show much higher conversion rates than samples containing enzymes immobilized by physical adsorption. Micrometer sized domains - the second issue - were obtained by dip coating at extremely slow dipping rates. The domains could be directly visualized by SEM, and single molecule fluorescence measurements showed oriented diffusion of dye molecules over several micrometers. These films functionalized with enzymes should, in principle, allow the direct observation of an enzymatic conversion within their pores, but insufficient pore size seems to impede a high loading and without calcination the film structure is collapsing too fast in aqueous solutions. Hence, future work has to focus on bigger templates and on a synthesis route including calcination, as well as post-grafting.

The last experimental section is dedicated to the visualization of nanostructures by electron tomography. More specifically, discrete tomography is used to calculate three-dimensional images from (S)TEM tilt series of several nanostructured samples. Due to sample limitations resulting in a large missing wedge and large tilt increments, respectively, the 3D structure could not be reconstructed by standard iterative algorithms; even a recently developed discrete algorithm failed until the initial segmentation of the input volume for discrete reconstruction was improved. Masked SIRT iterations were used to get a more accurate starting volume from which, compared to standard SIRT, more accurate gray values were determined. By applying this method, nine STEM images were enough to resolve the distribution of metal nanoclusters in the mesoporous structure of highly electron beam sensitive colloidal silica nanoparticles. Furthermore, it was possible to visualize nanopores in silicon nitride membranes with high resolution, although the maximum tilt range was strongly reduced due to object geometry, which would normally produce serious missing wedge artifacts under standard SIRT conditions. It is expected that the presented approach is transferable to a wide range of nanomaterials, including other particles, clusters and membranes, and particularly beam sensitive specimens.

On the one hand this work intends to present new possibilities on how the combination of optical and electron microscopy methods can be used to gain information not available from the individual techniques. On the other hand it is demonstrated how the quality of tomographic reconstructions of nano structures is strongly increased by incorporation of additional information during reconstruction. In both cases a combination of several techniques (TEM with SPT and DART with masked SIRT, respectively) is the key for visualizing mesostructured objects and their properties. Visualization not only represents a technique facilitating the interpretation of scientific results, but it can also serve to enhance the general appreciation and understanding of nanotechnology.





INTRODUCTION

EXPERIMENTAL METHODS

RESULTS AND DISCUSSION

CONCLUSION

**APPENDIX**



## 9 Appendix

### 9.1 Literature

#### Notes

<sup>1</sup>[http://www3.mercedes-benz.com/teclex/main\\_de.html](http://www3.mercedes-benz.com/teclex/main_de.html), keyword "Nano-Klarlack", as at: 18/01/2008

<sup>2</sup><http://www.intel.com>, as at: 18/01/2008

<sup>3</sup><http://www.nanoTruck.de>, as at: 18/01/2008

<sup>4</sup>Phala, N., v. Steen, E. Intrinsic Reactivity of Gold Nanoparticles: Classical, Semi-empirical and DFT Studies. *Gold Bulletin* **40** (2), 150-153 (2007).

<sup>5</sup>Lue, J.-T. A review of characterization and physical property of metallic nanoparticles. *J. Phys. Chem. Sol* **62**, 1599-1612 (2001).

<sup>6</sup>Guczi, L., Petö, G., Beck, A., Frey, K., Geszti, O., Molnár, G., Daróczy, C. Gold Nanoparticles Deposited on SiO<sub>2</sub>/Si(100): Correlation between Size, Electron Structure, and Activity in CO Oxidation. *J. Am. Chem. Soc* **125**, 4332-4337 (2003).

<sup>7</sup>Dabbousi, B. O., Rodriguez-Viejo, J., Mikulec, F. V., Heine, J. R., Mattoussi, H., Ober, R., Jensen, K. F., Bawendi, M. G. (CdSe)ZnS core-shell quantum dots: Synthesis and characterization of a size series of highly luminescent nanocrystallites. *J. Phys. Chem. B* **101** (46), 9463-9475 (1997).

<sup>8</sup>Eustis, S., El-Sayed, M. A Why gold nanoparticles are more precious than pretty gold: Noble metal surface plasmon resonance and its enhancement of the radiative and nonradiative properties of nanocrystals of different shapes. *Chem. Soc. Rev.* **35**, 209-217 (2006).

<sup>9</sup>Federal Ministry of Education and Research (BMBF), nano.DE-Report 2009. Bonn, Berlin 2009

<sup>10</sup>Lux Research, The Nanotech Report, 4th Edition, New York, NY - May 8, 2006

<sup>11</sup>Lux Research 2008: Press Release from 07/22/2008 ([www.luxresearchinc.com/press/RELEASE\\_Nano-SMR\\_7\\_22\\_08.pdf](http://www.luxresearchinc.com/press/RELEASE_Nano-SMR_7_22_08.pdf))

<sup>12</sup>Luther, W., Malanowski, N., Bachmann, G., Hoffknecht, A., Holtmannspötter, D., Zweck, A. Innovations- und Technikanalyse. Nanotechnologie als wirtschaftlicher Wachstumsmarkt. *Zukünftige Technologien Consulting der VDI Technologiezentrum GmbH* (2004)

<sup>13</sup>Federal Ministry of Education and Research (BMBF), Report of the Federal Government on Research 2006

<sup>14</sup>Crommie, M. F., Lutz, C. P., Eigler, D. M. Confinement of electrons to quantum corrals on a metal surface. *Science* **262**, 218-220 (1993).

<sup>15</sup><http://www.almaden.ibm.com/vis/stm/corral.html>, as at: 23/01/2008

<sup>16</sup>Eigler, D. M., Schweizer, E. K. Positioning single atoms with a scanning tunneling microscope. *Nature* **344**, 524-526 (1990).

<sup>17</sup><http://www.vanderbilt.edu/physics/matphys/research>, as at: 21/01/2008

<sup>18</sup>Whatmore, R. W. Nanotechnology big prospects for small engineering. *Ingenia* **9**, 28-33 (2001).

<sup>19</sup><http://www.intel.com>, as at: 28/05/2008

<sup>20</sup>[http://www.toshiba.co.jp/about/press/2007\\_12/pr1201.htm](http://www.toshiba.co.jp/about/press/2007_12/pr1201.htm), as at: 16/04/2008

<sup>21</sup>Lu, W., Lieber, C. M. Nanoelectronics from the bottom up. *Nat. Mater.* **6**, 841-850 (2007).

<sup>22</sup>International technology roadmap of semiconductors, 2007 Edition - Lithography, **2007**

- <sup>23</sup>The Royal Society, Nanoscience and nanotechnologies: opportunities and uncertainties, ISBN 0 85403 604 0, **2004**
- <sup>24</sup>Guth, J.-L., Kessler, H. in Catalysis and zeolites, J. Weitkamp, L. Puppe (Eds), Springer, Berlin, 1999, 1-31
- <sup>25</sup>Wilson, S. T., Lok, B. M., Messina, C. A., Cannan, T. R., Flanigen, E. M. Aluminophosphate molecular sieves: a new class of microporous crystalline inorganic solids. *J. Am. Chem. Soc.* **104**, 1146-1147 (1982).
- <sup>26</sup>Davis, M.E. Zeolite-based catalysts for chemicals synthesis. *Microporous and Mesoporous Materials* **21**, 173-182 (1998).
- <sup>27</sup>Yaghi, O. M., Li, G., Li, H. Selective binding and removal of guests in a microporous metal-organic framework. *Nature* **378**, 703-706 (1995).
- <sup>28</sup>Janiak, C. Functional organic analogues of zeolites based on metal-organic coordination frameworks. *Angew. Chem. Int. Ed.* **36**, 1431-1434 (1997).
- <sup>29</sup>Côté, A. P., Benin, A. I., Ockwig, N. W., O'Keeffe, M., Matzger, A. J., Yaghi, O. M. Porous, Crystalline, Covalent Organic Frameworks. *Science* **310**, 1166-1170 (2005).
- <sup>30</sup>Yaghi, O. M., O'Keeffe, M., Ockwig, N. W., Chae, H. K., Eddaoudi, M., Kim, J. Reticular synthesis and the design of new materials. *Nature* **423**, 705-714 (2003).
- <sup>31</sup>El-Kaderi, H. M., Hunt, J. R., Mendoza-Cortés, J. L., Côté, A. P., Taylor, R. E., O'Keeffe, M., Yaghi, O. M. Designed synthesis of 3D covalent organic frameworks. *Science* **316**, 268-272 (2007).
- <sup>32</sup>Mastalerz, M. The next generation of shape-persistent zeolite analogues: Covalent organic frameworks. *Angew. Chem. Int. Ed.* **47**, 445-447 (2008).
- <sup>33</sup>Kresge, C. T., Leonowicz, M. E., Roth, W. J., Vartuli, J. C., Beck, J. S. Ordered mesoporous molecular sieves synthesized by a liquid-crystal template mechanism. *Nature* **359**, 710-712 (1992).
- <sup>34</sup>Inagaki, S., Fukushima, Y., Kuroda, K. J. Synthesis of Highly Ordered Mesoporous Materials from a Layered Polysilicate. *Chem. Soc., Chem. Commun.* **8**, 680-682 (1993).
- <sup>35</sup>Tanev, P. T., Pinnavaia, T. J. A Neutral Templating Route to Mesoporous Molecular Sieves. *Science* **267**, 865-867 (1995).
- <sup>36</sup>Bagshaw, S. A., Prouzet, E., Pi, Pinnavaia, T. J. Templating of Mesoporous Molecular Sieves by Nonionic Polyethylene Oxide Surfactants. *Science* **269**, 1242-1244 (1995).
- <sup>37</sup>Yu, C., Yu, Y., Miao, L., Zhao, D. Highly ordered mesoporous silica structures templated by poly(butylene oxide) segment di- and tri-block copolymers. *Micro. Meso. Mater.* **44-45**, 65-72 (2001).
- <sup>38</sup>Romero, F., Jiménez, C., Huc, I., Oda, R. Room temperature synthesis of ordered porous silicas templated by symmetric and dissymmetric gemini surfactants  $[C_nH_{2n+1}N(CH_3)_2(CH_2)_2(CH_3)_2NC_mH_{2m+1}]Br_2$ . *Micro. Meso. Mater.* **69**, 43-48 (2004).
- <sup>39</sup>Zhao, D., Feng, J., Huo, Q., Melosh, N., Fredrickson, G. H., Chmelka, B. F., Stucky, G. D. Triblock Copolymer Syntheses of Mesoporous Silica with Periodic 50 to 300 Angstrom Pores. *Science* **279**, 548-552 (1998).
- <sup>40</sup>Zhao, D., Yang, P., Melosh, N., Feng, J., Chmelka, F., Stucky, G. Continuous Mesoporous Silica Films with Highly Ordered Large Pore Structure. *Adv. Mater.* **10(16)**, 1380-1385 (1998).
- <sup>41</sup>Zhao, D., Huo, Q., Feng, J., Chmelka, F., Stucky, G. Nonionic Triblock and Star Diblock Copolymer and Oligomeric Surfactant Syntheses of Highly Ordered, Hydrothermally Stable, Mesoporous Silica Structures. *J. Am. Chem. Soc.* **120**, 6024-6036 (1998).

- <sup>42</sup>Beck, J. S., Vartuli, J. C., Roth, W. J., Leonowicz, M. E., Kresge, C. T., Schmitt, K. D., Chu, C. T.-W., Olson, D. H., Sheppard, E. W., McCullen, S. B., Higgins, J. B., Schlenker, J. L. A new family of mesoporous molecular sieves prepared with liquid-crystal templates. *J. Am. Chem. Soc.* **114**, 10834-10843 (1992).
- <sup>43</sup>Sen, T., Tiddy, G. J. T., Casci, J. L., Anderson, M. W. Synthesis and characterization of hierarchically ordered porous silica materials. *Chem. Mater.* **16**, 2044-2054 (2004).
- <sup>44</sup>Yang, C.-M., Cho, A.-T., Pan, F.-M., Tsai, T.-G., Chao, K.-J. Spin-on mesoporous silica films with ultralow dielectric constants, ordered pore structures, and hydrophobic surfaces. *Adv. Mater.* **13**, 1099-1102 (2001).
- <sup>45</sup>Dag, Ö., Ozin, G. A., Yang, H., Reber, C., Bussière, G. Photoluminescent silicon clusters in oriented hexagonal mesoporous silica film. *Adv. Mater.* **11**, 474-480 (1999).
- <sup>46</sup>Shen, J. L., Lee, Y. C., Liu, Y. L., Yu, C. C., Cheng, P. W., Cheng, C. F. Photoluminescence sites on MCM-48. *Micropor. Mesopor. Mater.* **64**, 135-143 (2003).
- <sup>47</sup>Doshi, D. A., Huesing, N. K., Lu, M., Fan, H., Lu, Y., Simmons-Potter, K., Potter Jr., B. G., Hurd, A. J., Brinker, C. J. Optically defined multifunctional patterning of photosensitive thin-film silica mesophases. *Science* **290**, 107-111 (2000).
- <sup>48</sup>Fuertes, M. C., López-Alcaraz, F. J., Marchi, M. C., Troiani, H. E., Luca, V., Míguez, H., de A. A. Soler-Illia, G. J. Photonic crystals from ordered mesoporous thin-film functional building blocks. *Adv. Funct. Mater.* **17**, 1247-1254 (2007).
- <sup>49</sup>Inagaki, S., Ohtani, O., Goto, Y., Okamoto, K., Ikai, M., Yamanaka, K., Tani, T., Okada, T., Light Harvesting by a Periodic Mesoporous Organosilica Chromophore. *Angew. Chem.* **121**, 4102-4106 (2009).
- <sup>50</sup>Taguchi, A., Sch"uth, F. Ordered mesoporous materials in catalysis. *Micropor. Mesopor. Mater.* **77**, 1-45 (2005).
- <sup>51</sup>Lei, B., Li, B., Zhang, H., Zhang, L., Li, W. Synthesis, characterization, and oxygen sensing properties of functionalized mesoporous SBA-15 and MCM-41 with a covalently linked Ruthenium(II) complex. *J. Phys. Chem. C* **111**, 11291-11301 (2007).
- <sup>52</sup>Che, S., Garcia-Bennett, A. E., Liu, X., Hodgkins, R. P., Wright, P. A., Zhao, D., Terasaki, O., Tatsumi, T. Synthesis of large-pore Ia $\bar{3}d$  mesoporous silica and its tubelike carbon replica. *Angew. Chem. Int. Ed.* **42**, 3930-3934 (2003).
- <sup>53</sup>Aronson, B. J., Blanford, C. F., Stein, A. Solution-phase grafting of titanium dioxide onto the pore surface of mesoporous silicates: Synthesis and structural characterization. *Chem. Mater.* **9**, 2842-2851 (1997).
- <sup>54</sup>Teraoka, Y., Ishida, S., Yamasaki, A., Tomonaga, N., Yasutake, A., Izumi, J., Moriguchi, I., Kagawa, S. Synthesis and characterization of tin oxide-modified mesoporous silica by the repeated post-grafting of tin chloride. *Micropor. Mesopor. Mater.* **48**, 151-158 (2001).
- <sup>55</sup>Angloher, S., Bein., T. Metalorganic modification of periodic mesoporous silica: aromatic nitrogen functionalities. *J. Mater. Chem.* **16**, 3629-3634 (2006).
- <sup>56</sup>Angloher, S., Kecht, J., Bein., T. Optimization of reaction conditions for the metalorganic modification of MCM-41. *Chem. Mater* **19**, 3568-3574 (2007).
- <sup>57</sup>Angloher, Kecht, J., S., Bein., T. Metal-organic modification of periodic mesoporous silica: Multiply bonded systems. *Chem.Mater* **19**, 5797-5802 (2007).
- <sup>58</sup>Lim, M. H., Stein, A. Comparative studies of grafting and direct syntheses of inorganic-organic hybrid mesoporous materials. *Chem. Mater.* **11**, 3285-3295 (1999).

- <sup>59</sup>Yokoi, T., Yoshitakeb, H., Tatsumi, T. Synthesis of amino-functionalized MCM-41 via direct co-condensation and post-synthesis grafting methods using mono-, di- and tri-amino-organoalkoxysilanes. *J. Mater. Chem.* **14**, 951-957 (2004).
- <sup>60</sup>Lesaint, C., Lebeau, B., Marichal, C., Patarin, J. Synthesis of mesoporous silica materials functionalized with n-propyl groups. *Micropor. Mesopor. Mater.* **83**, 76-84 (2005).
- <sup>61</sup>F., Hoffmann, M., Cornelius, J., Morell, M. Fröba Silica-based mesoporous organic-inorganic hybrid materials. *Angew. Chem. Int. Ed.* **45**, 3216-3251 (2006).
- <sup>62</sup>Ogawa, M. Formation of Novel Oriented Transparent Films of Layered Silica-Surfactant Nanocomposites. *J. Am. Chem. Soc.* **116**, 7941-7942 (1994).
- <sup>63</sup>Sanchez, C., Boissière, C., Grosso, D., Laberty, C., Nicole, L. Design, Synthesis, and Properties of Inorganic and Hybrid Thin Films Having Periodically Organized Nanoporosity. *Chem. Mater.* **20**, 682-737 (2008).
- <sup>64</sup>Bach, U., Lupo, D., Comte, P., Moser, J. E., Weissörtel, F., Salbeck, J., Spreitzer, H., Grätzel, M. Solid-state dye-sensitized mesoporous TiO<sub>2</sub> solar cells with high photon-to-electron conversion efficiencies. *Nature* **395**, 583-585 (1998).
- <sup>65</sup>Shibata, H., Ogura, T., Mukai, T., Ohkubo, T., Sakai, H., Abe, M. Direct Synthesis of Mesoporous Titania Particles Having a Crystalline Wall. *J. Am. Chem. Soc.* **127**, 16396-16397 (2005).
- <sup>66</sup>Wagner, E. Programmed drug delivery: nanosystems for tumor targeting. *Expert Opin. Biol. Ther.* **7(5)**, 587-593 (2007).
- <sup>67</sup>nanosystems initiative munich, Research Area K  
<http://www.nano-initiative-munich.de/research-areas/k/design-of-nano-structured-drug-delivery-devices/>, as at: 02/01/2008
- <sup>68</sup>Kukla, V., Kornatowski, J., Demuth, D., Girnus, I., Pfeifer, H., Rees, L. V. C., Schunk, S., Unger, K. K., Kärger, J. NMR studies of single-file diffusion in unidimensional channel zeolites. *Science* **272**, 702-704 (1996).
- <sup>69</sup>Benes, N. E., Jobic, H., Verweij, H.  
Quasi-elastic neutron scattering study of the mobility of methane in microporous silica. *Micropor. Mesopor. Mater.* **43**, 147-152 (2001).
- <sup>70</sup>Fu, Y., Ye, F., Sanders, W. G., Collinson, M. M., Higgins, D. A. Single Molecule Spectroscopy Studies of Diffusion in Mesoporous Silica Thin Films. *J. Phys. Chem. B* **110**, 9164-9170 (2006).
- <sup>71</sup>Sprague, B. L., Pego, R. L., Stavreva, D. A., McNally, J. G. Analysis of Binding Reactions by Fluorescence Recovery after Photobleaching. *Biophys. J.* **86**, 3473-3495 (2006).
- <sup>72</sup>de Rosier, D. J., Klug, A. Reconstruction of Three Dimensional Structures from Electron Microscopy. *Nature* **217**, 130-134 (1968).
- <sup>73</sup>Henderson, R., Unwin, P. N. Three-Dimensional model of purple membrane obtained by electron microscopy. *Nature* **257**, 28-32 (1975).
- <sup>74</sup>Olins, D. E., Olins, A. L., Levy, H. A., Durfee, R. C., Margle, S. M., Tinnel, E. P., Durfee, R. C. Electron Microscope Tomography: Transcription in Three Dimensions. *Science* **220**, 498-500 (1983).
- <sup>75</sup>Nickell, S., Kofler, C., Leis, A. P., Baumeister, W. A visual approach to proteomics. *Nat. Reviews* **7**, 225-230 (2006).
- <sup>76</sup>He, W., Cowin, P., Stokes, D. L. Untangling Desmosomal Knots with Electron Tomography. *Science* **302**, 109-113 (2003).

- <sup>77</sup>Grabenbauer, M., Geerts, W. J. C., Fernandez-Rodriguez, J., Hoenger, A., Koster, A. J., Nilsson, T. Correlative microscopy and electron tomography of GFP through photooxidation. *Nat. Methods* **2**, 857-862 (2005).
- <sup>78</sup>Beck, M., Lučić, V., Förster, F., Baumeister, W., Medalia, O. Snapshots of nuclear pore complexes in action captured by cryo-electron tomography. *Nature* **449**, 611-615 (2007).
- <sup>79</sup>He, W., Ladinsky, M. S., Huey-Tubman, K. E., Jensen, G. J., McIntosh, J. R., Björkman, P. J. FcRn-mediated antibody transport across epithelial cells revealed by electron tomography. *Nature* **455**, 542-546 (2008).
- <sup>80</sup>Janssen, A. H., Koster, A. J., de Jong, K. P. Three-Dimensional Transmission Electron Microscopic Observations of Mesopores in Dealuminated Zeolite Y. *Angew. Chem.* **113**, 1136-1138 (2001).
- <sup>81</sup>Fan, C., Qiu, H., Ruan, J., Terasaki, O., Yan, Y., Wei, Z., Che, S. Formation of Chiral Mesopores in Conducting Polymers by Chiral-Lipid-Ribbon Templating and 'Seeding' Route. *Adv. Funct. Mater.* **18**, 2699-2707 (2008).
- <sup>82</sup>Ersen, O., Parmentier, J., Solovyov, L. A., Drillon, M., Pham-Huu, C., Werckmann, J., Schultz, P. Direct Observation of Stacking Faults and Pore Connections in Ordered Cage-Type Mesoporous Silica FDU-12 by Electron Tomography. *J. Am. Chem. Soc.* **130**, 16800-16806 (2008).
- <sup>83</sup>Friedrich, H., Sietsma, J. R. A., de Jongh, P. E., Verkleij, A. J., de Jong, K. P. Measuring Location, Size, Distribution, and Loading of NiO Crystallites in Individual SBA-15 Pores by Electron Tomography. *J. Am. Chem. Soc.* **129**, 10249-10254 (2007).
- <sup>84</sup>Janssen, A. H., Yang, C.-M., Wang, Y., Schüth, F., Koster, A. J., de Jong, K. P. Localization of Small Metal (Oxide) Particles in SBA-15 Using Bright-Field Electron Tomography. *J. Phys. Chem. B* **107**, 10552-10556 (2003).
- <sup>85</sup>Li, Z., Kübel, C., Pârvulescu, V. I., Richards, R. Size Tunable Gold Nanorods Evenly Distributed in the Channels of Mesoporous Silica. *ACS Nano* **2**, 1205-1212 (2008).
- <sup>86</sup>Gabor T. Herman and Attila Kuba, *Discrete Tomography - Foundations, Algorithms, and Applications*, Birkhäuser Boston, 1999
- <sup>87</sup>Gabor T. Herman and Attila Kuba, *Advances in Discrete Tomography and Its Applications*, Birkhäuser Boston, 2007
- <sup>88</sup>Batenburg, K. J., Sijbers, J. DART: A FAST HEURISTIC ALGEBRAIC RECONSTRUCTION ALGORITHM FOR DISCRETE TOMOGRAPHY. *IEEE International Conference on Image Processing, ICIP* **4**, IV-133 - IV-136 (2007).
- <sup>89</sup>Batenburg, K. J., Bals, S., Sijbers, J., Kübel, C., Midgley, P. A., Hernandez, J. C., Kaiser, U., Encina, E. R., Coronado, E. A., Van Tendeloo, G. 3D imaging of nanomaterials by discrete tomography. *Ultramicroscopy* **109**, 730-740 (2009).
- <sup>90</sup>Beck, J. S., Vartuli, J. C. Recent advances in the synthesis, characterization and applications of mesoporous molecular sieves. *Curr. Opin. Solid State Mater. Sci.* **1**, 76-87 (1996).
- <sup>91</sup>Corma, A. From Microporous to Mesoporous Molecular Sieve Materials and Their Use in Catalysis. *Chem. Rev.* **97**, 2373-2419 (1997).
- <sup>92</sup>Zhao, D., Yang, P., Huo, Q., Chmelka, B. F., Stucky, G. D. Topological construction of mesoporous materials. *Curr. Opin. Solid State Mater. Sci.* **3**, 111-121 (1998).
- <sup>93</sup>Ciesla, U., Schüth, F. Ordered mesoporous materials. *Micropor. Mesopor. Mater.* **27**, 131-149 (1999).



- <sup>94</sup>Ying, J. Y., Mehnert, C. P., Wong, M. S. Synthesis and Applications of Supramolecular-Templated Mesoporous Materials. *Angew. Chem. Int. Ed.* **38**, 56-77 (1999).
- <sup>95</sup>Davis, M. E. Ordered porous materials for emerging applications. *Nature* **417**, 813-821 (2002).
- <sup>96</sup>Patarin, J. Lebeau, B., Zana, R. Recent advances in the formation mechanisms of organized mesoporous materials. *Curr. Opin. Colloid Interface Sci.* **7**, 107-115 (2002).
- <sup>97</sup>He, X., Antonelli, D. Recent Advances in Synthesis and Applications of Transition Metal Containing Mesoporous Molecular Sieves. *Angew. Chem. Int. Ed.* **41**, 214-229 (2002).
- <sup>98</sup>Wight, A. P., Davis, M. E. Design and Preparation of Organic-Inorganic Hybrid Catalysts. *Chem. Rev.* **102**, 3589-3614 (2002).
- <sup>99</sup>de Vos, D. E., Dams, M., Sels, B. F., Jacobs, P. A. Ordered Mesoporous and Microporous Molecular Sieves Functionalized with Transition Metal Complexes as Catalysts for Selective Organic Transformations. *Chem. Rev.* **102**, 3615-3640 (2002).
- <sup>100</sup>de A. A. Soler-Illia, G. J. Sanchez, C., Lebeau, B., Patarin, J. Chemical Strategies To Design Textured Materials: from Microporous and Mesoporous Oxides to Nanonetworks and Hierarchical Structures. *Chem. Rev.* **102**, 4093-4138 (2002).
- <sup>101</sup>Schüth, F. Endo- and Exotemplating to Create High-Surface-Area Inorganic Materials. *Angew. Chem. Int. Ed.* **42**, 3604-3622 (2003).
- <sup>102</sup>Maschmeyer, T., van de Water, L. An Overview of Zeolite, Zeotype and Mesoporous Solids Chemistry: Design, Synthesis and Catalytic Properties. *Cat. Fine Chem. Syn.* **4**, 1-38 (2006).
- <sup>103</sup>Wan, Y., Zhao, D. On the Controllable Soft-Templating Approach to Mesoporous Silicates. *Chem. Rev.* **107**, 2821-2860 (2007).
- <sup>104</sup>Grosso, D., Cagnol, F., de A. A. Soler-Illia, G. J., Crepaldi, E.L., Amenitsch, H., Brunet-Bruneau, A., Bourgeois, A., Sanchez, C. Fundamentals of Mesostructuring Through Evaporation-Induced Self-Assembly. *Adv. Func. Mater.* **14**, 309-322 (2004).
- <sup>105</sup>Chao, K.-J., Liu, P.-H., Huang, K.-Y. Thin films of mesoporous silica: characterization and applications. *C. R. Chimie* **8**, 727-739 (2005).
- <sup>106</sup>de A. A. Soler-Illia, G. J., Innocenzi, P. Mesoporous Hybrid Thin Films: The Physics and Chemistry Beneath. *Chem. Eur. J.* **12**, 4478-4494 (2006).
- <sup>107</sup>Smarsly, B., Antonietti, M. Block Copolymer Assemblies as Templates for the Generation of Mesoporous Inorganic Materials and Crystalline Films. *Eur. J. Inorg. Chem.* **6**, 1111-1119 (2006).
- <sup>108</sup>Schüth, F. Non-siliceous Mesostructured and Mesoporous Materials. *Chem. Mater.* **13**, 3184-3195 (2001).
- <sup>109</sup>Inagaki, S., Guan, S., Ohsuna, T., Terasaki, O. An ordered mesoporous organosilica hybrid material with a crystal-like wall structure. *Nature* **416**, 304-307 (2002).
- <sup>110</sup>Crepaldi, E. L., Soler-Illia, G. J. de A. A., Grosso, D., Cagnol, F., Ribot, F., Sanchez, C. Controlled Formation of Highly Organized Mesoporous Titania Thin Films: From Mesostructured Hybrids to Mesoporous Nanoanatase TiO<sub>2</sub>. *J. Am. Chem. Soc.* **125**, 9770-9786 (2003).
- <sup>111</sup>Lai, X., Li, X., Geng, W., Tu, J., Li, J., Qiu, S. Ordered Mesoporous Copper Oxide with Crystalline Walls. *Angew. Chem. Int. Ed.* **46**, 738-741 (2007).
- <sup>112</sup>Chen, C. Y., Li, H. X., Davis, M. E. Studies on mesoporous materials. I. Synthesis and characterization of MCM-41. *Micropor. Mater.* **2**, 17-26 (1993).
- <sup>113</sup>Attard, G. S., Bartlett, P. N., Coleman, N. R. B., Elliott, J. M., Owen, J. R., Wang J. H. Mesoporous Platinum Films from Lyotropic Liquid Crystalline Phases. *Science* **278**, 838-840

(1997).

<sup>114</sup>Sun, D., Riley, A. E., Cadby, A. J., Richman, E. K., Korlann, S. D., Tolbert, S. H. Hexagonal nanoporous germanium through surfactant-driven self-assembly of Zintl clusters. *Nature* **441**, 1126-1130 (2006).

<sup>115</sup>Armatas, G. S., Kanatzidis, M. G. Mesostructured germanium with cubic pore symmetry. *Nature* **441**, 1122-1125 (2006).

<sup>116</sup>Armatas, G. S., Kanatzidis, M. G. Hexagonal Mesoporous Germanium. *Science* **313**, 817-820 (2006).

<sup>117</sup>Yang, P., Zhao, D., Margolese, D. I., Chmelka, B. F., Stucky, G. D. Generalized syntheses of large-pore mesoporous metal oxides with semicrystalline frameworks. *Nature* **396**, 152-155 (1998).

<sup>118</sup>Yang, P., Zhao, D., Margolese, D. I., Chmelka, B. F., Stucky, G. D. Block Copolymer Templating Syntheses of Mesoporous Metal Oxides with Large Ordering Lengths and Semicrystalline Framework. *Chem. Mater.* **11**, 2813-2826 (1999).

<sup>119</sup>Emons, T. T., Li, J., Nazar, L. F. Synthesis and Characterization of Mesoporous Indium Tin Oxide Possessing an Electronically Conductive Framework. *J. Am. Chem. Soc.* **124**, 8516-8517 (2002).

<sup>120</sup>Lyu, Y.-Y., Yi, S. H., Shon, J. K., Chang, S., Pu, L. S., Lee, S.-Y., Yie, J. E., Char, K., Stucky, G. D., Kim, J. M. Highly Stable Mesoporous Metal Oxides Using Nano-Propping Hybrid Gemini Surfactants. *J. Am. Chem. Soc.* **126**, 2310-2311 (2004).

<sup>121</sup>Tian, Z. R., Tong, W., Wang, J. Y., Duan, N. G., Krishnan, V. V., Suib, S. L. Manganese Oxide Mesoporous Structures: Mixed-Valent Semiconducting Catalysts. *Science* **276**, 926-930 (1997).

<sup>122</sup>Chen, J., Burger, C., Krishnan, C. V., Chu, B. Morphogenesis of Highly Ordered Mixed-Valent Mesoporous Molybdenum Oxides. *J. Am. Chem. Soc.* **127**, 14140-14141 (2005).

<sup>123</sup>Sinha, A. K., Suzuki, K., Takahara, M., Azuma, H., Nonaka, T., Fukumoto, K. Mesostructured Manganese Oxide/Gold Nanoparticle Composites for Extensive Air Purification. *Angew. Chem. Int. Ed.* **46**, 2891-2894 (2007).

<sup>124</sup>Asefa, T., MacLachlan, M. J., Coombs, N., Ozin, G. A. Periodic mesoporous organosilicas with organic groups inside the channelwalls. *Nature* **402**, 867-871 (1999).

<sup>125</sup>Guan, S., Inagaki, S., Ohsuna, T., Terasaki, O. Cubic Hybrid Organic-Inorganic Mesoporous Crystal with a Decaohedral Shape. *J. Am. Chem. Soc.* **122**, 5660-5661 (2000).

<sup>126</sup>Hunks, W. J., Ozin, G. A. Challenges and advances in the chemistry of periodic mesoporous organosilicas (PMOs). *J. Mater. Chem.* **15**, 3716-3724 (2005).

<sup>127</sup>Ryoo, R., Joo, S. H., Jun, S. Synthesis of Highly Ordered Carbon Molecular Sieves via Template-Mediated Structural Transformation. *J. Phys. Chem. B* **103**, 7743-7746 (1999).

<sup>128</sup>Lee, J.-S., Joo, S., H., Ryoo, R. Synthesis of Mesoporous Silicas of Controlled Pore Wall Thickness and Their Replication to Ordered Nanoporous Carbons with Various Pore Diameters. *J. Am. Chem. Soc.* **124**, 1156-1157 (2002).

<sup>129</sup>Kim, T.-W., Park, I.-S., Ryoo, R. A Synthetic Route to Ordered Mesoporous Carbon Materials with Graphitic Pore Walls. *Angew. Chem. Int. Ed.* **42**, 4375-4379 (2003).

<sup>130</sup>Jun, S., Joo, S. H., Ryoo, R., Kruk, M., Jaroniec, M., Liu, Z., Ohsuna, T., Terasaki, O. Synthesis of New, Nanoporous Carbon with Hexagonally Ordered Mesostructure. *J. Am. Chem. Soc.* **122**, 10712-10713 (2000).

- <sup>131</sup>Zhang, F., Meng, Y., Gu, D., Yan, Y., Yu, C., Tu, B., Zhao, D. A Facile Aqueous Route to Synthesize Highly Ordered Mesoporous Polymers and Carbon Frameworks with  $Ia\bar{3}d$  Bicontinuous Cubic Structure. *J. Am. Chem. Soc.* **127**, 13508-13509 (2005).
- <sup>132</sup>Meng, Y., Gu, D., Zhang, F., Shi, Y., Yang, H., Li, Z., Yu, C., Tu, B., Zhao, D. Ordered Mesoporous Polymers and Homologous Carbon Frameworks: Amphiphilic Surfactant Templating and Direct Transformation. *Angew. Chem. Int. Ed.* **44**, 7053-7059 (2005).
- <sup>133</sup>Huang, Y., Cai, H., Yu, T., Zhang, F., Zhang, F., Meng, Y., Gu, D., Wan, Y., Sun, X., Tu, B., Zhao, D. Formation of Mesoporous Carbon With a Face-Centered-Cubic  $Fd\bar{3}m$  Structure and Bimodal Architectural Pores From the Reverse Amphiphilic Triblock Copolymer PPO-PEO-PPO. *Angew. Chem. Int. Ed.* **46**, 1089-1093 (2007).
- <sup>134</sup>Brinker, C. J., Lu, Y., Sellinger, A., Fan, H. Evaporation-Induced Self-Assembly: Nanostructures Made Easy. *Adv. Mater.* **11**, 579-585 (1999).
- <sup>135</sup>Kirstein, J., Platschek, B., Jung, C., Brown, R., Bein, T., Bräuchle, C. Exploration of nanostructured channel systems with singlemolecule probes. *Nature Mater.* **6**, 303-310 (2007).
- <sup>136</sup>Platschek, B., Petkov, N., Bein, T. Tuning the Structure and Orientation of Hexagonally Ordered Mesoporous Channels in Anodic Alumina Membrane Hosts: A 2D Small-Angle X-ray Scattering Study. *Angew. Chem. Int. Ed.* **45**, 1134-1138 (2006).
- <sup>137</sup>Platschek, B., Köhn, R., Döblinger, M., Bein, T. Formation Mechanism of Mesostructured Silica in Confined Space: An In Situ GISAXS Study. *Chem. Phys. Chem.* **9**, 2059-2067 (2008).
- <sup>138</sup>A. C. Kak and Malcolm Slaney, *Principles of Computerized Tomographic Imaging*, IEEE Press, 1988.
- <sup>139</sup>Kawase, N., Kato, M., Nishioka, H., Jinnai, H. Transmission electron microtomography without the "missing wedge" for quantitative structural analysis. *Ultramicroscopy* **107**, 8-15 (2007).
- <sup>140</sup>Midgley, P. A., Weyland, M., Yates, T. J. V., Arslan, I., Dunin-Borkowski, R. E., Thomas, J. M. Nanoscale scanning transmission electron tomography. *J. Microscopy* **223**, 185-190 (2006).
- <sup>141</sup>Klar, T. A., Hell, S. W. Subdiffraction resolution in far-field fluorescence microscopy. *Optics Letters* **24**, 954-956 (1999).
- <sup>142</sup>Hell, S. W. Far-Field Optical Nanoscopy. *Science* **316**, 1153-1158 (2007).
- <sup>143</sup>Rittweger, E., Han, K. Y., Irvine, S. E., Eggeling, C., Hell, S. W. STED microscopy reveals crystal colour centres with nanometric resolution. *Nature Photonics* **3**, 144-147 (2009).
- <sup>144</sup>Jung, C., Kirstein, J., Platschek, B., Bein, T., Budde, M., Frank, I., Müllen, K., Michaelis, J., Bräuchle, C. Diffusion of Oriented Single Molecules with Switchable Mobility in Networks of Long Unidimensional Nanochannels. *J. Am. Chem. Soc.* **130**, 1638-1648 (2008).
- <sup>145</sup>Tamarat, P., Maali, A., Lounis, B., Orrit, M. Ten Years of Single-Molecule Spectroscopy. *J. Phys. Chem. A* **104**, 1-16 (2000).
- <sup>146</sup>Moerner, W. E. A Dozen Years of Single-Molecule Spectroscopy in Physics, Chemistry, and Biophysics. *J. Phys. Chem. B* **106**, 910-927 (2002).
- <sup>147</sup>Kulzer, F., Orrit, M. Single-molecule Optics. *Ann. Rev. Phys. Chem.* **55**, 585-611 (2004).
- <sup>148</sup>Weiss, S. Fluorescence Spectroscopy of Single Biomolecules. *Science* **283**, 1676-1683 (1999).
- <sup>149</sup>Kitamura, K., Tokunaga, M., Iwane, A. H., Yanagida, T. A single myosin head moves along an actin filament with regular steps of 5.3 nanometres. *Nature* **397**, 129-134 (1999).
- <sup>150</sup>Seisenberger, G., Ried, M. U., Endreš, T., Büning, H., Hallek, M., Bräuchle, C. Real-time single-molecule imaging of the infection pathway of an adeno-associated virus. *Science* **294**, 1929-1932 (2001).

- <sup>151</sup>Yildiz, A., Forkey, J. N., McKinney, S. A., Ha, T., Goldman, Y. E., Selvin, P. R. Myosin V Walks Hand-Over-Hand: Single Fluorophore Imaging with 1.5-nm Localization. *Science* **300**, 2061-2065 (2003).
- <sup>152</sup>Bacia, K., Kim, S. A., Schwille, P. Fluorescence cross-correlation spectroscopy in living cells. *Nature Methods* **3**, 83-89 (2006).
- <sup>153</sup>Shiroguchi, K., Kinoshita Jr., K. Myosin V Walks by Lever Action and Brownian Motion. *Science* **316**, 1208-1212 (2007).
- <sup>154</sup>Schindler, F., Lupton, J. M., Müller, J., Feldmann, J., Scherf, U. How single conjugated polymer molecules respond to electric fields. *Nat. Mater.* **5**, 141-146 (2006).
- <sup>155</sup>McCain, K. S., Hanley, D. C., Harris, J. M. Single-molecule fluorescence trajectories for investigating molecular transport in thin silica sol-gel films. *Anal. Chem.* **75**, 4351-4359 (2003).
- <sup>156</sup>Werley, C. A., Moerner, W. E. Single-molecule nanoprobe explores defects in spin-grown crystals. *J. Phys. Chem. B* **110**, 18939-18944 (2006).
- <sup>157</sup>Vanden Bout, D. A., Yip, W.-T., Hu, D., Fu, D.-K., Swager, T. M., Barbara, P. F. Discrete Intensity Jumps and Intramolecular Electronic Energy Transfer in the Spectroscopy of Single Conjugated Polymer Molecules. *Science* **277**, 1074-1077 (1997).
- <sup>158</sup>Hellriegel, C., Kirstein, J., Bräuchle, C., Latour, V., Pigot, T., Olivier, R., Lacombe, S., Brown, R., Guieu, V., Payrastra, C., Izquierdo, A., Mocho, P. Diffusion of Single Streptocyanine Molecules in the Nanoporous Network of Sol-Gel Glasses. *J. Phys. Chem. B* **108**, 14699-14709 (2004).
- <sup>159</sup>García-Parajó, M. F., Veerman, J. A., Bouwhuis, R., Vallée, R., van Hulst, N. F. Optical Probing of Single Fluorescent Molecules and Proteins. *Chem. Phys. Chem.* **2**, 347-360 (2001).
- <sup>160</sup>Saxton, M. J., Jacobson, K. Single-particle tracking: applications to membrane dynamics. *Annu. Rev. Biophys. Biomol. Struct.* **26**, 373-399 (1997).
- <sup>161</sup>Qian, H., Sheetz, M. P., Elson, E. L. Single particle tracking - Analysis of diffusion and flow in two-dimensional systems. *Biophys. J.* **60**, 910-921 (1991).
- <sup>162</sup>Schütz, G. J., Schindler, H., Schmidt, Th. Single-Molecule Microscopy on Model Membranes Reveals Anomalous Diffusion. *Biophys. J.* **73**, 1073-1080 (1997).
- <sup>163</sup>Basché, T., Kummer, S., Bräuchle, C. Direct spectroscopic observation of quantum jumps of a single molecule. *Nature* **373**, 132-134 (1995).
- <sup>164</sup>Kulzer, F., Kummer, S., Matzke, R., Bräuchle, C., Basché, T. Single-molecule optical switching of terrylene in p-terphenyl. *Nature* **387**, 688-691 (1997).
- <sup>165</sup>Seebacher, C., Hellriegel, C., Christoph Bräuchle, Bräuchle, C. Orientational Behavior of Single Molecules in Molecular Sieves: A Study of Oxazine Dyes in AlPO<sub>4</sub>-5 Crystals. *J. Phys. Chem. B* **107**, 5445-5452 (2003).
- <sup>166</sup>Hillhouse, H. W., van Egmond, J. W., Tsapatsis, M., Hanson, J. C., Larese, J. Z. The interpretation of X-ray diffraction data for the determination of channel orientation in mesoporous films. *Micro. Meso. Mater.* **44-45**, 639-643 (2001).
- <sup>167</sup>Roth, S. V., Döhrmann, R., Dommach, M., Kuhlmann, M., Kröger, I., Gehrke, R., Walter, H., Schroer, C., Lengeler, B., Müller-Buschbaum, P. Small-angle options of the upgraded ultrasmall-angle x-ray scattering beamline BW4 at HASYLAB. *Rev. Sci. Instr.* **1-7**, 55-59 (2006).
- <sup>168</sup>Besson, S., Gacoin, T., Jacquiod, C., Ricolleau, C., Babonneaud, D., Boilot, J.-P. Structural study of 3D-hexagonal mesoporous spin-coated sol-gel films. *J. Mater. Chem.* **10**, 1331-1336 (2000).
- <sup>169</sup>Klotz, M., Albouy, P.-A., Ayral, A., Ménager, C., Grosso, D., Van der Lee, A., Cabuil, V.,

Babonneau, F., Guizard, C. The True Structure of Hexagonal Mesophase-Templated Silica Films As Revealed by X-ray Scattering: Effects of Thermal Treatments and of Nanoparticle Seeding. *Chem. Mater.* **12**, 1721-1728 (2000).

<sup>170</sup>Grosso, D., Balkenende, A. R., Albouy, P. A., Lavergne, M., Mazerollese, L., Babonneau, F. Highly oriented 3D-hexagonal silica thin films produced with cetyltrimethylammonium bromide. *J. Mater. Chem.* **10**, 2085-2089 (2000).

<sup>171</sup>Grosso, D., de A. A. Soler-Illia, G. J., Babonneau, F., Sanchez, C., Albouy, P.-A., Brunet-Bruneau, A., Balkenende, A. R. Highly Organized Mesoporous Titania Thin Films Showing Mono-Oriented 2D Hexagonal Channels. *Adv. Mater.* **13**, 1085-1090 (2001).

<sup>172</sup>Grosso, D., Balkenende, A. R., Albouy, P. A., Ayrál, A., Amenitsch, H., Babonneau, F. Two-Dimensional Hexagonal Mesoporous Silica Thin Films Prepared from Block Copolymers: Detailed Characterization and Formation Mechanism. *Chem. Mater.* **13**, 1848-1856 (2001).

<sup>173</sup>Falcaro, P., Grosso, D., Amenitsch, H., Innocenzi, P. Silica Orthorhombic Mesostructured Films with Low Refractive Index and High Thermal Stability. *J. Phys. Chem. B* **108**, 10942-10948 (2004).

<sup>174</sup>Hayward, R. C., Alberius, P. C. A., Kramer, E. J., Chmelka, B. F. Thin Films of Bicontinuous Cubic Mesostructured Silica Templated by a Nonionic Surfactant. *Langmuir* **20**, 5998-6004 (2004).

<sup>175</sup>Tate, M. P., Eggiman, B. W., Kowalski, J. D., Hillhouse, H. W. Order and Orientation Control of Mesoporous Silica Films on Conducting Gold Substrates Formed by Dip-Coating and Self-Assembly: A Grazing Angle of Incidence Small-Angle X-ray Scattering and Field Emission Scanning Electron Microscopy Study. *Langmuir* **21**, 10112-10118 (2005).

<sup>176</sup>Innocenzi, P., Malfatti, L., Kidchob, T., Falcaro, P., Costacurta, S., Guglielmi, M., Mattei, G., Bello V., Amenitsch, H. Thermal-induced phase transitions in self-assembled mesostructured films studied by small-angle X-ray scattering. *J. Synchrotron Rad.* **12**, 734-738 (2005).

<sup>177</sup>Gibaud, A., Dourdain, S., Vignaud, G. Analysis of mesoporous thin films by X-ray reflectivity, optical reflectivity and grazing incidence small angle X-ray scattering. *Appl. Surf. Sci.* **253**, 3-11 (2006).

<sup>178</sup>Tanaka, S., Tate, M. P., Nishiyama, N., Ueyama, K., Hillhouse, H. W. Structure of Mesoporous Silica Thin Films Prepared by Contacting PEO<sub>106</sub>-PPO<sub>70</sub>-PEO<sub>106</sub> Films with Vaporized TEOS. *Chem. Mater.* **18**, 5461-5466 (2006).

<sup>179</sup>Park, S., Lee, D. H., Xu, J., Kim, B., Hong, S. W., Jeong, U., Xu, T., Russell, T. P. Macroscopic 10-Terabit-per-Square-Inch Arrays from Block Copolymers with Lateral Order. *Science* **323**, 1030-1033 (2009).

<sup>180</sup>Renaud, G., Lazzari, R., Revenant, C., Barbier, A., Noblet, M., Ulrich, O., Leroy, F., Jupille, J., Borensztein, Y., Henry, C. R., Deville, J.-P., Scheurer, F., Mane-Mane, J., Fruchart, O. Real-Time Monitoring of Growing Nanoparticles. *Science* **300**, 1416-1419 (2003).

<sup>181</sup>Lin, Y., Böker, A., He, J., Sill, K., Xiang, H., Abetz, C., Li, X., Wang, J., Emrick, T., Long, S., Wang, Q., Balazs, A., Russell, T. P. Self-directed self-assembly of nanoparticle/copolymer mixtures. *Nature* **434**, 55-59 (2005).

<sup>182</sup>Figure6.jpg on [http://www.jawoollam.com/tutorial\\_4.html](http://www.jawoollam.com/tutorial_4.html), as at: 17/05/2010

<sup>183</sup>Hellriegel, C., Kirstein, J., Bräuchle, C. Tracking of single molecules as a powerful method to characterize diffusivity of organic species in mesoporous materials. *New J. Phys.* **7**, 23 (2005).

<sup>184</sup>Schloßbauer, A., Schaffert, D., Kecht, J., Wagner, E., Bein, T. Click Chemistry for High-Density Biofunctionalization of Mesoporous Silica. *J. Am. Chem. Soc.* **130(38)**, 12558-12559



(2008).

<sup>185</sup>Naik, S. P., Yamakita, S., Ogura, M., Okubo, T. Studies on mesoporous silica films synthesized using F127, a triblock co-polymer. *Micro. Meso. Mater.* **75**, 51-59 (2004).

<sup>186</sup>Jung, C., Hellriegel, C., Michaelis, J., Bräuchle, C. Single-molecule traffic in mesoporous materials: translational, orientational, and spectral dynamics. *Adv. Mater.* **19**, 956-960 (2007).

<sup>187</sup>Schmidt, T., Schütz, G. J., Baumgartner, W., Gruber, H. J., Schindler, H. Imaging of single molecule diffusion. *Proc. Natl Acad. Sci. USA* **93**, 2926-2929 (1996).

<sup>188</sup>Roeffaers, M. B. J., Sels, B. F., Uji-i, H., De Schryver, F. C., Jacobs, P. A., De Vos, D. E., Hofkens, J. Spatially resolved observation of crystalface-dependent catalysis by single turnover counting. *Nature* **439**, 572-575 (2006).

<sup>189</sup>Sakamoto, Y., Kaneda, M., Terasaki, O., Zhao, D. Y., Kim, J. M., Stucky, G., Shin, H. J., Ryoo, R Direct imaging of the pores and cages of three-dimensional mesoporous materials. *Nature* **408**, 449-453 (2000).

<sup>190</sup>C. J. Brinker and G. W. Scherrer, Sol-Gel Science. The Physics and Chemistry of Sol-Gel Processing, Academic Press, San Diego, 1990.

<sup>191</sup>Alexandridis, P., Zhou, D., Khan, A. Lyotropic liquid crystallinity in amphiphilic block copolymers: Temperature effects on phase behavior and structure for poly(ethylene oxide)-b-poly(propylene oxide)-b-poly(ethylene oxide) copolymers of different composition. *Langmuir* **12**, 2690-2700 (1996).

<sup>192</sup>Innocenzi, P., Malfatti, L., Kidchob, T., Falcaro, P., Costacurta, S., Guglielmi, M., Mattei, G., Belloc, V., Amenitsch, H. Thermal-induced phase transitions in self-assembled mesostructured films studied by small-angle X-ray scattering. *J. Synchrotron Rad.* **12**, 734-738 (2005).

<sup>193</sup>Schmid, A., Hollmann, F., Park, J. B., Bühler, B. The use of enzymes in the chemical industry in Europe. *Curr. Op. Biotechnol.* **13**, 359-366 (2002).

<sup>194</sup>Koeller, K. M., Wong, C.-H. Enzymes for chemical synthesis. *Nature* **409**, 232-240 (2001).

<sup>195</sup>Thomas, S. M., DiCosimo, R., Nagarajan, V. Biocatalysis: applications and potentials for the chemical industry. *TRENDS in Biotechnol.* **20**, 238-242 (2002).

<sup>196</sup>Bajpai, P. Application of Enzymes in the Pulp and Paper Industry. *Biotechnol. Prog.* **15**, 147-157 (1999).

<sup>197</sup>Kirk, O., Borchert, T. V., Fuglsang, C. C. Industrial enzyme applications. *Curr. Op. in Biotechnol.* **13**, 345-351 (2002).

<sup>198</sup>Schmid, A., Dordick, J. S., Hauer, B., Kiener, A., Wubbolts, M., Witholt, B. Industrial biocatalysis today and tomorrow. *Nature* **409**, 258-268 (2001).

<sup>199</sup>Gavrilescua, M., Chisti, Y. Biotechnology—a sustainable alternative for chemical industry. *Biotechnol. Adv.* **23**, 471-499 (2005).

<sup>200</sup>W. Aehle, *Enzymes in Industry - Production and Applications*, WILEY-VCH Verlag GmbH & Co. KGaA, Weinheim, 3rd edn., 2007, ch. 3, pp. 70-75.

<sup>201</sup>Bornscheuer, U. T. Immobilizing Enzymes: How to Create More Suitable Biocatalysts. *Angew. Chem. Int. Ed.* **42**, 3336-3337 (2003).

<sup>202</sup>Yiu, H. H. P., Wright, P. A. Enzymes supported on ordered mesoporous solids: a special case of an inorganic-organic hybrid. *J. Mater. Chem.* **15**, 3690-3700 (2005).

<sup>203</sup>Salis, A., Meloni, D., Ligas, S., Casula, M. F., Monduzzi, M., Solinas, V., Dumitriu, E. Physical and Chemical Adsorption of *Mucor javanicus* Lipase on SBA-15 Mesoporous Silica. Synthesis, Structural Characterization, and Activity Performance. *Langmuir* **21**, 5511-5516 (2005).

- <sup>204</sup>Svec, F. Less common applications of monoliths: I. Microscale protein mapping with proteolytic enzymes immobilized on monolithic supports. *Electrophoresis* **27**, 947-961 (2006).
- <sup>205</sup>Xu, Q., Zhu, J.-J., Hu, X.-Y. Ordered mesoporous polyaniline film as a new matrix for enzyme immobilization and biosensor construction. *Anal. Chim. Acta* **597**, 151-156 (2007).
- <sup>206</sup>Orosco, M. M., Pacholski, C., Sailor, M. J. Real-time monitoring of enzyme activity in a mesoporous silicon double layer. *Nature Nanotechnol.* **4**, 255-258 (2009).
- <sup>207</sup>Kataoka, S., Endo, A., Oyama, M., Takao, O. Enzymatic reactions inside a microreactor with a mesoporous silica catalyst support layer. *Appl. Catalysis A: General* **359**, 108-112 (2009).
- <sup>208</sup>Amblard, F., Cho, J. H., Schinazi, R. F. Cu(I)-Catalyzed Huisgen Azide-Alkyne 1,3-Dipolar Cycloaddition Reaction in Nucleoside, Nucleotide, and Oligonucleotide Chemistry. *Chem. Rev.* **109**, 4207-4220 (2009).
- <sup>209</sup>Kolb, H. C., Finn, M. G., Sharpless, K. B. Click Chemistry: Diverse Chemical Function from a Few Good Reactions. *Angew. Chem. Int. Ed.* **40**, 2005-2011 (2001).
- <sup>210</sup>Kecht, J., Bein, T. Oxidative removal of template molecules and organic functionalities in mesoporous silica nanoparticles by H<sub>2</sub>O<sub>2</sub> treatment. *Chem. Rev.* **116**, 123-130 (2008).
- <sup>211</sup>Jameson, G. W., Roberts, D. V., Adams, R. W., Kyle, W. S. A., Elmore, D. T. Determination of the operational molarity of solutions of bovine  $\alpha$ -chymotrypsin, trypsin, thrombin and factor Xa by spectrofluorimetric titration. *Biochem. J.* **131**, 107-117 (1973).
- <sup>212</sup>Yiu, H. H. P., Wright, P. A., Botting, N. P. Enzyme immobilisation using siliceous mesoporous molecular sieves. *Micro. Meso. Mater.* **44-45**, 763- (2001).
- <sup>213</sup>Lüebbe, A. S., Alexiou, C., Bergemann, C. Clinical Applications of Magnetic Drug Targeting. *J. Surgical Res.* **95**, 200-206 (2001).
- <sup>214</sup>Yamauchi, Y., Sawada, M., Noma, T., Ito, H., Furumi, S., Sakkad, Y., Kuroda, K. Orientation of mesochannels in continuous mesoporous silica films by a high magnetic field. *J. Mater. Chem.* **15**, 1137-1140 (2005).
- <sup>215</sup>Tolbert, S. H., Firouzi, A., Stucky, G. D., Chmelka, B. F. Magnetic Field Alignment of Ordered Silicate-Surfactant Composites and Mesoporous Silica. *Science* **278**, 264-268 (1997).
- <sup>216</sup>Miyata, H., Kuroda, K. Formation of a Continuous Mesoporous Silica Film with Fully Aligned Mesochannels on a Glass Substrate. *Chem. Mater.* **12**, 49-54 (2000).
- <sup>217</sup>Miyata, H., Suzuki, T., Fukuoka, A., Sawada, T., Watanabe, M., Noma, T., Takada, K., Mukaide, T., Kuroda, K. Silica films with a single-crystalline mesoporous structure. *Nat. Mater.* **3**, 651-656 (2004).
- <sup>218</sup>Midgley, P. A., Weyland, M. W., Thomas, J. M., Johnson, B. F. G. Z-Contrast tomography: a technique in three-dimensional nanostructural analysis based on Rutherford scattering. *Chem. Comm.* **10**, 907-908 (2001).
- <sup>219</sup>Yurtsever, A., Weyland, M., Muller, D. A. Three-dimensional imaging of nonspherical silicon nanoparticles embedded in silicon oxide by plasmon tomography. *Appl. Phys. Lett.* **89**, 151920 (2006).
- <sup>220</sup>Dunin-Borkowski, R. E., McCartney, M. R., Frankel, R. B., Bazylinski, D. A., Posfai, M., Buseck, P. R. Magnetic Microstructure of Magnetotactic Bacteria by Electron Holography. *Science* **282**, 1868-1870 (1998).
- <sup>221</sup>Barnard, J. S., Sharp, J., Tong, J. R., Midgley, P. A. High-Resolution Three-Dimensional Imaging of Dislocations. *Science* **313**, 319-320 (2006).
- <sup>222</sup>Sueda, S., Yoshida, K., Tanaka, N. Quantification of metallic nanoparticle morphology on TiO<sub>2</sub> using HAADF-STEM tomography. *Ultramicroscopy* **110**, 1120-1127 (2010).

<sup>223</sup>Bals, S., Van Tendeloo, G., Kisielowski, C. A New Approach for Electron Tomography: Annular Dark-Field Transmission Electron Microscopy. *Adv. Mater.* **18**, 892-895 (2006).

<sup>224</sup>Crowther, R. A., de Rosier, D. J., Klug, A. The Reconstruction of a Three-Dimensional Structure from Projections and its Application to Electron Microscopy. *Proc. Roy. Soc. Lond. A* **317**, 319-340 (1970).

<sup>225</sup>Radermacher, M., Hoppe, W. Properties of three-dimensionally reconstructed objects from projections by conical tilt compared to single axis tilting. *Proc. 7th Eur. Congr. Electron Microsc. Den Haag* **1**, 132-133 (1980).

<sup>226</sup>Weyland, M. On the Limits of High Angle Annular Dark Field (HAADF) Tomography; Electron Beam Damage. *Microsc. Microanal.* **11**, 20-21 (2005).

<sup>227</sup>Aoyama, K., Takagi, T., Hirase, A., Miyazawa, A. STEM tomography for thick biological specimens. *Ultramicroscopy* **109**, 70-80 (2008).

<sup>228</sup>Leschner, J., Biskupek, J., Chuvilin, A., Kaiser, U. Accessing the local three-dimensional structure of carbon materials sensitive to an electron beam. *Carbon* **48**, 4042-4048 (2010).

<sup>229</sup>Nickell, S., Förster, F., Linaroudis, A., Net, W. D., Beck, F., Hegerl, R., Baumeister, W., Plitzko, J. M. TOM software toolbox: acquisition and analysis for electron tomography. *J. Struct. Biol.* **149**, 227-234 (2005).

<sup>230</sup>Schweyer, F., Braunstein, P., Estournes, C., Guille, J., Kessler, H., Paillaud, J.-L., Rose, J. Metallic nanoparticles from heterometallic Co-Ru carbonyl clusters in mesoporous silica xerogels and MCM-41-type materials. *Chem. Commun.* **14**, 1271-1272 (2000).

<sup>231</sup>Kecht, J., Schloßbauer, A., Bein, T. Selective Functionalization of the Outer and Inner Surfaces in Mesoporous Silica Nanoparticles. *Chem. Mater.* **20**, 7207-7214 (2008).

<sup>232</sup>Cauda, V., Schloßbauer, A., Kecht, J., Zürner, A., Bein, T. Multiple Core-Shell Functionalized Colloidal Mesoporous Silica Nanoparticles. *J. Am. Chem. Soc.* **131**, 11361-11370 (2009).

<sup>233</sup>Howorka, S., Siwy, Z. Nanopore analytics: sensing of single molecules. *Chem. Soc. Rev.* **38**, 2360-2384 (2009).

<sup>234</sup>Wei, R., Pedone, D., Zürner, A., Döblinger, M., Rant, U. Fabrication of Metallized Nanopores in Silicon Nitride Membranes for Single-Molecule Sensing. *Small* **6**, 1406-1414 (2010).

## 9.2 Supplementary figures

### 9.2.1 Basics - 1D-XRD

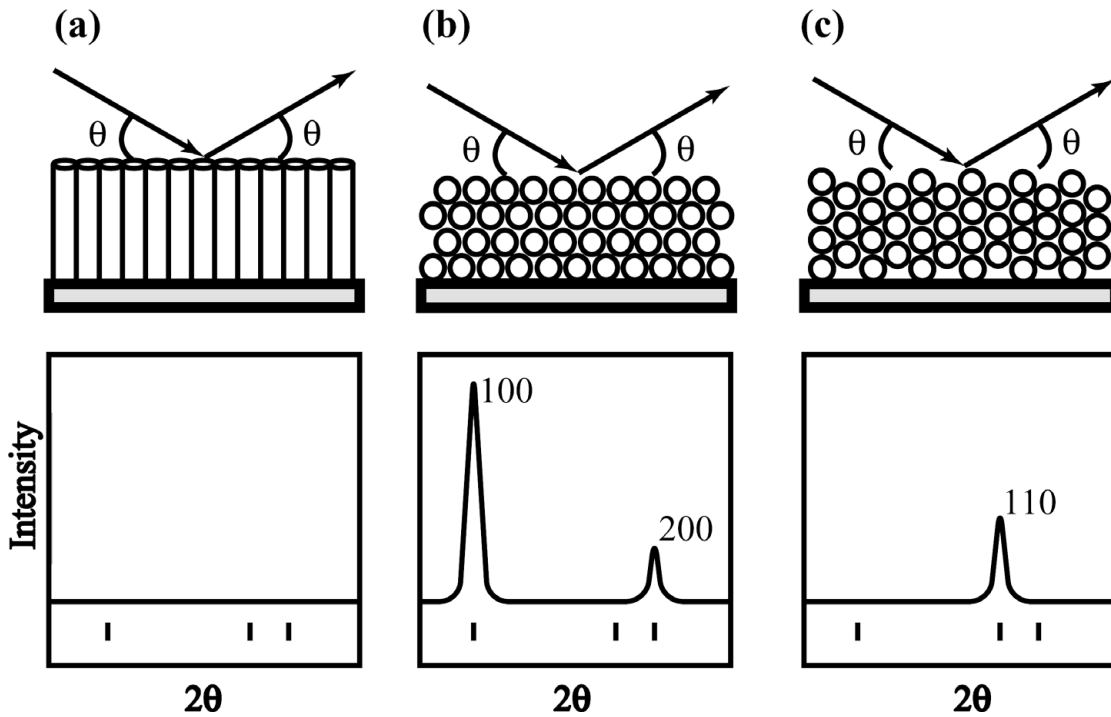


**Figure 9.1: Orientations of a  $P_6mm$  hexagonal mesophase (above) and the corresponding predicted diffraction patterns (below) for 1D-XRD.<sup>166</sup> a** Mesophase with channels oriented perpendicular to the substrate. **b** Mesophase with channels oriented parallel to the substrate with the 100 face also parallel to the surface. **c** Mesophase with channels parallel to the substrate with the 110 face parallel to the surface.

### 9.2.2 Filmthickness

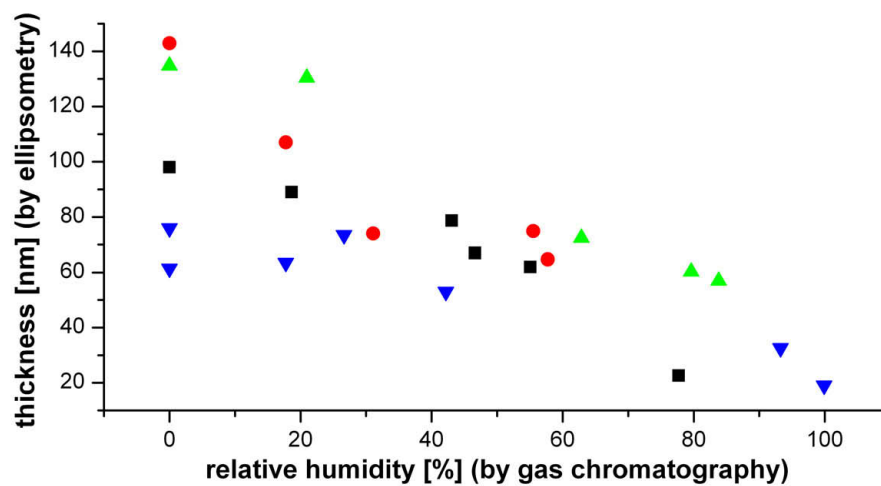


**Figure 9.2:** Thickness of mesoporous films spin coated at different humidities. Data is obtained from several experiments, indicated by different symbols. The humidity was measured by gas chromatography, calibrated with a standard hygrometer.



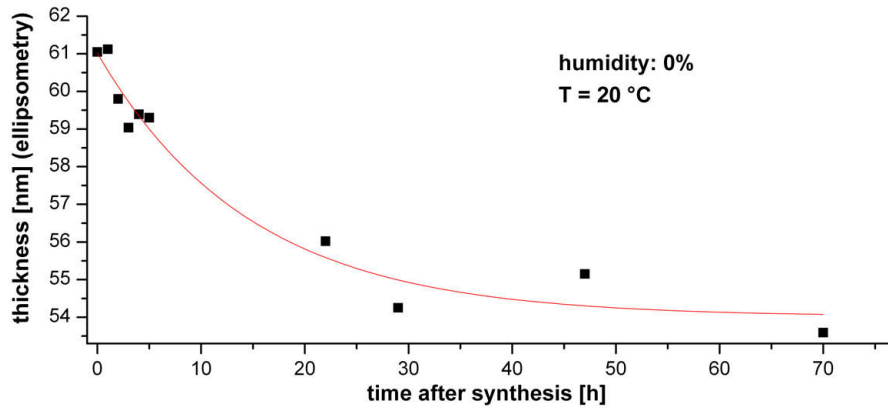


**Figure 9.3:** Film shrinkage after synthesis at room temperature measured with ellipsometry.

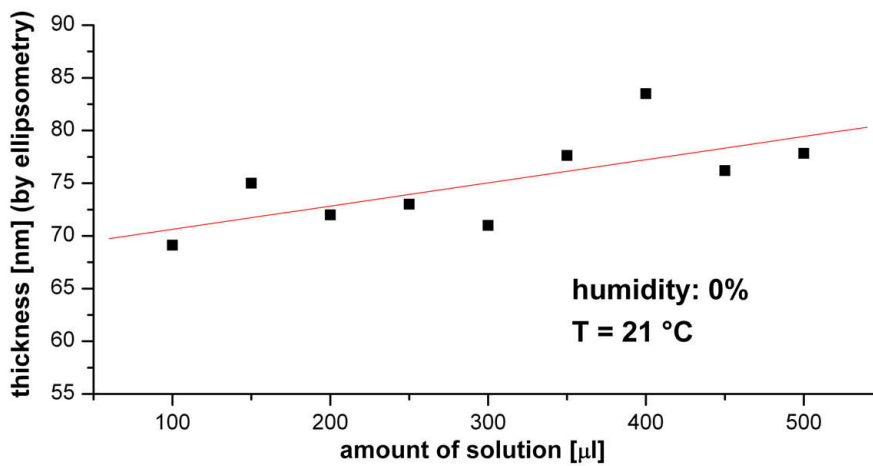


**Figure 9.4:** With higher amount of synthesis solution dropped on the substrate before spin coating, film thickness increases slightly.

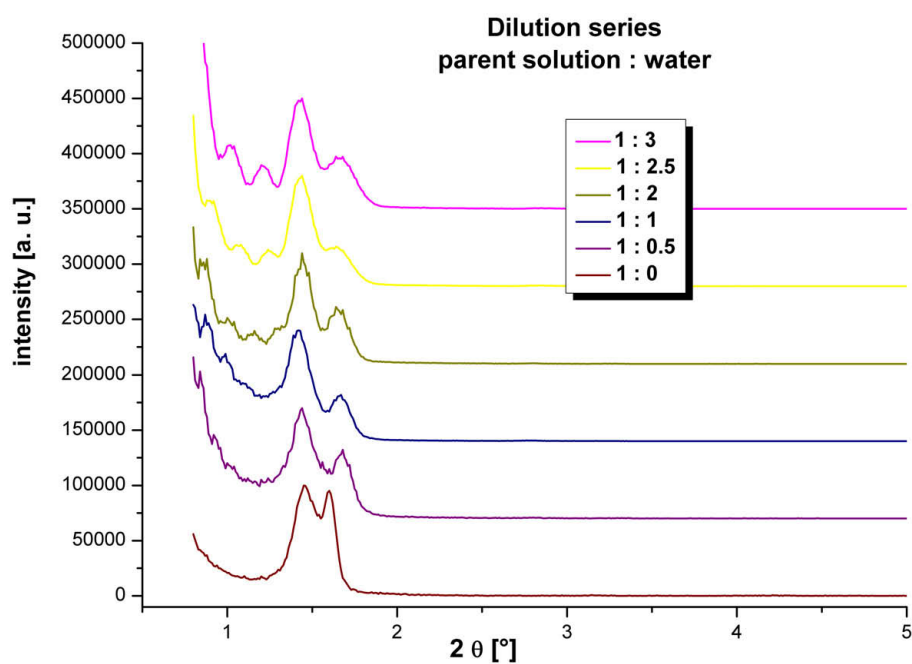


**Figure 9.5:** By dilution of the parent solution with water before spin coating the ratio lamellar to hexagonal changes in favor of the lamellar structure indicated by the decrease of reflection intensity at  $1.6^\circ 2\theta$ . Each diffractogram is shifted by 70,000 a. u. and normalized to 100,000 a. u. for the reflection at  $1.4^\circ 2\theta$ .

### 9.2.3 2D-hexagonal phase

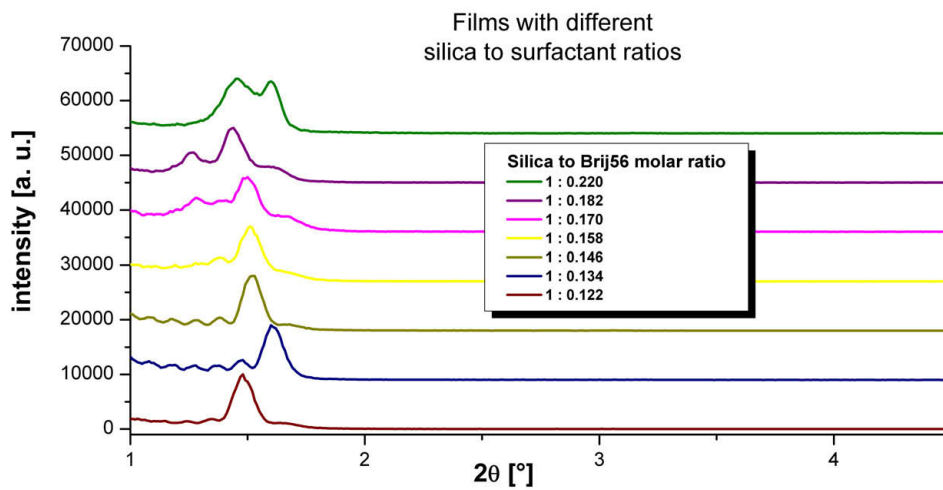


**Figure 9.6:** 1D-XRD data of films synthesized with the original recipe and with solutions containing less surfactant and more water (half the volume of original solution). By decreasing the Brij56 amount the reflection of the lamellar structure disappears - pure 2D hexagonal phases are obtained. All graphs were normalized to 10,000 a. u. for the highest reflection intensity and each diffractogram is shifted by 9,000 a. u.

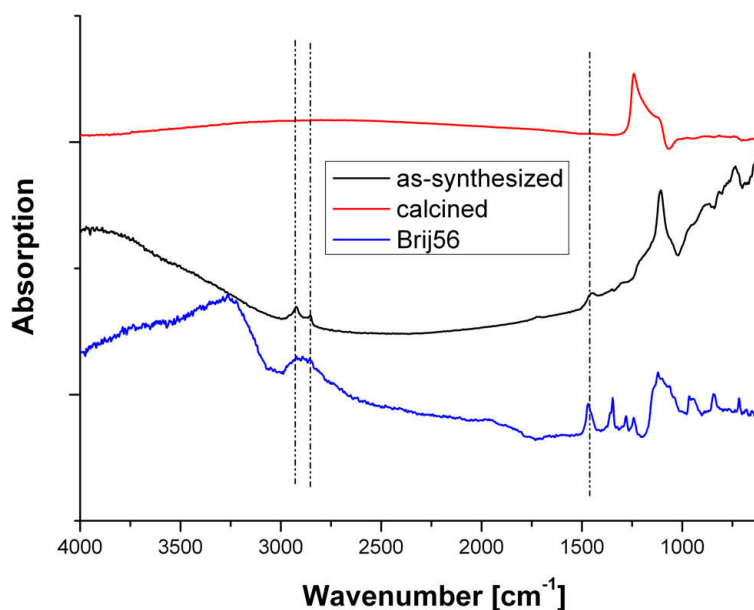


**Figure 9.7:** Infrared spectra of as-synthesized and calcined 2D-hexagonal films in comparison to the spectrum of Brij56. Some typical C-H stretching and bending vibrations of Brij56 are also visible in the as-synthesized film. After calcination these vibrations are not detectable any more.

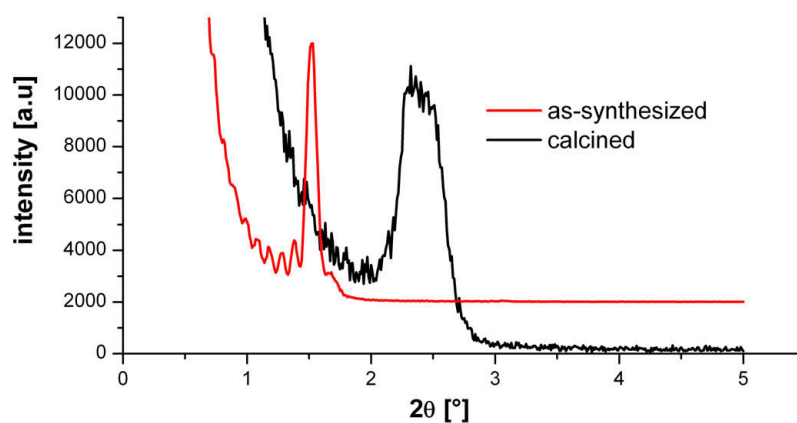


**Figure 9.8:** 1D-XRD patterns of the as-synthesized and the calcined 2D-hexagonal film. The reflection shift indicates a film shrinkage perpendicular to the surface of about 35 %.

### 9.2.4 Cubic phase

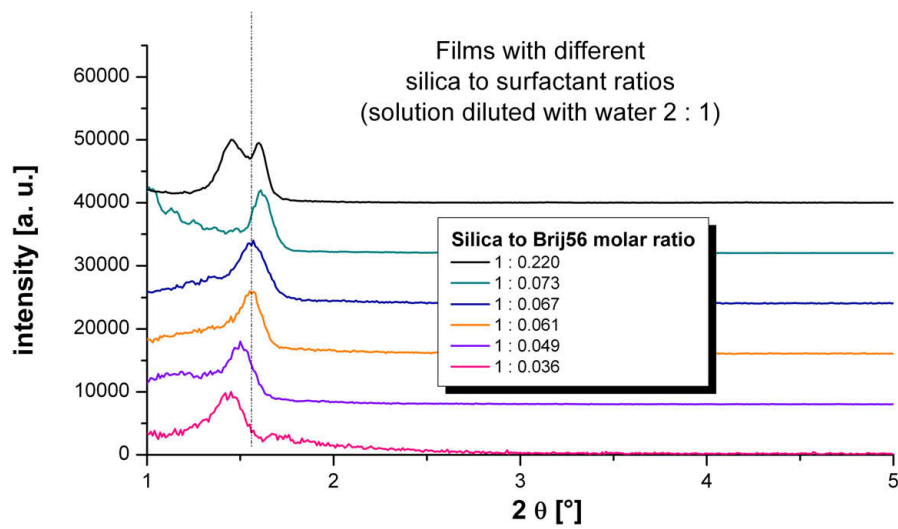


**Figure 9.9:** 1D-XRD data of films synthesized with the original recipe and with solutions containing less surfactant and more water (half the volume of original solution). A significant reflection shift indicating a structural change is not visible. All graphs were normalized to 10,000 a. u. for the highest reflection intensity and each diffractogram is shifted by 8,000 a. u.



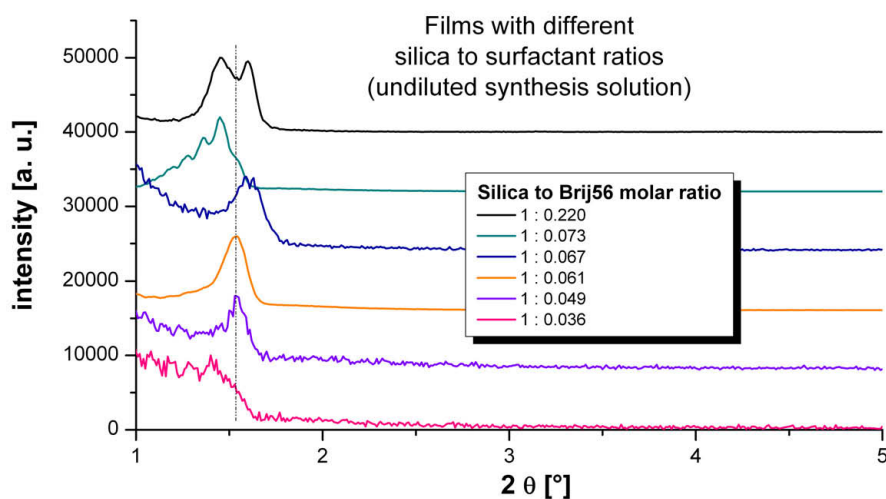


**Figure 9.10:** 1D-XRD data of films synthesized with the original recipe and with solutions containing less surfactant. The best signal to noise ratio is obtained at a surfactant to silica ratio of 0.061. All graphs were normalized to 10,000 a. u. for the highest reflection intensity and each diffractogram is shifted by 8,000 a. u.

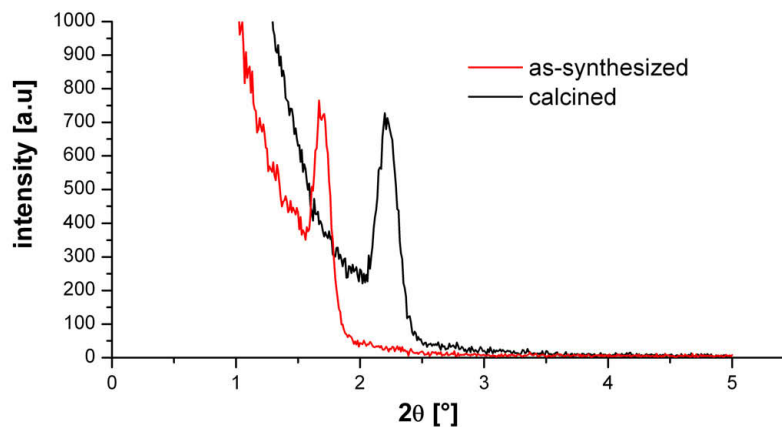


**Figure 9.11:** 1D-XRD patterns of a as-synthesized and calcined cubic film, respectively. The reflection shift indicates a film shrinkage perpendicular to the surface of about 24 %.

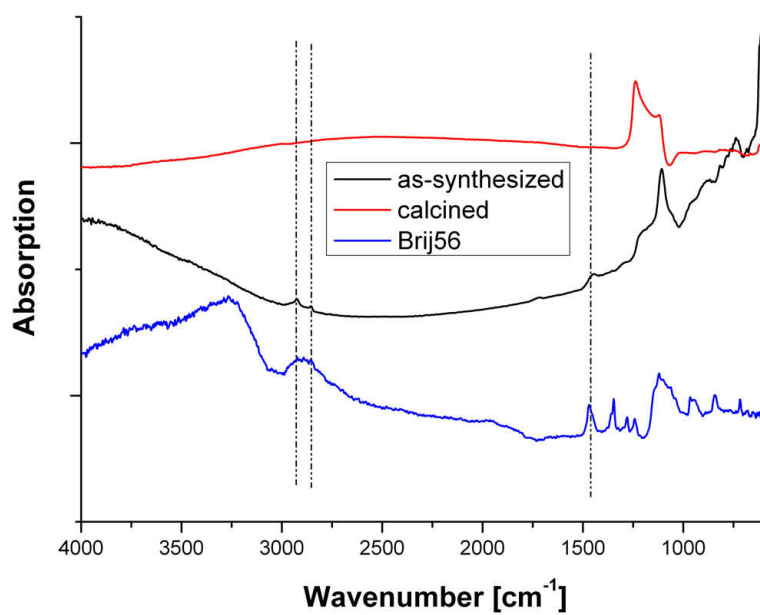


**Figure 9.12:** Infrared spectra of as-synthesized and calcined cubic films in comparison to the spectrum of Brij56. Some typical C-H stretching and bending vibrations of Brij56 are also visible in the as-synthesized film. After calcination these vibrations are not detectable any more.

### 9.2.5 Lamellar phase

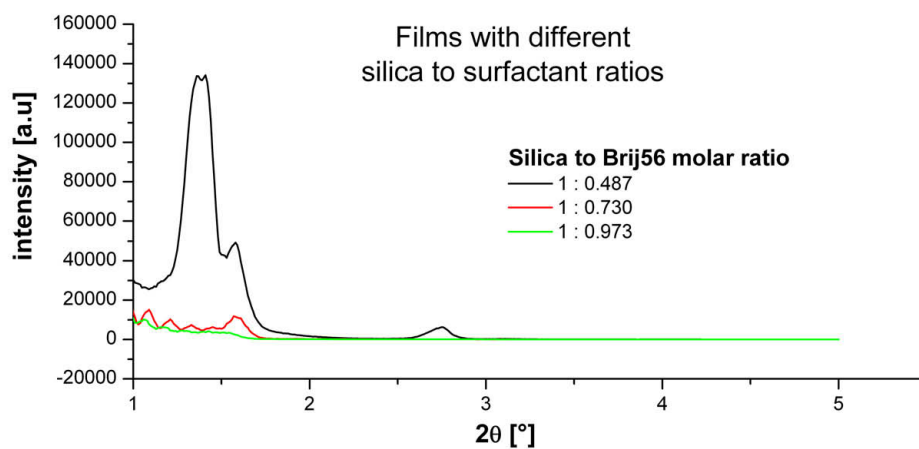


**Figure 9.13:** By dilution a pure lamellar phase is obtained. But with increasing surfactant amount the structure is getting worse. At a molar ratio (silica to template) of 1 : 0.487 the structure still seems to be highly ordered.

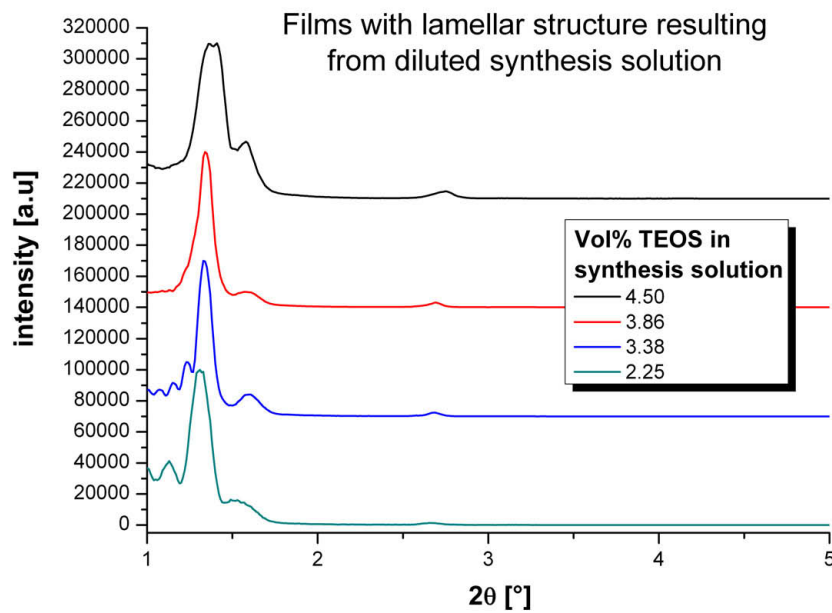


**Figure 9.14:** Dilution series of mesoporous films synthesized with a surfactant to silica ratio of 1 : 0.487. The main reflection is slightly shifting to lower angles at lower TEOS concentrations indicating a thicker layer of amorphous SiO<sub>2</sub>. Each diffractogram is shifted by 70,000 a. u. and normalized to 100,000 a. u. for the highest reflection intensity.

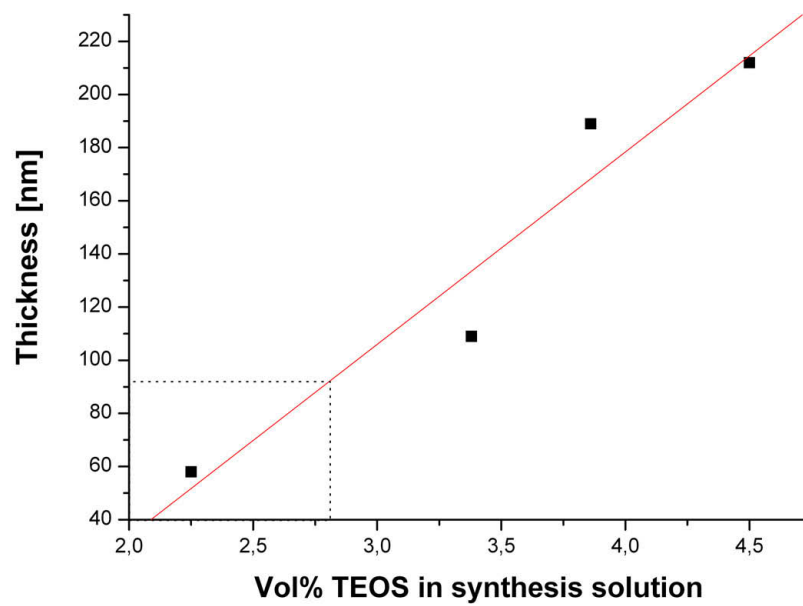


**Figure 9.15:** Dilution series of mesoporous films synthesized with a surfactant to silica ratio of 1 : 0.487. There is a direct correlation between the amount of TEOS in the synthesis solution and the thickness of the resulting mesostructured films.



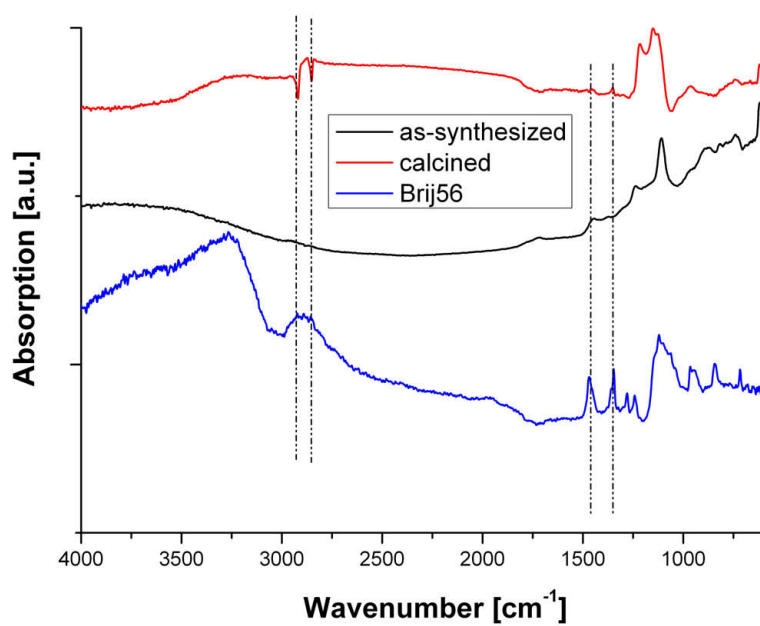


**Figure 9.16:** Infrared spectra of as-synthesized and calcined lamellar films in comparison to the spectrum of Brij56. Some typical C-H stretching and bending vibrations of Brij56 are also visible in the as-synthesized film. After calcination these vibrations are only weakly detectable.

### 9.3 Supplementary tables

Map (mean deviation)	X Position TEM (nm)	Y Position TEM (nm)	X Position widefield (nm)	Y Position widefield (nm)	Deviation (nm)
Map 8 (15.02 nm)	1082.47	2042.41	1073.13	2032.54	13.59
	1943.77	1317.64	1931.28	1329.86	17.48
	157.18	2843.63	158.37	2833.69	10.01
	1560.88	529.27	1556.52	537.17	9.02
	2742.11	2297.69	2767.11	2297.39	25.01
Map 10 (47.84 nm)	302.01	1128.98	322.51	1081.04	52.14
	3450.15	871.82	3409.50	873.23	40.67
	1362.03	3278.76	1382.17	3325.29	50.70
Map 11 (33.77 nm)	3517.62	3369.95	3530.17	3389.88	23.55
	1388.64	1914.38	1377.29	1958.71	45.76
	2242.05	3392.85	2235.12	3344.06	49.28
	1334.05	796.52	1339.77	781.06	16.489
Map 12 (26.15 nm)	1680.29	1780.52	1698.29	1813.65	37.71
	2668.13	2982.96	2675.41	2977.05	9.38
	1660.17	1129.70	1637.22	1136.09	23.82
	801.55	1829.53	799.22	1795.92	33.69
Map 13 (20.17 nm)	2318.42	2251.67	2300.48	2267.53	23.95
	2933.93	2619.05	2944.50	2634.09	18.39
	2283.05	1108.95	2289.39	1101.35	9.90
	3347.34	505.14	3326.55	492.58	24.29
	800.85	1333.16	822.67	1322.42	24.32

**Table 9: Mean deviation of overlay.** The table shows the bead positions in the TEM images and in wide-field tracking data before and after the overlay procedure. A mean deviation down to 15 nm was achieved (Map 8).

Surfactant amount	Silica amount	Structure	relative humidity
1.4 g	2 g	lamellar	—
1.16 g	2 g	2D hexagonal	—
0.91 g	2 g	2D hexagonal	low
0.91 g	2 g	cubic	high

**Table 10: The influence of the silica to surfactant ratio on the film structure.** The same tendency as in section 4.2 could be obtained. A high surfactant amount results in lamellar films. With a reduced amount of template 2D hexagonal films are synthesized and by variation of the relative humidity during synthesis even a cubic framework could be observed.

## 9.4 Program code

### 9.4.1 Determining the center of PS-beads in TEM maps

```

//*****
//Variablen festlegen//
//*****
number pi, top, left, bottom, right, Breite, Hoehe, Winkel, countx, county
number AnzPunkte, AnzPunkte2, maxdiff, maxvar, radius, maxrad, radstart, radsprung, seite
number xstart, xsprung, ystart, ysprung, minx, miny
image temp, img, Ergeb, bild, bild2, maximage, kreis, innen, Kreuz
pi = 3.1415926535897932384626433832795

//*****
//Auswählen des Frontimages//
//*****
if( !GetFrontImage(img) )
{
    OkDialog("You must have an image to operate on!")
    exit(0)
}

//*****
//Beginn der Schleife/Auswahl der Bereiche//
//*****
GetSelection(img,top,left,bottom,right) // uses whole image rectangle if no selection is present
Breite = right-left
Hoehe = bottom-top
temp := img[top,left,bottom,right]
Ergeb := ReallImage("Ergebnis", 4, Breite, Hoehe)
showimage(temp)
maxdiff=256; maxvar=20000
if (Breite>=Hoehe) seite=Hoehe
if (Breite<Hoehe) seite=Breite
maxrad = seite/3; minx = Breite/2; miny = Hoehe/2
radsprung = seite/25; xsprung = Breite/25; ysprung = Hoehe/25

while (abs(radstart-maxrad)>=0.1 || abs(xstart-minx)>=0.1 || abs(ystart-miny)>=0.1)
{
    radsprung = radsprung/4; radstart = maxrad
    xsprung = xsprung/4; xstart = minx
    ysprung = ysprung/4; ystart = miny

for (radius=radstart-radsprung*10; radius<=radstart+radsprung*10; radius=radius+radsprung)
{
    kreis = tert (sqrt((icol-xstart)*(icol-xstart)+(irow-ystart)*(irow-ystart))<radius+10 && sqrt((icol-xstart)
        *(icol-xstart)+(irow-ystart)*(irow-ystart))>radius-10, temp, 0)
    bild = tert (kreis>0.1,0)
    AnzPunkte = mean(bild)*Hoehe*Breite
    //result ("nRadius(Pythagoras): "+xstart+" "+ystart)
    //result ("nRadius: "+radius+" Variance: "+variance(kreis))
    if (sum(kreis)/AnzPunkte < maxdiff && variance(kreis)<maxvar)
    {
        maximage = kreis
        maxdiff = sum(kreis)/AnzPunkte
        maxrad = radius
        maxvar = variance(kreis)
    }
}

for (countx=xstart-xsprung*5; countx<=xstart+xsprung*5; countx=countx+xsprung)
{
    for (county=ystart-ysprung*5; county<=ystart+ysprung*5; county=county+ysprung)
    {
        kreis = tert (sqrt((icol-countx)*(icol-countx)+(irow-county)*(irow-county))<maxrad+10 && sqrt((icol-
            countx)*(icol-countx)+(irow-county)*(irow-county))>maxrad-10, temp, 0)
        bild = tert (kreis>0.1,0)
        AnzPunkte = mean(bild)*Hoehe*Breite
        //result ("n: "+countx+" y: "+county+" Variance: "+variance(kreis))
    }
}

```

```

    if (sum(kreis)/AnzPunkte < maxdiff && variance(kreis)<maxvar)
    {
        maximage = kreis
        minx = countx; miny = county
        maxvar = variance(kreis)
    }
}
}

result (" \nBreite:_" + Breite + "_Hoche:_" + Hoeh)
result (" \nRadius:_" + maxrad + "_minx:_" + minx + "_miny:_" + miny)
result (" \nGesamt:_" + (left + minx) + "_Gesamt:_" + (top + miny))

Kreuz := temp[miny-20,minx-20,miny+20,minx+20]
Kreuz = tert((icol<irow+2 && icol>irow-2) || (40-icol<irow+2 && 40-icol>irow-2), 1, Kreuz)
img[top+ystart-20,left+xstart-20,top+ystart+20,left+xstart+20] = Kreuz

```

## 9.4.2 Calculating the FFT directors of TEM maps

```

//*****
//Variablen festlegen//
//*****
number top, left, bottom, right, ntx, nty, countx, county, Breite, Hoeh, verhalt
number centery, centerx, xval, yval, countx2, county2, zahl, schnitt, summe
number maxmean, maxx, maxy, steigung, YAbschnitt, pi, bildersahl, Anzahl
image temp, testimage, bild, maximage, richtung, img2, img, Ergeb
centerx = 128; centery = 128; xval=0; yval=0; pi = 3.1415926535897932384626433832795

//*****
//Auswählen des Frontimages//
//*****
Anzahl = 4
for (bildersahl=0; bildersahl<Anzahl; bildersahl++)
{
    GetFrontImage(img)
    GetSize(img, Breite, Hoeh);
    Ergeb := ReallImage("FFT_of_" + GetName(img), 4, Breite, Hoeh)
    Ergeb = 1
}

//*****
//Beginn der Schleife/Auswahl der Bereiche//
//*****
for (countx=0; countx<(Hoeh/128)-1; countx++)
{
    for (county=0; county<(Breite/128)-1; county++)
    {
        result (" \nBild_" + (bildersahl+1) + "_von_" + Anzahl + "_Bearbeite_Ausschnitt_" + (((Breite/128)-1)*countx+
            county+1) + "_von_" + (((Breite/128)-1)*((Hoeh/128)-1)))
        ntx = countx*128
        nty = county*128

        SetSelection(img, ntx, nty, ntx+256, nty+256)
        GetSelection(img, top, left, bottom, right) // uses whole image rectangle if no selection is present

        number sizeX = right - left
        number sizeY = bottom - top

        image windowedImg := CreateFloatImage("", sizeX, sizeY)
        windowedImg = ( 1-cos(2*pi()*icol/sizeX) ) * ( 1-cos(2*pi()*irow/sizeY) ) * (img[] - average(img[]))

        compleximage diffractogram := PackedFFT(windowedImg)

        SetName(diffractogram, "Diffractogram")

        //*****
        //Acquiring the foremost image and obtaining the centre location//
        //*****
        GetNumberNote(diffractogram, "Diffraction_Package:Center:X", centerx )
    }
}

```



```

GetNumberNote(diffractogram, "Diffraction_Package:Center:Y", centery)

//*****
//Warping the image to obtaining the linear projection of the data //
//*****
temp := modulus( diffractogram ) //Macht Absolutwerte aus den imaginären Zahlen
zahl=0; schnitt=0; maxmean = 0

//*****
//Suche nach dem Maximum//
//*****
number kleiner = 42
number groesser = 34

bild = tert (iradius<kleiner && iradius>groesser, temp, 0)

for (countx2=127-kleiner; countx2<129+kleiner; countx2++)
{
    for (county2=127-kleiner; county2<129+kleiner; county2++)
    {
        if (max(bild[countx2, county2]) > 0)
        {
            testimage := RealImage( "test", 4, 5, 5 )
            testimage = temp[countx2-2+icol, county2-2+irow]
            zahl++
            if (mean(testimage)>maxmean)
            {
                maximage = testimage
                maxmean = mean(testimage)
                maxx = countx2
                maxy = county2
            }
        }
    }
}

//*****
//Zeichnen des Balkens//
//*****
verhalt = maxmean/(sum(bild)/zahl)
steigung = (maxx-128.001)/(maxy-128.001)*(-1)
YAbschnitt = 64-(steigung*64)
result ("MAXX:_" + maxx + "_MAXY:_" + maxy + "_Verhältnis:_" + verhalt + "_Steigung:_" + steigung)
if (verhalt>1.5)
{
    Ergeb[ntx+64, nty+64, ntx+192, nty+192] = tert (irow <= steigung*icol+YAbschnitt+(sqrt(1+
    steigung*steigung)*verhalt) && irow >= steigung*icol+YAbschnitt-(sqrt(1+steigung*
    steigung)*verhalt) && iradius<40, 0, Ergeb[ntx+64, nty+64, ntx+192, nty+192])
}
}

//*****
//Ausgabe des fertigen Bildes//
//*****
showimage(Ergeb)
hideimage(Ergeb)
hideimage(img)
}

```

### 9.4.3 Calculating scaling, rotation and translation of optical images with respect to the TEM map

```

<html>
<head>
</head>
<body>
<?php
$n1 = chr(13) . chr(10);

```

```

$tab = chr(9);

//These are the starting parameters and were adjusted for each calculation
$Verkfaktor = 6912; //reduction factor
$BerXlo = "0"/$Verkfaktor; //X-Koordinate der linken oberen Ecke des zu betrachtenden Ausschnitts (Photoshop –
    Ursprung ist links oben)
$BerYlo = "0"/$Verkfaktor; //X-Koordinate der linken oberen Ecke des zu betrachtenden Ausschnitts (Photoshop –
    Ursprung ist links oben)
$BerGrX = "6912"/$Verkfaktor; //Breite in Pixeln des Bereichs (geteilt durch $Verkfaktor muss vielfaches von 8
    sein -> mpj)
$BerGrY = "6912"/$Verkfaktor; //Höhe in Pixeln des Bereichs (geteilt durch $Verkfaktor muss vielfaches von 8 sein
    -> mpj)

$ITEMGRX = "6912"/$Verkfaktor; //Breite TEM-Bild in Pixeln
$ITEMGRY = "6912"/$Verkfaktor; //Höhe TEM-Bild in Pixeln
$AITEMGRX = "6912"/$Verkfaktor; //Breite TEM-Bild im Adobe Illustrator
$AITEMGRY = "6912"/$Verkfaktor; //Höhe TEM-Bild im Adobe Illustrator
$AITEMX = "3456"/$Verkfaktor; //X-Position TEM-Bild im Adobe Illustrator
$AITEMY = "3456"/$Verkfaktor; //Y-Position TEM-Bild im Adobe Illustrator

$TRANSX1 = "48"; //erster X-Wert der Skala im Trajektorien-PS
$TRANSX2 = "92"; //letzter X-Wert der Skala im Trajektorien-PS
$TRANSY1 = "115"; //erster Y-Wert der Skala im Trajektorien-PS
$TRANSY2 = "152"; //letzter Y-Wert der Skala im Trajektorien-PS
$AITRANSGRX = "44"; //Breite des Trajektorien-PS im Adobe Illustrator (nur Rahmen!)
$AITRANSGRY = "37"; //Höhe des Trajektorien-PS im Adobe Illustrator (nur Rahmen!)
$AITRANSX = "0"; //X-Position des Trajektorien-PS im Adobe Illustrator (nur Rahmen!)
$AITRANSY = "0"; //Y-Position des Trajektorien-PS im Adobe Illustrator (nur Rahmen!)

//PS bead positions in TEM map (in pixel)
$ITEM = array(
    array("x"=>"582.8759"/$Verkfaktor, "y"=>"5245.0715"/$Verkfaktor),
    array("x"=>"6658.792"/$Verkfaktor, "y"=>"5741.3805"/$Verkfaktor),
    array("x"=>"2628.72"/$Verkfaktor, "y"=>"1096"/$Verkfaktor)
);

//PS bead positions in optical im image (in pixel)
$TRANS = array(
    array("x"=>"78.567", "y"=>"148.28"),
    array("x"=>"55.575", "y"=>"139.47"),
    array("x"=>"78.409", "y"=>"128.53")
);

$AnzTEM = count($ITEM); //number of PS beads in TEM map
$AnzTRANS = count($TRANS); //number of PS beads in optical image

//Verification if in both images are the same number of PS beads
if ($AnzTEM<$AnzTRANS)
{
    $Anzahl = $AnzTEM;
}
else
{
    $Anzahl = $AnzTRANS;
}
echo ("Anzahl_der_Punkte:␣.$Anzahl.<br>");

//Recalculation of positions for overlay in Adobe Illustrator
for ($xyz=0; $xyz<$Anzahl; $xyz++)
{
    $ITEM[$xyz]["x"] = ($ITEM[$xyz]["x"]*$AITEMGRX)/$ITEMGRX + $AITEMX - $AITEMGRX/2;
    $ITEM[$xyz]["y"] = (($ITEMGRY-$ITEM[$xyz]["y"])*$AITEMGRY)/$ITEMGRY + $AITEMY - $AITEMGRY/2;
    $TRANS[$xyz]["x"] = (($TRANS[$xyz]["x"]-$TRANSX1)*$AITRANSGRX)/($TRANSX2-$TRANSX1) + $AITRANSX - $AITRANSGRX/2;
    $TRANS[$xyz]["y"] = (($TRANS[$xyz]["y"]-$TRANSY1)*$AITRANSGRY)/($TRANSY2-$TRANSY1) + $AITRANSY - $AITRANSGRY/2;
}

//Calculation of scaling and rotation angle
$lop=0;
for ($xyz=0; $xyz<$Anzahl; $xyz++)
{

```

```

for ($abc=$xyz+1; $abc<$Anzahl; $abc++)
{
    $xdiffTEM = $TEM[$xyz][ "x" ]-$TEM[$abc][ "x" ];
    $ydiffTEM = $TEM[$xyz][ "y" ]-$TEM[$abc][ "y" ];
    $xdiffTRANS = $TRANS[$xyz][ "x" ]-$TRANS[$abc][ "x" ];
    $ydiffTRANS = $TRANS[$xyz][ "y" ]-$TRANS[$abc][ "y" ];

    $LaengeTEM = sqrt(( $xdiffTEM*$xdiffTEM)+($ydiffTEM*$ydiffTEM));
    $LaengeTRANS = sqrt(( $xdiffTRANS*$xdiffTRANS)+($ydiffTRANS*$ydiffTRANS));
    $Verh[$iop] = $LaengeTEM/$LaengeTRANS;

    if ($xdiffTEM<0)
    {
        $WinkelTEM = M_PI+(atan($ydiffTEM/$xdiffTEM));
    }
    else
    {
        $WinkelTEM = (atan($ydiffTEM/$xdiffTEM));
    }
    if ($xdiffTRANS<0)
    {
        $WinkelTRANS = M_PI+(atan($ydiffTRANS/$xdiffTRANS));
    }
    else
    {
        $WinkelTRANS = (atan($ydiffTRANS/$xdiffTRANS));
    }
    $Winkel[$iop] = $WinkelTEM - $WinkelTRANS;
    if ($Winkel[$iop]<(-1)*M_PI) $Winkel[$iop] = 2*M_PI + $Winkel[$iop];
    $iop++;
}

//Calculating the mean values of scaling and rotation
for ($xyz=0; $xyz<count($Verh); $xyz++)
{
    $Ges=$Verh[$xyz]+$Ges;
    $Ges2=$Winkel[$xyz]+$Ges2;
}
$Skala=$Ges/count($Verh);
$Drehung=$Ges2/count($Winkel);
echo ("<br>Mittelwert-Skalierung:_" . $Skala);
echo ("<br>Mittelwert-Drehung:_" . $Drehung*180/M_PI);

//Setting the position of one PS bead equal in optical and TEM image
$TRANSNEU[0][ "x" ] = $TEM[0][ "x" ];
$TRANSNEU[0][ "y" ] = $TEM[0][ "y" ];

//Calculating new positions for the beads in optical image using scaling and rotation from above
for ($xyz=1; $xyz<count($TRANS); $xyz++)
{
    $xdiffTRANS = $TRANS[$xyz][ "x" ]-$TRANS[0][ "x" ];
    $ydiffTRANS = $TRANS[$xyz][ "y" ]-$TRANS[0][ "y" ];
    $LaengeTRANS = sqrt(( $xdiffTRANS*$xdiffTRANS)+($ydiffTRANS*$ydiffTRANS));
    if ($xdiffTRANS<0)
    {
        $WinkelTRANS = M_PI+(atan($ydiffTRANS/$xdiffTRANS));
    }
    else
    {
        $WinkelTRANS = (atan($ydiffTRANS/$xdiffTRANS));
    }
    $WinkelNEU = $WinkelTRANS+$Drehung;
    $TRANSNEU[$xyz][ "x" ] = $TRANSNEU[0][ "x" ]+$Skala*$LaengeTRANS*cos($WinkelNEU);
    $TRANSNEU[$xyz][ "y" ] = $TRANSNEU[0][ "y" ]+$Skala*$LaengeTRANS*sin($WinkelNEU);
}

//Iterative method for calculating offset of optical image
$deltax = 0; $deltay = 0; $zahl=0;

```

```

do {
  $SUMX = 0; $SUMY = 0;

  for ($xyz=0; $xyz<count($TRANSNEU); $xyz++)
  {
    $SUMX = $TEM[$xyz]["x"] - $TRANSNEU[$xyz]["x"] + $SUMX;
    $SUMY = $TEM[$xyz]["y"] - $TRANSNEU[$xyz]["y"] + $SUMY;

    $deltax = $SUMX/(count($TRANSNEU)*2);
    $deltay = $SUMY/(count($TRANSNEU)*2);
  }

  $zahl++;

  for ($xyz=0; $xyz<count($TRANSNEU); $xyz++)
  {
    $TRANSNEU[$xyz]["x"] = $TRANSNEU[$xyz]["x"] + $deltax;
    $TRANSNEU[$xyz]["y"] = $TRANSNEU[$xyz]["y"] + $deltay;
  }
} while ((abs($deltax)>0.0001 or abs($deltay)>0.0001) && $zahl<10000);

//Output calculated positions for optical image in Adobe Illustrator
echo "<br><b>neuTRANS: </b>";
print_r ($TRANSNEU);
echo "<br><b>TEM: </b>";
print_r ($TEM);
echo "<br><b>wie oft?: </b>". $zahl);





//Calculating overlay error
$SUM = 0;
for ($xyz=0; $xyz<count($TRANSNEU); $xyz++)
{
  $SUM = sqrt (($TEM[$xyz]["x"] - $TRANSNEU[$xyz]["x"]) * ($TEM[$xyz]["x"] - $TRANSNEU[$xyz]["x"]) + ($TEM[$xyz]["y"] - $TRANSNEU[$xyz]["y"]) * ($TEM[$xyz]["y"] - $TRANSNEU[$xyz]["y"])) + $SUM;
}
echo "<br><b>SUM_bis_jetzt: </b>". $SUM. " " . count($TRANSNEU));
}
$fehler = ($SUM/count($TRANSNEU))*(100/193)*$Verklfaktor;
echo "<br><b>mittlerer_Fehler: </b>". $fehler. 'µm';

?>

</body>
</html>

```

## 9.5 CD content

	<b>(CD):\</b>
thesis.pdf	The thesis itself.
	<b>(CD):\additional_artwork\</b>
image1.png	Artwork of a silica mesopore.
image2.png	Logo of the 22nd german zeolite days, Munich.
image3.png	Artwork of DNA traversing a SiN nanopore - image used for small cover 13/2010
	<b>(CD):\images\</b>
	All illustrations used for this thesis.
	<b>(CD):\movies\</b>
movie1.mpg	This file contains Supplementary Movie 1 which is a wide-field movie of fluorescent dye molecules diffusing through the porous system. Temporal resolution: 200 ms per frame. Animation with 5× real time.
movie2.mpg	This file contains Supplementary Movie 2 which shows the animation of the single particle trajectory superimposed with the porous structure from TEM (see figure 4.11). The molecule clearly diffuses along the porous structure. Animation with 2× real time.
movie3.mpg	This file contains Supplementary Movie 3 which shows the animation of the single particle trajectory superimposed with the porous structure from TEM (see figure 4.12). The molecule clearly diffuses along the porous structure and bounces back at domain boundaries. Animation with 2x real time.
movie4.avi	Mesoporous silica thin film - template extracted and loaded with TDI molecules. The sample is characterized by wide-field microscopy at 100× magnification in an EtOH saturated atmosphere. Temporal resolution 500 ms per frame. Animation with 12.5× real time.

	<b>(CD):\movies\ movie5.avi</b>	3D rendered volume (Amira) showing the distribution of gold nanoclusters within the pores of a colloidal mesoporous silica particle. The silica is illustrated as semi-transparent material.
	<b>movie6.avi</b>	3D rendered volume (Amira) only showing the gold nanoclusters within the pores of a colloidal mesoporous silica particle. The silica is not visible.
	<b>movie7.avi</b>	3D rendered volume (Amira) showing a nanopore in a SiN membrane.
	<b>movie8.avi</b>	3D rendered volume (Amira) showing the thin gold layer on top of a SiN nanopore.
	<b>movie9.mpg</b>	Animation of a rotating silica nanopore.
	<b>movie10.mpg</b>	Movie showing the assembly of an intelligent drug delivery system based on colloidal mesoporous silica.

	<b>(CD):\presentations\ present1.ppt</b>	Oral presentation, german zeolite days 2008, Halle.
	<b>movie1.mpg</b>	Movie for present1.ppt.
	<b>movie2.mpg</b>	Movie for present1.ppt.
	<b>movie3.mpg</b>	Movie for present1.ppt.
	<b>movie4.mpg</b>	Movie for present1.ppt.
	<b>movie5.mpg</b>	Movie for present1.ppt.
	<b>poster1.pdf</b>	Poster presentation, summarizing Workshop (SFB 486), Venice.
	<b>poster2.pdf</b>	Poster presentation, nanoday 2009, Munich



## 9.6 List of abbreviations

**1D** one dimensional

**2D** two-dimensional

**2D-GISAXS** 2D Grazing Incidence SAXS

**3D** three-dimensional

**Å** Ångström,  $1 \text{ Å} = 10^{-10} \text{ m}$

**AFM** Atomic Force Microscopy

**ART** Algebraic Reconstruction Technique

**BMBF** German federal ministry of education and research, Bundesministerium für Bildung und Forschung

**CCD** Charged Coupled Device

**CI-TEOS** (3-Chloropropyl)triethoxysilane

**CTAB** Cetyl Trimethyl Ammonium Bromide

**CMS** Colloidal Mesoporous Silica

**COF** Covalent Organic Framework

**CSA** Cooperative Self-Assembly

**CT** Computed Tomography, Computertomographie

**DART** Discrete Algebraic Reconstruction Technique

**DMF** DiMethyl Formamide

**DT** Discrete Tomography

**DSC** Differential Scanning Calorimetry

**e.g.** for example

**EDC** 1-Ethyl-3-(3-Dimethylaminopropyl) Carbodiimide

**EISA** Evaporation-Induced Self-Assembly

**EM** Electron Microscopy

**EM-CCD** Electron Multiplying CCD

**ET** Electron Tomography

**etc.** et cetera

**FBP** Filtered BackProjection

**FCS** Fluorescence Correlation Spectroscopy

- FFT** Fast Fourier Transformation
- FRAP** Fluorescence Recovery After Photobleaching
- FRET** Förster Resonance Energy Transfer
- FSM** Folded-Sheet Mesoporous material
- FTIR** Fourier Transform IR
- HAADF** High Angle Annular Dark Field
- HRTEM** High Resolution TEM
- IR** InfraRed spectroscopy
- IRM** Imagerie par Résonance Magnétique
- LED** Light Emitting Diode
- MCM** Mobil Composition of Matter
- MES** 2-(N-Morpholino) EthaneSulfonic acid
- MOF** Metal Organic Framework
- MRI** Magnetic Resonance Imaging
- MRT** Magnetresonanztomographie
- MuGB** 4 Methylumbelliferyl-4 GuanidinoBenzoate hydrochloride hydrate
- NA** Numerical Aperture
- nm** nanometer
- NMR** Nuclear Magnetic Resonance spectroscopy
- PBS** Phosphate Buffered Saline
- PFG-NMR** Pulsed-Field Gradient NMR spectroscopy
- PMO** Periodic Mesoporous Organosilica
- PS** PolyStyrol
- RAIR** Reflection Absorption IR
- r. h.** relative humidity
- SBA** Santa Barbara Amorphous type material
- SART** Simultaneous Algebraic Reconstruction Technique
- SAXS** Small Angle X-ray Scattering
- SEM** Scanning Electron Microscopy
- SIRT** Simultaneous Iterative Reconstruction Technique

- SPT** Single Particle Tracking
- STED** STimulated Emission Depletion
- STEM** Scanning Transmission Electron Microscopy
- SMM** Single Molecule Microscopy
- SMT** Single Molecule Tracking
- sp-functionalization** triple bond functionalization
- STM** Scanning Tunneling Microscopy
- TDI** Terrylen Dilmide
- TEM** Transmission Electron Microscopy
- TEOS** Tetra Ethyl Ortho Silicate
- TMOS** Tetra Methyl Ortho Silicate
- TGA** ThermoGravimetric Analysis
- TLCT** "True" Liquid Crystal Templating
- USAF** United States Air Force
- UV** UltraViolet
- XRD** X-Ray Diffraction
- XRR** X-Ray Reflection
- z. B.** zum Beispiel

## 9.7 Curriculum vitae

### Personal data

Name	Andreas Zürner
Date of birth	7 June 1980
Marital status	married, two children

### Education

1991 - 2000	<b>Abitur</b> , <i>König-Karlmann-Gymnasium, Altötting, 1,9</i>
2000 - 2005	<b>Diplom-Chemiker-Univ.</b> , <i>Ludwigs-Maximilians-Universität (LMU), München, 1,8</i>

### Diploma Thesis

title	“Synthese TEM-transparenter, mesoporöser Filme“
supervisors	Prof. Dr. Thomas Bein, Prof. Dr. Konstantin Karaghiosoff
description	Development of a reproducible synthesis for ultrathin (< 100 nm) mesoporous silica films. Variation of key parameters, such as template species, template to silica ratio or dilution.

### Languages

English	fluent
French	fluent
German	native speaker

## Experience

2008 - 2010 Nanoscape AG, Consultancy services in materials synthesis and analysis  
since 05/2010 GÜntner AG & Co. KG, Research & Development department

## Computer skills

image processing Photoshop, Digital Micrograph, Amira, ImageJ  
Office MS Office, Open Office, Adobe Creative Suite  
Programming languages Mainly scripting languages, like Matlab, Povray, php, etc., but also basics in C/C++ and Java  
miscellaneous Matlab, Origin, Latex, MySql

## Voluntary activities

since 1990 Active member, bavarian red cross rescue and water safety  
2002 - 2006 Member of the board, Förderverein der Wasserwacht Töging e.V.

## Hobbies

Family trips  
Traveling  
Swimming

## 9.8 Publications

- A. Zürner, J. Kirstein, M. Döblinger, C. Bräuchle, T. Bein, "Visualizing single-molecule diffusion in mesoporous materials", *Nature*, **450**, 705-708 (2007)
- V. Cauda, A. Schloßbauer, J. Kecht, A. Zürner, T. Bein, "Multiple Core-Shell Functionalized Colloidal Mesoporous Silica Nanoparticles", *J. Am. Chem. Soc.*, **131**, 11361-11370 (2009)
- R. Wei, D. Pedone, A. Zürner, M. Döblinger, U. Rant, "Fabrication of Metalized Nanopores in Silicon Nitride Membranes for Single-Molecule Sensing", *Small*, **6**, 1406-1414 (2010)
- A. Zürner, M. Döblinger, V. Cauda, R. Wei, T. Bein, "Discrete tomography of demanding samples based on a modified SIRT algorithm", *Ultramicroscopy*, revised

## 9.9 Presentations

- German zeolite days 2006, Hannover - Poster
- German zeolite days 2008, Halle - Oral presentation "Probing the inner landscape of a porous nanostructure: correlating single molecule tracking and electron microscopy"
- 4th International FEZA Conference 2008, Paris - Poster

## 9.10 Meetings, Awards

- Participant of the 58th Lindau Nobel Laureate Meeting in 2008
- CeNS (Center for Nanoscience) Publication Award 2008